

**Construction of a Novel Nanosecond Temperature Jump Apparatus and Its Application to Time-Resolved Raman Studies on Protein Dynamics**

**Kohji Yamamoto 1999**

**Construction of a Novel Nanosecond Temperature  
Jump Apparatus and Its Application to Time-Resolved  
Raman Studies on Protein Dynamics**

**Kohji Yamamoto**

**DOCTOR OF PHILOSOPHY**

*Department of Functional Molecular Science  
School of Mathematical and Physical Science  
The Graduate University for Advanced Studies*

1999

**Construction of a Novel Nanosecond Temperature  
Jump Apparatus and Its Application to Time-Resolved  
Raman Studies on Protein Dynamics**

**Kohji Yamamoto**

**DOCTOR OF PHILOSOPHY**

*Department of Functional Molecular Science  
School of Mathematical and Physical Science  
The Graduate University for Advanced Studies*

1999

## Preface

The understanding of chemical reactions is one of central themes in chemistry and the principles of them can be elucidated by the investigation of the initial processes of chemical reactions. In many kinds of reactions, photoreactions have been intensively studied with the advances of ultrafast laser technology. Hence the reactions, which start from the electronically excited states of molecules, have been made profoundly clear heretofore. On the other hand, thermal reactions have not been necessarily studied sufficiently up to the present, whereas they are widely seen in nature and are also practically important. Therefore, the knowledge of reactions starting from electronically ground and vibrationally excited states is not still evident. The author believes that the thermal reactions are the principal ones that must be studied and elucidated hereafter.

For this purpose, he aimed at the construction of a novel apparatus, which is applicable to pursue the initial processes of thermal reactions in the time scales from nanoseconds to milliseconds. He utilized the combined methods of near infrared (NIR) laser-induced temperature jump (T-jump) and time-resolved Raman ( $TR^2$ ) spectroscopy for the following two reasons. One was that NIR laser-induced T-jump can bring about nanosecond-initiation of thermal reactions. The other was that  $TR^2$  spectroscopy gives the precise information of reactive molecules, because vibrational modes are sensitive to the molecular structures and the relationship between vibrational bands and the structures are definite. By using this apparatus, the author studied protein dynamics of thermal unfolding, which is one of thermal reactions. In this study, he succeeded in  $TR^2$  measurements of a protein following the laser induced T-jump for the first time.

This thesis consists of three chapters. In Chapter 1, the subject of protein folding/unfolding is described from the experimental standpoints. Experimental

methods that have been utilized for this subject are explained at first and the understanding of protein dynamics from these studies are enumerated next. In the final section of Chapter 1, the problems of the previous studies are discussed. In Chapter 2, two types of NIR laser-induced T-jump apparatuses applicable to  $TR^2$  measurements are described from the following two viewpoints; the construction of the apparatuses and the performances of them. The new type of a NIR generation system using stimulated Raman seeding-amplification and the effects of this technique are discussed in the former viewpoints. In the latter ones, the direct measurements of transient temperature following NIR induced T-jump are written and then the instrumental limitation of these T-jump measurements are discussed from the temporal behavior of the elevated temperature. In Chapter 3, the application of this apparatus to the unfolding dynamics of ribonuclease A (RNase A) is described. From the temporal changes of Raman bands indicating the protein structures, the transient structures of RNase A are discussed.

# Contents

Preface

Contents

Chapter 1. General Introduction	1
1.1 Experimental Methods for Studying Fast Folding/Unfolding	2
1.1.1 Rapid Probe	3
1.1.2 Rapid Initiation Techniques	7
1.2 Recent Experimental Understandings of Fast Folding/Unfolding	9
1.2.1 Long Homopeptides	9
1.2.2 Small Peptides	10
1.2.3 Proteins	11
1.3 Several Problems in Recent Studies	13
References	15
Chapter 2 Construction of Temperature Jump Apparatuses Applicable to Raman Measurements	19
Abstract	20
2.1 Introduction	21
2.1.1 Determination of Transient Temperature	22
2.1.2 Choice of Raman Media	24
2.1.3 Requisite Intensity of Heat Pulse and Sample Thickness for T-jump	25
2.2 Experimental Procedures	26
2.2.1 Wavelength Conversion with Hydrogen and Deuterium	26
2.2.2 Sample and Illumination Geometry	28
2.2.3 Measurements of Time-Resolved Raman Spectra	29
2.3 Result	30
2.3.1 Accuracy of Temperature Determination	30
2.3.2 Characteristics of Generated 1.89- $\mu\text{m}$ Pulse	32
2.3.3 Characteristics of Generated 1.56- $\mu\text{m}$ Pulse	32
2.3.4 Transient Temperature Change by Illumination of Heat Pulse	34
2.4 Discussion	37
2.4.1 Effect of Seeding-Amplification	37

2.4.2	Observed Temperature Changes in T-Jump Measurements	42
2.4.3	Induced Thermal Effects upon T-Jump	48
2.4.4	Applicability to Raman Measurements of Protein	49
2.5	Summary	50
	Appendix	51
	References	53
Chapter 3	Time-Resolved Raman Study on Thermal Unfolding of Ribonuclease A	71
	Abstract	72
3.1	Introduction	73
3.2	Experimental Procedures	74
3.2.1	Sample Preparation	74
3.2.2	Measurements of Steady-State and Time-Resolved Raman Spectra	75
3.3	Result	76
3.4	Discussion	79
3.4.1	Temperature Jump in RNase A Solution	79
3.4.2	Disulfide Conformations	81
3.4.3	Conformations of Methionine	83
3.4.4	Conformational Change of Tyrosine Side Chain	83
3.4.5	Sulfate Ions	84
	References	86
	List of Publications	99
	Acknowledgement	100

## **Chapter 1. General Introduction**



Proteins adopt specific folded three-dimensional structure (tertiary structure) to attain biological activity. Nevertheless the genetic information for the protein specifies only the linear sequence of amino acids (primary structure). Specific tertiary structure is, therefore, determined solely by the primary structure<sup>1</sup> and understanding how the primary structure folds into the tertiary structure is a central problem in modern structural biology.<sup>2-7</sup> However, as Levintal pointed out,<sup>8</sup> it takes much longer time than the life time of an organism for a protein to explore all the possible conformations by random searching. This indicates that there must be protein folding pathways to speed up this process markedly (the Levinthal paradox<sup>9,10</sup>) and that the amino acid sequence codes the mechanistic paths which folding actually follows through the vast conformational space. Therefore, the key to solving the problem of protein folding is given by the studies on the early events of protein folding/unfolding dynamics.

The author first introduces the experimental methods applicable to pursuing fast events of protein folding/unfolding within subsecond and then reviews the recent results of the fast events of it. Finally, the author discusses several problems of recent experimental studies on protein dynamics.

## **1.1 EXPERIMENTAL METHODS FOR STUDYING FAST FOLDING/UNFOLDING**

Early events of folding/unfolding dynamics can be investigated by the transient relaxation methods,<sup>11</sup> that is, by monitoring the temporal changes after rapid displacement of equilibrium or after rapid movement from equilibrium. Both the rapid displacement and the rapid movement initiate chemical transitions of folding/unfolding and, accordingly, transient protein structures following these initiations can be directly

detected. The rapid displacement is obtained by sudden change of an intensive variable (temperature, pressure, pH and electric field). On the other hand, the rapid movement is accomplished by sudden change of an extensive variable. Concentration change or electric dipole change induced by laser light is, especially, used for this purpose. Rapid probe and rapid initiation of folding/unfolding is, therefore, necessary to observe fast events of it, except for NMR spectroscopy with amide proton exchange methods.<sup>12</sup>

### 1.1.1 Rapid Probe

**Circular Dichroism.** Circular dichroism (CD) appears when a molecule has the difference between the absorption coefficients for left and right circularly polarized light<sup>13</sup> and hence it is observed in the absorption band of a chiral molecule. A circular dichroism spectrum of a protein, especially, contains two characteristic regions (the far-UV and the near-UV regions), which give the structural information of the protein.<sup>12</sup> The CD band in the far-UV region (180-240 nm) due to the absorption of the amide groups provides a qualitative measure of the average secondary structure content;  $\alpha$ -helices,  $\beta$ -sheets,  $\beta$ -turns and random coils.<sup>13</sup> The CD band in the near-UV region (250-310 nm) originates in the absorption of aromatic-side chains (tryptophan and tyrosine) and appears only when the aromatic-side chains are tightly packed within the core of a stable folded protein. The near-UV CD band is hence a useful indicator for the formation of a rigid core in the protein.

**Absorption and Fluorescence in UV or Visible Region.** Absorption spectroscopy is widely used to obtain structural information of proteins. The UV absorption of aromatic-side chains and the visible absorption of prosthetic groups (heme, retinal, and so on) reflect their electronic states. Hence absorption spectroscopy gives the information of the local environments around aromatic-side chains or around prosthetic

groups in a protein as well as that of their own structures. In the visible spectrum of heme, especially, the Soret band at about 420 nm and the Q bands ( $Q_0$  band at about 560 nm and  $Q_1$  band at 525 nm) are useful indicator bands to pursue the structure of heme proteins.<sup>14</sup>

Fluorescence is also used to pursue protein structures. Intrinsic fluorescence of proteins without prosthetic groups is due to the aromatic residues. Fluorescence with the excitation at 290-300 nm is particularly dominated by that of tryptophan, whereas tyrosine fluorescence contributes significantly at shorter-wavelength excitation.<sup>15</sup> By monitoring the amount of quenched fluorescence of tryptophan, the protein structures around it can be investigated<sup>16</sup>; its exposure to solvent and the formation of tertiary contacts around it.

### **Vibrational Spectroscopy; IR Absorption and Raman Scattering.**

To detect vibrational states of a molecule, IR absorption and Raman scattering (nonresonance or resonance) are often used. Vibrational spectroscopy has both sufficient time-resolution and structural sensitivity for the characterization of protein structures on the folding/unfolding dynamics. The structural specificity is derived from the connection of molecular vibrations to specific structures and to environments around the molecule. Hence vibrational spectroscopy gives more precise information than absorption (UV and visible) and fluorescence.

#### *(1) IR Absorption*

Proteins and polypeptides give the intense IR bands that originate in the vibrations of backbone chains; amide I ( $\sim 1650\text{ cm}^{-1}$ ), amide II ( $\sim 1550\text{ cm}^{-1}$ ), and amide III ( $\sim 1250\text{ cm}^{-1}$ ).<sup>17</sup> These bands are sensitive to the conformation of backbone chains and the types of hydrogen bonding ( $\alpha$ -helices,  $\beta$ -sheets, random coils, and so on).

The amide I mode is mainly the stretching motion of the backbone peptide C=O group with some contribution from the C-N stretching. The amide II mode consists primarily of N-H in-plane bending coupled with some extent of C-N stretching. The N-H in-plane bending also contributes to the amide III mode, which includes mainly the N-C $_{\alpha}$  stretching.

The amide I band is usually used for IR absorption studies of proteins and peptides especially. To avoid the overlap between the amide I band and the intense IR absorption band of water around 1650 cm<sup>-1</sup>, heavy water (D<sub>2</sub>O) is often used<sup>18-20</sup> instead of light water (H<sub>2</sub>O). The amide I for deuterated amide groups is usually labeled as amide I', which is slightly low-frequency shifted by the isotope effect.<sup>21</sup> The band-frequencies of specific secondary structures in the amide I' are summarized in Ref. 20.

## *(2) Resonance Raman Scattering*

Resonance Raman scattering is widely used to determine the local environmental changes of prosthetic groups and aromatic side-chains as well as secondary structure contents. The UV excitation<sup>15,22,23</sup> enhances the bands of aromatic side-chains as well as those of amide I, amide II, and amide III of the backbone-chain. The amide II mode is particularly prominent, though it is not observed in nonresonant Raman spectra with visible excitation. Heme proteins are intensively and precisely investigated by visible resonance Raman scattering in the studies on protein structures. Raman bands of heme proteins are sensitive to the oxidation, spin, and coordination states of hemes.<sup>24,25</sup> For example, the  $\nu_3$  bands in the 1475-1520 cm<sup>-1</sup> region are sensitive to both the axial coordination and the spin state of the iron at the center of the heme and the  $\nu_2$  bands in the 1550-1600 cm<sup>-1</sup> region is sensitive to the iron spin state.<sup>26</sup>

A tremendous enhancement of the scattering intensity by the resonance effect

has allowed the use of much less concentrated solutions and structural investigations of various proteins so far.

### *(3) Nonresonant Raman Scattering*

Nonresonant Raman scattering is also used for the determination of protein structures. To obtain sufficient Raman signals, much more concentrated solution of protein is needed for nonresonant Raman measurements than for resonance Raman ones. In spite of this disadvantage, nonresonant Raman scattering has the important advantage that all the Raman bands sensitive to protein structures can be detected simultaneously; S-S stretching, C-S stretching, tyrosine doublet, amide I, amide III, and so on. The S-S stretching and C-S stretching give especially characteristic Raman bands which are sensitive to the conformations of disulfide bridges and those of methionine side chains, respectively; S-S stretching bands in 505-545  $\text{cm}^{-1}$  and C-S stretching bands in 630-760  $\text{cm}^{-1}$ .<sup>22</sup> These bands can be detected by nonresonant Raman scattering but are difficult to measure by resonance Raman scattering because they are enhanced by the light of shorter wavelength than 200 nm.<sup>23</sup> Fermi resonance in the phenyl ring of the tyrosine residue gives tyrosine doublet at 830  $\text{cm}^{-1}$  and 850  $\text{cm}^{-1}$ ,<sup>22,27</sup> which is sensitive to the hydrogen bonding associated with the phenolic hydroxyl group.

In addition, this method as well as fluorescence emission and resonance Raman scattering has the advantage over transmission methods (CD and absorption spectroscopy). Actually refractive index fluctuations and other variations are induced in the sample by initiation of reactions. Collection of scattering or emission light is, however, less influenced by these disturbances than that of transmission light.

### 1.1.2 Rapid Initiation Techniques

**Rapid Flow Methods.** Rapid flow methods are the earliest techniques for reaction initiations and are most widely used for the studies on protein dynamics; continuous flow method, stopped-flow method, and rapid quenching method. In the continuous flow method, two solutions are injected into a mixing chamber at constant flow rate and the mixed solution flows continuously through the observation cell. The time evolution of the reaction is determined from the flow rate and the distance between the mixing and the probing points. In the stopped-flow method, two solutions are rapidly mixed in a mixing chamber and the solution flowing is suddenly stopped. The reaction is continuously monitored at a constant point of the observation cell. In the rapid quenching method, two solutions are rapidly mixed and then the reaction is stopped after it has been allowed to proceed in a certain time. This 'frozen' product can then be examined by slow-detection techniques such as NMR.

The rapid flow methods are applicable to a very vast range of conditions, as relaxation can be induced by pH-, temperature-, or denaturant- (urea, guanidinium hydrochloride, and so on) jumps. But conventional mixers that are used for rapid flow methods include dead time as long as a few milliseconds. As a result the fast events within millisecond have not been examined by rapid flow methods. Recently, a new continuous mixer whose dead time is shorter than 100  $\mu$ s has been developed and applied to the studies on fast folding of cytochrome *c*.<sup>26,28-30</sup>

**Photochemical Triggering.** Photochemical triggering have been used to study dynamics of heme proteins. To move the protein ensemble from the folded/unfolded equilibrium, a visible laser pulse can be used where it triggers protein folding/unfolding by initiating a photochemical reaction. Protein folding/unfolding starts by

photodissociation of the CO-bound reduced form<sup>31-34</sup> or photoreduction of the oxidized form.<sup>35,36</sup> These methods use the protein-stability difference between the CO-bound and CO-unbound states in photodissociation or that between the reduced and oxidized states in electron injecting/removing.

**Temperature Jumps.** Sudden temperature-change displaces the equilibrium position of protein ensembles and starts the folding/unfolding relaxation. A profile of free energy of a protein is an approximately parabolic against temperature<sup>37</sup> and, accordingly, it leads to protein unfolding both at low and high temperatures, which are usually called as cold denaturation and heat denaturation, respectively. T-jump experiments can therefore be used to study protein refolding from cold-denatured states and protein unfolding from folded states as well as those of secondary structures of model peptides.

T-jump method was pioneered by Eigen and De Mayer,<sup>11</sup> where they used rapid capacitance discharge to produce Joule heating in conducting solutions. The temporal resolution of the measurements of fast events by this approach is limited to the microsecond time scale. This method has been recently applied to folding dynamics of barstar.<sup>38</sup> Mixing methods also accomplish T-jump and have been applied for studies of protein dynamics.<sup>39</sup> Microwave heating has been applied to NMR spectroscopy of proteins, where the T-jump as large as 25°C has been obtained within 20 ms. The laser-induced T-jump method has been extensively utilized for protein dynamics<sup>20,34,40-42</sup> and has revealed nanosecond-to-microsecond time scales of folding/unfolding dynamics of protein and peptide. Precise explanation about several types of laser T-jump methods is described in Chapter 2.

## **1.2 RECENT EXPERIMENTAL UNDERSTANDINGS OF FAST FOLDING/UNFOLDING**

The initial steps of protein folding/unfolding have been extensively studied by the combination of NMR with amide proton exchange and by the combination of CD or fluorescence with stopped-flow mixing.<sup>12</sup> These studies succeeded in the characterization of protein dynamics in the temporal range from millisecond and revealed that large amplitude of relaxation occurs within the instrumental dead times of milliseconds (4-20 ms). One of the most important results in these studies is the discovery of accumulated early transient intermediates<sup>43,44</sup> which appear nearly native in terms of secondary structure contents from far-UV CD but still unfolded in terms of the environments around aromatic side chains from near-UV CD.

To pursue faster events of protein folding/unfolding dynamics than milliseconds, the laser-induced T-jump and rapid continuous flow have been used. These methods allow the investigations in the time scales of 10 ns and 100  $\mu$ s, respectively. Model peptides have been used for these studies as well as proteins from the viewpoint that the dynamics of simple fragments helps the understanding of the overall folding/unfolding process in proteins.

### **1.2.1 Long Homopeptides**

For the study of fast events of  $\alpha$ -helix-coil transition, long  $\alpha$ -helical homopolymers of amino acids were initially investigated (reviewed by Gruenewald et al.<sup>45</sup>). The fastest relaxation times range from 50 ns to microseconds, which show averaged relaxation times of the whole homopolymers. They were determined indirectly from the data obtained by the probes lacking in structural specificity (ultrasonic absorption, dielectric loss, and so on) and hence it is difficult to interpret these



relaxation times. Moreover it is not clear that these results can be applied to the understanding of protein dynamics because the short runs of helical structures are usually found in proteins but long runs of homopolymers are not.

## 1.2.2 Small Peptides

### (1) $\alpha$ -helical peptides

For the investigation of  $\alpha$ -helix dynamics, unfolding dynamics of Fs-peptide (21-residue peptide: A<sub>5</sub>(AAARA)<sub>3</sub>A, A = alanine and R = arginine) was investigated in the time scales from nanosecond to millisecond by laser-induced T-jump.<sup>18,20,34,42,46</sup> This peptide forms  $\alpha$ -helix at room temperature owing to the strong helix propensity of alanine residues and is transformed to random coils following the rise of temperature. In the time-resolved IR absorption of amide I', two relaxation phases within milliseconds were observed<sup>18,20</sup>; 10 ns (small amplitude) and 160 ns (dominant amplitude). This result is consistent with that of time-resolved UV resonance Raman study on amide I, amide II, and amide III.<sup>42</sup> On the other hand, only one relaxation phase of 20 ns was observed from the fluorescence of N-terminal probe, 4-(methylamino)benzoic acid (MABA),<sup>34,46</sup> which was covalently bound to Fs-peptide. Dyer et al. interpreted that the faster process (10-20 ns) involves the rapid folding/unfolding equilibrium of the helix ends and the slower process (160 ns) involves the equilibrium between helix-containing and nonhelix-containing structures. The faster process is indicated as the nucleation process of forming the first turn of helix and the slower process is as the propagation process of the subsequent-turn formation.

For the study on dynamics of helix-helix interactions, GCN4-p1 peptide was investigated by the combination of laser-induced T-jump with time-resolved IR absorption.<sup>20</sup> Dimer structure of  $\alpha$ -helical GCN4-p1 peptides is formed at low

temperature and is disordered at high temperature. Hence this dimer structure is a model of tertiary structure involving the interaction between  $\alpha$ -helices. Relaxation time of the dimer is 3 orders of magnitude slower than that of the monomeric Fs peptide. This result indicates that the packing of the two helices occurs much slower than intrinsic transition between helical and coiled structure, that is, formation of tertiary structure is much slower than that of secondary structure.

## **(2) $\beta$ -hairpin**

For the investigation of  $\beta$ -structures, 16-residue C-terminal fragment of protein G B1 was studied by the combination of laser induced T-jump with tryptophan fluorescence.<sup>34,47</sup> This peptide forms a  $\beta$ -hairpin structure, which is the simplest  $\beta$ -structure with the antiparallel pleated sheet. The time for  $\beta$ -hairpin formation is observed to be  $\sim 6 \mu\text{s}$ , about 30-fold slower than that of the  $\alpha$ -helix formation of Fs peptide. The reason for the slower formation of  $\beta$ -hairpin is discussed by the statistical mechanical model,<sup>34,47,48</sup> which shows that the formation of the  $\beta$ -hairpin needs to cross over a greater free-energy barrier than that of an  $\alpha$ -helix. This model also gives the conformation at the transition state of the formation of this  $\beta$ -hairpin, which has two hydrogen bonds but no hydrophobic side-chain interactions within the  $\beta$ -hairpin structure. This structure indicates the necessity of the rapid formation of hydrogen bonding which precedes formation of hydrophobic cluster (hydrophobic collapse) on the pathway of  $\beta$ -hairpin formation.

## **1.2.3 Proteins**

### **(1) Apomyoglobin**

Apomyoglobin is an  $\alpha$ -helix rich protein consisting of eight  $\alpha$ -helices (A-H helix) and no  $\beta$ -structure. The fast events of apomyoglobin have been intensively

investigated by laser induced T-jump.<sup>19,20,41,49-51</sup> Dyer et al. studied its unfolding dynamics by IR absorption of amide I<sup>19,20,49</sup>; transition from the native state to heat-denatured states. Gruebele et al. studied its folding dynamics by tryptophan fluorescence<sup>41,50,51</sup>; transition from cold-denatured states to the native state. These groups observed two relaxation phases in nanosecond and microsecond region within milliseconds; 50 ns and 90  $\mu$ s for unfolding dynamics, and 250 ns and 4-17  $\mu$ s for folding dynamics. The microsecond relaxation is assigned to the formation of hydrophobic AGH core, which consist of A-, G-, and H-helices. This time scale is much faster than the temporal order that is expected from an intrachain-diffusion model and, therefore, it is suggested that the formation of intervening secondary structure (nonnative B-F structure of temporary helical segments) precedes the formation of AGH core. However, there is the discrepancy in the interpretations of the observed nanosecond relaxation between the two groups. From the comparison of the intrinsic  $\alpha$ -helix formation time of Fs peptide, Dyer et al. considered that the nanosecond relaxation originates in the formation of the  $\alpha$ -helical secondary structures. On the other hand, Gruebele et al. interpreted that nanosecond phase is a local collapse process for the formation of nonnative tertiary contacts among hydrophobic side chains and that this hydrophobic collapse induces the formation of the full A-helix.

## **(2) Cytochrome *c***

Cytochrome *c* has five  $\alpha$ -helices and no  $\beta$ -strands. The fast events of cytochrome *c* have been investigated by the combination of rapid continuous flow method with visible resonance Raman scattering<sup>26,28-30</sup> and by that of photochemical triggering with absorption of Soret band.<sup>31-34</sup> In unstructured states of cytochrome *c*, alternation of ligands to the heme occurs within several hundred microseconds. The

methionine binding to the heme, particularly, occurs at the time constant of 40  $\mu$ s.<sup>31</sup> From the intrachain-diffusion model,<sup>32-34</sup> this time constant is interpreted as the time scale of the contact formation between two regions of unfolded peptide fragments. The ligand exchange following this process occurs in millisecond time scales.<sup>26,28-30</sup> These results indicate the folding pathway of cytochrome *c* in the following; (1) at the first step, nonspecific condensation of the polypeptide chain occurs in the several hundred microseconds region without fine-tuning of the protein structure and it results in reducing the conformational space, and (2) at the next step, the native conformation is reached in the subsequent ligand exchange in slower time scales.

### **(3) Ribonuclease A**

Ribonuclease A is a four-disulfide containing protein that consists of four  $\alpha$ -helices and six  $\beta$ -strands. The unfolding dynamics of ribonuclease A was pursued in the time scales from picoseconds to nanoseconds by the combination of laser-induced T-jump with IR absorption of amide I'.<sup>40</sup> The disruption of the  $\beta$ -sheet appears after 1-ns delay following T-jump, and within 5.5 ns the absorption of amide I' due to the  $\beta$ -sheet achieves 15%-decrease of the intensity expected at equilibrium. This result is interpreted as the local changes of the  $\beta$ -sheet which occur in nanosecond time scale by the hydrogen bond alternation in amide groups of the  $\beta$ -sheet with water.

## **1.3 SEVERAL PROBLEMS IN RECENT STUDIES**

The studies on fast events of protein dynamics have been focused on the temporal changes of secondary and tertiary structures. However, the probe methods that have been used for these studies cannot give the direct information of tertiary structures. In fact, IR absorption and UV resonance Raman scattering of amide bands give the

information of secondary structure *contents* and tryptophan fluorescence gives the local structure around only tryptophan residues. However, the stability of tertiary structures is largely effected by the interactions between side chains; hydrogen bonding, hydrophobic interaction, and disulfide bridge. It is actually well known that the protein mutated with only one residue usually reduces its protein stability. This suggests that the side chain interactions influence the stability of whole proteins. Therefore, it is important to monitor directly transient conformations of side chains in the initial steps of folding/unfolding dynamics. For this purpose, nonresonant Raman spectroscopy is appropriate because it can give the residue-selective information about side-chain conformations and its environments. Moreover, it may be questionable whether the fast events of small peptides reflect those of proteins. The reason is that small peptides, in fact, show less cooperativity on their folding/unfolding transitions than proteins because fewer amounts of interactions exist in small peptides.

From the above considerations, the author believes that the investigation of transient side-chain conformations in proteins gives new insights to the protein-folding problem and that the combination of time-resolved nonresonant Raman spectroscopy with laser induced T-jump is a powerful method for this purpose.

## REFERENCES

- 1 C. B. Anfinsen, *Science* **181**, 223-230 (1973).
- 2 Y. Bai and S. W. Englander, *Proteins: Struct., Funct., Genet.* **24**, 145-151 (1996).
- 3 A. D. Miranker and C. M. Dobson, *Curr. Opin. Struct. Biol.* **6**, 31-42 (1996).
- 4 K. A. Dill and H. S. Chan, *Nat. Struct. Biol.* **4**, 10-19 (1997).
- 5 W. A. Eaton, V. Munoz, P. A. Thompson, C. K. Chan, and J. Hofrichter, *Curr. Opin. Struct. Biol.* **7**, 10-14 (1997).
- 6 A. R. Fersht, *Curr. Opin. Struct. Biol.* **7**, 3-9 (1997).
- 7 H. Roder and W. Colon, *Curr. Opin. Struct. Biol.* **7**, 15-28 (1997).
- 8 C. Levinthal, *J. Chim. Phys.* **65**, 44 (1968).
- 9 R. Zwanzig, A. Szabo, and B. Bagchi, *Proc. Natl. Acad. Sci* **89**, 20 (1992).
- 10 T. E. Creighton, in *Mechanisms of Protein Folding*, edited by R. H. Pain (Oxford University Press Inc., New York, 1994), pp. 1-25.
- 11 M. Eigen and L. DeMaeyer, in *Technique of Organic Chemistry*, Vol. 8, edited by S. L. Friess, E. S. Lewis, and A. Weissberger (Interscience, New York, 1963), pp. 895-1054.
- 12 H. Roder and G. A. Eloeve, in *Mechanisms of Protein Folding*, edited by R. H. Pain (Oxford University Press Inc., New York, 1994), pp. 26-54.
- 13 J. W. C. Johnson, *Ann. Rev. Biophys. Chem.* **17**, 145-166 (1988).
- 14 B. Cartling, in *Biological Applications of Raman Spectroscopy*, Vol. 3, edited by T. G. Spiro (John Wiley & Sons, New York, 1988), pp. 217-248.
- 15 B. Hudson and L. C. Mayne, in *Biological Applications of Raman Spectroscopy*, Vol. 2, edited by T. G. Spiro (John Wiley & Sons, New York, 1987), pp. 181-209.
- 16 M. Gruebele, *Annu. Rev. Phys. Chem.* **50**, 485-516 (1999).
- 17 S. Krimm, in *Biological Applications of Raman Spectroscopy*, Vol. 1, edited by T. G. Spiro (John Wiley & Sons, New York, 1987), pp. 1-45.
- 18 S. Williams, T. P. Causgrove, R. Gilmanshin, K. S. Fang, R. H. Callender, W. H. Woodruff, and R. B. Dyer, *Biochemistry* **35**, 691-697 (1996).
- 19 R. Gilmanshin, S. Williams, R. H. Callender, W. H. Woodruff, and R. B. Dyer, *Biochemistry* **36**, 15006-15012 (1997).
- 20 R. B. Dyer, F. Gai, W. H. Woodruff, R. Gilmanshin, and R. H. Callender, *Acc. Chem. Res.* **31**, 709-716 (1998).
- 21 A. T. Tu, in *Advances in Spectroscopy*, Vol. 13, edited by R. J. H. Clark and R. E. Hester (John Wiley & Sons, New York, 1986), pp. 47-112.
- 22 I. Harada and H. Takeuchi, in *Spectroscopy of Biological Systems*, Vol. 13, edited

- by R. J. H. Clark and R. E. Hester (John Wiley & Sons, New York, 1986), pp. 113-175.
- 23 R. P. Rava and T. G. Spiro, *Biochemistry* **24**, 1861-1865 (1985).
  - 24 P. R. Carey, *Biochemical Applications of Raman and Resonance Raman Spectroscopies* (Academic Press, New York, 1982).
  - 25 T. Kitagawa and T. Ogura, *Progress in Inorganic Chemistry* **45**, 431-479 (1997).
  - 26 S. Takahashi, S.-R. Yeh, T. K. Das, C.-K. Chan, D. S. Gottfried, and D. L. Rousseau, *Nature Struct. Biol.* **4**, 44-50 (1997).
  - 27 M. N. Siamwiza, R. C. Lord, M. C. Chen, T. Takamatsu, I. Harada, H. Matsuura, and T. Shimanouchi, *Biochemistry* **14**, 4870-4876 (1975).
  - 28 S.-R. Yeh, S. Takahashi, B. Fan, and D. L. Rousseau, *Nature Struct. Biol.* **4**, 51-56 (1997).
  - 29 S.-R. Yeh and D. L. Rousseau, *Nature Struct. Biol.* **5**, 222-228 (1998).
  - 30 S.-R. Yeh, S. Han, and D. L. Rousseau, *Acc. Chem. Res.* **31**, 727-736 (1998).
  - 31 C. M. Jones, E. R. Henry, Y. Hu, C.-K. Chan, S. D. Luck, A. Bhuyan, H. Roder, J. Hofrichter, and W. A. Eaton, *Proc. Natl. Acad. Sci. USA* **90**, 11860-11864 (1993).
  - 32 S. J. Hagen, J. Hofrichter, A. Szabo, and W. A. Eaton, *Proc. Natl. Acad. Sci. USA* **93**, 11615-11617 (1996).
  - 33 S. J. Hagen, J. Hofrichter, and W. A. Eaton, *J. Phys. Chem. B* **101**, 2352-2365 (1997).
  - 34 W. A. Eaton, V. Munoz, P. A. Thompson, E. R. Henry, and J. Hofrichter, *Acc. Chem. Res.* **31**, 745-753 (1998).
  - 35 T. Pascher, J. P. Chesick, J. R. Winkler, and H. B. Gray, *Nature* **271**, 1558-1560 (1996).
  - 36 G. A. Mines, T. Pascher, S. C. Lee, J. R. Winkler, and H. B. Gray, *Chem. Biol.* **3**, 491-497 (1996).
  - 37 P. L. Privalov, *Crit. Rev. Biochem. Mol. Biol.* **25**, 281-305 (1990).
  - 38 T. Ikura and A. R. Fersht, in *37th Annual Meeting of the Biophys. Soc. JPN.* (Wako, Japan, 1999).
  - 39 B. Noelting, R. Golbik, J. L. Neira, A. S. S.-Gonzalez, G. Schreiber, and A. R. Fersht, *Proc. Natl. Acad. Sci. USA* **94**, 826-830 (1997).
  - 40 C. M. Phillips, Y. Mizutani, and R. M. Hochstrasser, *Proc. Natl. Acad. Sci. USA* **92**, 7292-7296 (1995).
  - 41 M. Gruebele, J. Sabelko, R. Ballew, and J. Ervin, *Acc. Chem. Res.* **31**, 699-707 (1998).
  - 42 I. K. Lednev, A. S. Karnoup, M. C. Sparrow, and S. A. Asher, *J. Am. Chem. Soc.* **121**, 4076-4077 (1999).

- 43 K. Kuwajima, Y. Hiraoka, M. Ikeguchi, and S. Sugai, *Biochemistry* **24**, 874-881 (1985).
- 44 K. Kuwajima, H. Yamaya, S. Miwa, S. Sugai, and T. Nagamura, *FEBS Lett.* **221**, 115-118 (1987).
- 45 B. Gruenewald, C. U. Nicola, A. Lustig, and G. Schwarz, *Biophys. Chem.* **9**, 137-147 (1979).
- 46 P. A. Thompson, W. A. Eaton, and J. Hofrichter, *Biochemistry* **36**, 9200-9210 (1997).
- 47 V. Munoz, P. A. Thompson, J. Hofrichter, and W. A. Eaton, *Nature* **390**, 196-199 (1997).
- 48 V. Munoz, E. Henry, J. Hofrichter, and W. A. Eaton, *Proc. Natl. Acad. Sci. USA* **95**, 5872-5879 (1998).
- 49 R. Gilmanshin, S. Williams, R. H. Callender, W. H. Woodruff, and R. B. Dyer, *Proc. Natl. Acad. Sci. USA* **94**, 3709-3713 (1997).
- 50 R. M. Ballew, J. Sabelko, and M. Gruebele, *Nature Struct. Biol.* **3**, 923-926 (1996).
- 51 R. M. Ballew, J. Sabelko, and M. Gruebele, *Proc. Natl. Acad. Sci. UAS* **93**, 5759-5764 (1996).





**Chapter 2.**  
**Construction of Temperature Jump Apparatuses**  
**Applicable to Raman Measurements**

*Appl. Spectrosc.* in submission  
Kohji Yamamoto, Yasuhisa Mizutani, and Teizo Kitagawa

## ABSTRACT

We constructed two types of nanosecond temperature jump (T-jump) apparatuses applicable to Raman measurements. In the apparatuses, T-jump was achieved by 1.89- $\mu\text{m}$  near infrared (NIR) pulses or 1.56- $\mu\text{m}$  NIR pulses. Two wavelengths of NIR were generated by stimulated Raman scattering (SRS) of  $\text{H}_2$  or  $\text{D}_2$  from the fundamental line of a Q-switched Nd:YAG laser; in a single pass configuration with  $\text{H}_2$  for 1.89- $\mu\text{m}$  NIR and in a seeding-amplification configuration with  $\text{D}_2$  for 1.56- $\mu\text{m}$  NIR. The seeding-amplification configuration brought about the improvements of conversion efficiency, of stability between successive generated pulses, and of beam quality. We applied these apparatuses to transient Raman measurements of  $\text{MoO}_4^{2-}$  solution and obtained transient temperatures of heated volume directly by ratios of anti-Stokes to Stokes intensities. From the results nanosecond temperature rise by illumination of nanosecond heat pulses at 1.89- $\mu\text{m}$  or 1.56- $\mu\text{m}$  was directly examined. The longer-time limit of temperature jump experiments is discussed on the points of thermal diffusion, thermal transfer and replacement of sample. It becomes clear that this limit is not determined by thermal diffusion but by replacement of sample in thick or thin sample and by thermal transfer in thin sample.

## 2.1 INTRODUCTION

Reactions can be categorized by inducing origins. Photoreactions are induced by light and thermal reactions are induced by heat. To investigate initial processes of these reactions, relaxation methods are employed extensively in combination with many kinds of spectroscopy. Raman spectroscopy is so sensitive to molecular structures and the environments around molecules that it gives more precise information about molecular states than absorption and fluorescence spectroscopy. Therefore the combination of relaxation methods with Raman spectroscopy is a powerful tool for this purpose. As to the investigation of the initial process of photoreactions by Raman spectroscopy, time resolution has reached to the time scales of picoseconds with advances of ultrafast laser technology. The fastest time-resolution is limited by probe bandwidth due to Fourier transform limitation. By using two laser pulses as pump and Raman probe lights, fast events on photoexcited molecules have been extensively studied from the time scales of picoseconds to that of microseconds at present. On the other hand, fast processes of thermal reactions have not been well investigated by Raman spectroscopy so far, compared with those of photoreactions. The reason for few studies on the former is that rapid heating method at high repetition is uncommon. As a result, understanding of fast processes of thermal reactions is very limited, although thermal reactions are more widely seen in the nature. Therefore construction of heating apparatus applicable to time-resolved Raman measurements are very meaningful for the studies on thermal reactions.

Among various methods of temperature jump (T-jump) used to investigate thermal reactions, the laser-induced T-jump method can be applied to high repetition measurements. Laser-induced T-jump is achieved (i) by heating water directly or (ii) by

transferring heat from dissolved dyes.<sup>1</sup> Overtones or combinations of vibrations of water are excited by a near infrared (NIR) pulse in T-jump (i), or dissolved dyes are electronically excited by a visible pulse in T-jump (ii). The laser-induced T-jump is completed by two processes; the first step is energy dissipation of vibrationally excited water or of electronically excited dyes and the second step is thermal equilibration of dissipated energy between the excited molecules and their surrounding molecules. In T-jump (i), NIR is generated by Raman shifting of Nd:YAG laser fundamental (1064 nm) with N<sub>2</sub> liquid<sup>2,3</sup> (1.41  $\mu$ m) or with molecular gases,<sup>4-12</sup> while it is also generated by the difference mixing of two dye laser outputs by LiNbO<sub>3</sub> crystal<sup>13</sup> (2.0  $\mu$ m). Our laser induced T-jump was achieved with NIR pulses, which were shifted by H<sub>2</sub> or D<sub>2</sub> with stimulated Raman effect from the fundamental line of a Q-switched Nd:YAG laser. First we explain three types of generation techniques of NIR including the single pass, the half resonator and the seeding-amplification. Second we describe the performance of two T-jump apparatuses constructed here, which was directly examined by measuring transient temperatures of the sample illuminated by the heat pulses. The transient temperature was calculated from the relationship between intensity-ratios of anti-Stokes/Stokes bands of molybdate ions (MoO<sub>4</sub><sup>2-</sup>) in water. Finally, we discuss the characteristics of the NIR generations by H<sub>2</sub> and D<sub>2</sub>, the temporal limitations on the laser-induced T-jump experiments with high-repetition heating, and the applicability of two types of T-jump apparatus to nonresonant Raman measurements of proteins. We called a NIR pulse utilized for T-jump as a heat pulse hereafter.

### **2.1.1 DETERMINATION OF TRANSIENT TEMPERATURE**

Illumination of a heat pulse to a sample is followed by the temporal temperature change of the laser-illuminated volume. The transient temperature of the

heated volume was determined by the intensity-ratios of anti-Stokes to Stokes bands of  $\text{Na}_2\text{MoO}_4$  in an aqueous solution (1.5 M). The Raman scattering of the molybdate solution was excited by another laser with variable delay times ( $\Delta t$ ) after illumination of heat pulses. The intensity (photon-counting rate) of anti-Stokes ( $I_{aS}$ ) and Stokes ( $I_S$ ) bands of a given molecular vibration with a wavenumber of  $\tilde{\nu}_{mol}$  is related to the instantaneous temperature ( $T$ ) by Eq. 1,<sup>14</sup>

$$\left( \frac{I_{aS}}{I_S} \right)_T = \left( \frac{\tilde{\nu}_{ex} + \tilde{\nu}_{mol}}{\tilde{\nu}_{ex} - \tilde{\nu}_{mol}} \right)^3 \exp \left( - \frac{hc\tilde{\nu}_{mol}}{k_B T} \right) \quad (1)$$

where  $\tilde{\nu}_{ex}$  and  $k_B$  are a Raman excitation wavenumber and Boltzmann factor, respectively. Basic assumption for Eq. (1) is Boltzmann distribution among vibrational freedoms, which is usually satisfied within subnanosecond in liquid phase. In the practical use of Eq. (1), it is more convenient to determine the amount of temperature rise ( $\Delta T$ ) than the absolute temperature. Supposed that the sample is initially placed in thermal equilibrium at  $T_0$  and raised by  $\Delta T$  upon illumination of the heat pulse, the measurements of Raman intensities at the initial stage,  $(I_{aS}/I_S)_{T_0}$ , and a transient state  $(I_{aS}/I_S)_{T_0+\Delta T}$  give  $\Delta T$  by Eq. (2).

$$\ln \left( \frac{I_{aS}}{I_S} \right)_{T_0+\Delta T} - \ln \left( \frac{I_{aS}}{I_S} \right)_{T_0} = - \frac{hc\tilde{\nu}_{mol}}{k_B} \left( \frac{1}{T_0 + \Delta T} - \frac{1}{T_0} \right) \quad (2)$$

Before applying Eq. (2) to determination of transient temperature rise following illumination of the heat pulse, we examined the accuracy of stationary temperature determination based on Eq. (2) from 20.0°C to 75.0°C in the following; the stationary temperature was measured by a calibrated alumel-chromel thermocouple (accuracy:  $\pm 0.1^\circ\text{C}$ ) and was compared with the temperature calculated by Eq. (2).

Molybdate solution was excited by the second harmonics of a Q-switched Nd:YAG laser while both Stokes and anti-Stokes Raman spectra were obtained simultaneously.

### 2.1.2 CHOICE OF RAMAN MEDIA

NIR pulses can be generated by stimulated Raman scattering (SRS) as the first Stokes lines of Raman media from the fundamental (1.064  $\mu\text{m}$ ) of a Nd:YAG laser. The presence of low thresholds for self-focusing and optical breakdown in solids and liquids as well as appearance of bubbles in liquids make it impossible to use these media as high-efficiency converters for SRS. Gases are suitable for Raman media for this purpose, because these problems are less severe in gases. Hydrogen<sup>4,9</sup> and methane<sup>5-8</sup> are, most of all, widely used and deuterium is also usable as Raman-medium gases both for their relatively large Raman gain coefficients and for large energy shifts;  $\tilde{\nu} [\text{H}_2, \text{Q}(1)] = 4155 \text{ cm}^{-1}$ ,  $\tilde{\nu} [\text{D}_2, \text{Q}(2)] = 2987 \text{ cm}^{-1}$ ,  $\tilde{\nu} [\text{CH}_4, \text{Q}] = 2917 \text{ cm}^{-1}$ . The NIR wavelengths of the first Stokes lines of  $\text{H}_2$ ,  $\text{D}_2$  and  $\text{CH}_4$  by excitation with 1.064  $\mu\text{m}$  is 1.89  $\mu\text{m}$ , 1.56  $\mu\text{m}$ , and 1.54  $\mu\text{m}$ , respectively. However, photo-reactive materials like  $\text{CH}_4$ , which undergoes photodissociation upon excitation by intense pump pulses, get more critical problems<sup>15</sup> than  $\text{H}_2$  and  $\text{D}_2$  in successive generation of NIR with prolonged pumping. Therefore, we utilized  $\text{H}_2$  and  $\text{D}_2$  gases as Raman media for generation of NIR in the laser-induced T-jump experiments.

---

<sup>1</sup> We tried successive generation of 1.54- $\mu\text{m}$  NIR with compressed methane: at 10-Hz repetition in Configuration (A) and (B) (shown later). By prolonged pumping with 1.064- $\mu\text{m}$  light of 560 mJ, an inside-window surface of a Raman shifter was damaged in the two configurations. The reason of this damage is considered that photo-dissociated carbon atoms formed particles, which stuck to the inside surface of windows, and that the carbon particles were burned by intense pump light.

### 2.1.3 REQUISITE INTENSITY OF HEAT PULSE AND SAMPLE THICKNESS FOR T-JUMP

It is quite important to heat a sample uniformly, but temperature gradient is produced because the intensity of a heat pulse decreases as it proceeds from the surface to inside due to absorption. To overcome this problem, it is helpful to illuminate the sample from both sides with two heat pulses. Moreover sample thickness is also an important factor for uniformly heating. Thin samples must be used for illumination of heat pulses with large absorption coefficient of water. Absorption coefficients of water at 1.89  $\mu\text{m}$  and at 1.56  $\mu\text{m}$  are  $61\text{ cm}^{-1}$ <sup>†</sup> and  $4\text{ cm}^{-1}$ ,<sup>2</sup> respectively. Accordingly, about 15-times thicker samples can be used for 1.56- $\mu\text{m}$  heating than that for 1.89- $\mu\text{m}$  heating under the same heating conditions.

Suppose that the intensity of a heat pulse is 100 mJ and that the sample is illuminated by equally divided pulses (50 mJ) from both sides by counter-propagating geometry, as illustrated in the upper part of Figure 2-1. The temperature profiles of the illuminated volume calculated with the values of absorption coefficients of water mentioned above are delineated in the lower part of Figure 2-1, where the conditions are as follows; (A) 140- $\mu\text{m}$  thick water is heated by 1.89- $\mu\text{m}$  pulses with 3-mm diameter and (B) 2-mm thick water is heated by 1.56- $\mu\text{m}$  pulses with 1.5-mm diameter. The averaged temperature rise by 1.89- $\mu\text{m}$  pulses and that by 1.56- $\mu\text{m}$  pulses are estimated to be 20.8°C and 5.7°C, respectively. To attain T-jump more than 5°C, 30 mJ of one 1.89- $\mu\text{m}$  pulse or 100 mJ of one 1.56- $\mu\text{m}$  pulse is totally necessary in the heating conditions as shown in Figure 2-1. Moreover, to satisfy the condition of uniform heating

---

<sup>†</sup> It was determined from absorbance of water at 1.89- $\mu\text{m}$  light with 25- $\mu\text{m}$ , 50- $\mu\text{m}$ , 100- $\mu\text{m}$ , and 200- $\mu\text{m}$  thickness.



of a sample, its thickness should be several hundred-micrometer for 1.89- $\mu\text{m}$  heating or several millimeter for 1.56- $\mu\text{m}$  heating; uncertainties of temperatures are 4.7°C (22%) in panel (A) and 1.1°C (20%) in panel (B).

## **2.2 EXPERIMENTAL PROCEDURES**

### **2.2.1 WAVELENGTH CONVERSION WITH HYDROGEN AND DEUTERIUM**

The excitation pulse of 1.064  $\mu\text{m}$  which pumped  $\text{H}_2$  or  $\text{D}_2$  was obtained from a Q-switched Nd:YAG laser (GCR-150, Spectra Physics). The pump energy was 560 mJ at 10 Hz and its pulse width was 9 ns (FWHM). To generate NIR pulses by stimulated Raman scattering, we applied three types of configurations as illustrated in Figure 2-2; (A) a single-pass configuration, (B) a half-resonator configuration, and (C) a seeding-amplification configuration. For the generation of 1.89- $\mu\text{m}$  NIR by  $\text{H}_2$ , Configuration (A) was sufficient. However, for generation of 1.56- $\mu\text{m}$  NIR with  $\text{D}_2$ , Configurations (A) and (B) were insufficient and Configuration (C) was indispensable. Hereafter we call a compressed gas cell used for wavelength conversion by SRS as a Raman shifter.

Figure 2-2(A) shows the single pass configuration, in which the first Stokes line is generated by spontaneous Raman scattering and amplified within the same pump pulse by self-seeding. The pump pulse was focused by a lens ( $\text{L1}$ ,  $f = 600$  mm) into a Raman shifter (RS1). RS1 is a 1.0-m long gas cell made of type-304 stainless steel with 12-mm inside effective diameter. Fused silica windows with 25.9-mm diameter and 20.0-mm width are used at the entrance and the exit of RS1 and are sealed by O-ring with flanges. The out-going pulses were collimated with a lens ( $\text{L2}$ ,  $f = 600$  mm) and separated by a Pellin-Broca prism (PBP) into pump, Stokes and anti-Stokes pulses.

Figure 2-2(B) shows the half-resonator configuration,<sup>15,16</sup> which uses an injection-seeding technique. A dichroic mirror (DM) and a mirror (M2) were added to the single-pass configuration in Figure 2-2(A); DM reflects 98.5 % at 1.56  $\mu\text{m}$  and transmits 95 % at 1.064  $\mu\text{m}$  for 45° incidence, and M2 completely reflects 1.56- $\mu\text{m}$  light. The half-resonator configuration makes the backward first SRS reflected back into RS1 by M2 and utilizes it as a seeding pulse, which is amplified within the same pump pulse. The temporal walk-off between the reflected seed and original pump pulses was 5 ns.

Figure 2-2(C) shows the seeding-amplification configuration<sup>10-12,16,17</sup> in this experiment. The pump pulse was split into about 1:5 by a beam-splitter (BS) with variable reflection-ratio. The weak portion was focused by a lens (L3,  $f = 1000$  mm) into RS1 and a seed pulse of the first Stokes line was yielded through SRS. This seed pulse was collimated once with a convex lens (L4,  $f = 500$  mm) and then expanded to the same size as the other portion of the split pump pulse with a combination of a concave and convex lens (L5,  $f = -100$  mm; L6,  $f = 300$  mm). The seed pulse was overlain on the pump pulse spatially and temporarily by a dichroic mirror (DM). The seed pulse and the pump pulse were focused by a lens (L7,  $f = 800$  mm) into an amplification Raman shifter (RS2), which is a 1.1-m long gas cell made of type-304 stainless steel with 20-mm inside effective diameter. Fused silica windows used at the entrance and the exit of RS2 are AR-coated broadband filter from 1050 nm to 1600 nm (transmission > 99%) with 38.1-mm diameter and 19.1-mm-thickness. Pressures of compressed gas filled in RS1 and RS2 were set equal to make the wavelengths of the seeding and amplified NIR pulses coincide.<sup>18</sup> This pressure adjustment improves the conversion efficiency from the pump pulse to the first Stokes line. The out-going pulses were collimated with a lens (L8,  $f = 600$  mm) and separated by PBP into pump, Stokes

and anti-Stokes pulses.

### 2.2.2 SAMPLE AND ILLUMINATION GEOMETRY

For T-jump induced by 1.89- $\mu\text{m}$  heat pulses, 100- $\mu\text{m}$  thick sample-cell with 1-mm thick quartz windows was used. The 1.89- $\mu\text{m}$  heat pulse dispersed with the Pellin-Broca Prism (62 mJ) and one reflected at the surface of the prism (8 mJ) were used in the Configuration (A) in Figure 2-2 with  $\text{H}_2$ . These two pulses were incident into the sample cell from both sides with 45°-upward geometry. Energies of these heat pulses were not equal in this experiment and therefore the lower-energy pulse was more tightly focussed (diameter: 1.1 mm) at the sample point than the high-energy one (diameter: 2.3 mm). Each beam size was determined as a spot size with a burning paper. A beam size depicted hereafter was determined by the same procedure. The actual path length through the sample along the propagation direction of heat pulses was 140  $\mu\text{m}$  in this incident configuration.

The Raman probe pulse was introduced to the sample cell so as to propagate co-linearly with the high-energy heat pulse (diameter at the sample point: 1.3 mm). The energy of Raman probe pulse was 5 mJ. Uncertainty due to the slightly-larger diameter of the probe pulse than that of the low-energy heat pulse was negligible in this experiment because the Raman scattering was mainly collected from the center of heated volume. The sample was circulated with a peristaltic pump between the cell and a sample reservoir, which was kept at 25.0°C by circulating temperature-controlled water. Between the peristaltic pump and the cell, two glass tubes were inserted as pressure reservoirs to remove pulsating flow. The averaged flow speed was 150 cm/s in the cell.

For T-jump induced by 1.56- $\mu\text{m}$  heat pulses, 2-mm thick sample-cell with 1-

mm thick quartz windows was used. The heat pulse (135 mJ) at 1.56  $\mu\text{m}$  obtained in Configuration (C) with  $\text{D}_2$  was split into two equal pulses with a 50:50-beam splitter. They were incident into the sample cell from both sides with up-and-down-counter-propagating geometry. The diameter of each pulse was 1.4 mm at the sample point. The Raman probe pulse, which was propagated collinearly with the up-going heat pulse, was focused below the sample cell before it illuminates the sample. This defocusing configuration prevented the Raman probe pulse from destroying cell windows through thermal lens effects induced by heat pulses. This problem was more crucial in the 1.56- $\mu\text{m}$  heating due to thicker sample than in the 1.89- $\mu\text{m}$  heating. By the use of a cylindrical lens, the shape of Raman probe pulse was modified to an elliptical shape at the sample point, where the major axis of ellipsoid was directed to the collecting optics of Raman scattering. The lengths of major and minor axes were 1.2 mm and 0.5 mm, respectively. The energy of Raman probe pulse was lowered to 3 mJ. The cell was held with brass blocks and the temperature of sample was kept at 25.0°C by circulating temperature-controlled water into the brass blocks. Thermal-conductive sheet was inserted between the cell and the brass blocks to improve thermal exchange. Sample was stirred by a small magnetic stirrer which was inserted into the brass blocks.

### **2.2.3 MEASUREMENTS OF TIME-RESOLVED RAMAN SPECTRA**

Raman scattering of molybdate ions were excited by the second harmonic (532 nm) of a Q-switched Nd:YAG laser (Spectra Physics, GCR-11) with the pulse width of 7 ns. The delay time ( $\Delta t$ ) of the Raman probe pulse following the illumination of the heat pulses was controlled by a pulse generator (Stanford Research Systems, DG535). The backward-scattered light in 1.89- $\mu\text{m}$  heating or 90°-scattered light in 1.56- $\mu\text{m}$  heating was collected and focused onto an entrance slit of a 25-cm single imaging

spectrograph (Chromex, 250IS). The width of the entrance slit was 100  $\mu\text{m}$ , while widths of the image were 2.7 and 1.3 mm in the 1.89- and 1.56- $\mu\text{m}$  heating experiments, respectively. Therefore, the Raman scattering from the most heated volume (central part) was collected. A holographic notch filter (Kaiser Optical Systems, Super Notch-Plus) and an iris were inserted between the entrance of the spectrograph and the sample-cell to reduce the stray light. A quartz polarization scrambler was placed in front of the entrance slit to remove the effect of polarization from the spectrograph throughput. In case of the 90°-scattering geometry in 1.56- $\mu\text{m}$  heating, another variable rectangular slit was placed by the side of the sample cell to reduce the stray light and Raman scattering of quartz windows more effectively. The dispersed light by the spectrograph was detected with an intensified photodiode array (EG&G PARC, model 1421). Both Stokes and anti-Stokes transient Raman spectra were obtained simultaneously.

One cycle of T-jump experiments involved a series of spectral measurements along increasing  $\Delta t$  and decreasing  $\Delta t$  and, in addition, the probe-only spectrum was measured at the end of individual series. In 1.89- $\mu\text{m}$  heating, we measured one set of transient Raman spectra that were the sum over 5 cycles. Total accumulation time at each delay was 20 minutes. In 1.56- $\mu\text{m}$  heating, we measured three sets of transient Raman spectra that were the sum over 3 cycles at each set. Total accumulation time at each delay was 6 minutes for each set.

## **2.3 RESULT**

### **2.3.1 ACCURACY OF TEMPERATURE DETERMINATION**

Molybdate ions in solution give sharp Raman bands at 317  $\text{cm}^{-1}$  and at 897  $\text{cm}^{-1}$ , and a broad band at 837  $\text{cm}^{-1}$ .<sup>19</sup> Figure 2-3 delineates the stationary Stokes and anti-

Stokes Raman spectra of  $\text{Na}_2\text{MoO}_4$  aqueous solution (1.5 M) in the upper and lower panels, respectively; at 75.0°C (*A* and *A'*) and at 20.0°C (*B* and *B'*). The spectral intensities are normalized in terms of the intensity of Stokes 897- $\text{cm}^{-1}$  band at 20.0°C in the two panels. The ordinate scale of the anti-Stokes Raman spectra (*A'*) and (*B'*) is magnified by four times of that of Stokes ones (*A*) and (*B*). All the Raman spectra from 20.0°C to 75.0°C were fitted to determine the temperatures of the sample according to Eq. (2); 317- and 897- $\text{cm}^{-1}$  bands by Lorentzian functions and 837- $\text{cm}^{-1}$  band by a Gaussian function. By using 20.0°C as reference temperature  $T_0$ , the temperature differences from  $T_0$ ,  $\Delta T_{obs}$ , were obtained from ratios of intensity of anti-Stokes bands,  $I_{as}$ , to that of Stokes bands,  $I_s$ . The intensity of  $I_s$  and  $I_{as}$  at each temperature was calculated from the fitted parameters. Dotted lines in Figure 2-3 delineate both base lines and fitted Raman bands at 317, 837 and 897  $\text{cm}^{-1}$ .

Comparison of the temperatures obtained according to Eq. (2),  $T_{obs}$  ( $= \Delta T_{obs} + T_0$ ), with the temperatures measured with thermocouple,  $T_{tc}$  is displayed in Figure 2-4, which plots  $T_{obs}$  derived from the 317- and the 897- $\text{cm}^{-1}$  bands against  $T_{tc}$ . We did not use the 837- $\text{cm}^{-1}$  band to determine  $T_{obs}$  because its intensity obtained by fitted spectra contained more uncertainty than those of 317- and the 897- $\text{cm}^{-1}$  bands due to the overlaps between intense 897- $\text{cm}^{-1}$  and broad 837- $\text{cm}^{-1}$  bands. It is recognized from the upper panels of (*A*) and (*B*) in Figure 2-4 that the discrepancy between  $T_{obs}$  and  $T_{tc}$  are within 1.5°C from 20.0°C to 75.0°C for 317- (*A*) and the 897- $\text{cm}^{-1}$  (*B*) bands. This result confirms that temperatures of the sample based on the relationship of Eq. (2) can be determined within the accuracy of 1.5°C in the temperature range from 20.0°C to 75.0°C from 317- and the 897- $\text{cm}^{-1}$  bands in the present apparatus.

### 2.3.2 CHARACTERISTICS OF GENERATED 1.89- $\mu\text{m}$ PULSE

Hydrogen gas at 3.0 MPa was compressed into RS1 for generation of a 1.89- $\mu\text{m}$  heat pulse. By using the single pass configuration, Configuration (A) in Figure 2-2, 70-mJ pulses at 1.89- $\mu\text{m}$  were obtained as the forward output at 10 Hz. Intensity fluctuation among generated 1.89- $\mu\text{m}$  pulses was within 10 %. The profile of the output 1.89- $\mu\text{m}$  pulse was not Gaussian shape but was a shape like two combined half-moons with low-energy distribution at the center. The surface temperature of RS1 around the focused point of the pump pulse was raised by prolonged pumping.

The highest output energy of the 1.89- $\mu\text{m}$  heat pulse was obtained at the hydrogen pressure of 3.0 MPa in the range from 1.0 MPa to 5.0 MPa. The output under 1.0 MPa of hydrogen was very low (16 mJ) and increased as raising of hydrogen pressure. The output was, however, slightly dependent on hydrogen pressure between 2.0 MPa and 5.0 MPa; 46 mJ at 2.0 MPa and 43 mJ at 5.0 MPa. Its fluctuation and its beam-profile were barely dependent in this pressure range.

### 2.3.3 CHARACTERISTICS OF GENERATED 1.56- $\mu\text{m}$ PULSE

**Generation by a Single Raman Shifter.** Deuterium gas at 3.5 MPa was compressed into RS1 for generation of 1.56- $\mu\text{m}$  pulse. By using Configuration (A), however, the forward output of 1.56- $\mu\text{m}$  pulse was of very low energy (10 mJ) at 10 Hz and, moreover, it fluctuated intensely among generated pulses in terms of its energy and beam-profile. The conversion efficiency of the pump pulse to the 1.56- $\mu\text{m}$  pulse by  $\text{D}_2$  was much less than that to the 1.89- $\mu\text{m}$  pulse by  $\text{H}_2$  in Configuration (A). The forward radiation pulses from RS1 contained many components with different wavelengths. Large amount of backward radiation was also observed. The surface temperature of RS1 around the focused point of the pump pulse was raised by prolonged pumping as was

observed in the 1.89- $\mu\text{m}$  generation in Configuration (A). The forward output energy of the 1.56- $\mu\text{m}$  pulse, its fluctuation among generated pulses, and its beam-profile were barely dependent on deuterium pressure in the range from 1.1 MPa to 3.5 MPa. Temperature rise of RS1 was also observed in this pressure range of  $\text{D}_2$ .

To obtain more intense pulse at 1.56  $\mu\text{m}$ , we examined the half resonator, Configuration (B) in Figure 2-2, with 3.5 MPa of  $\text{D}_2$ . The results were improved in comparison with the case of Configuration (A); 25-mJ pulse of 1.56- $\mu\text{m}$  NIR was obtained at 10 Hz as forward output. However, the energy of 1.56- $\mu\text{m}$  pulse reduced to 10 mJ with large intensity fluctuation after 20-minute pumping. Although the intensity of first Stokes light was practically increased by Configuration (B) with  $\text{D}_2$ , its energy was not sufficient for our purpose of T-jump and, moreover, its successive generation was lacking the long-term stability.

**Generation by Seeding-Amplification.** Finally, we examined the seeding-amplification configuration, Configuration (C) in Figure 2-2, with the pressure of RS1 and RS2 at 3.5 MPa. By adjusting the splitting ratio of the pump pulse with BS, we obtained 135-mJ pulses of 1.56  $\mu\text{m}$  at 10-Hz repetition as the forward first SRS radiation, which was more than ten times larger than that obtained by Configuration (A). The successive generation of 1.56- $\mu\text{m}$  pulses was stable for a period longer than half a day. Intensity fluctuation among generated 1.56- $\mu\text{m}$  pulses was suppressed within 10%. The output pulses from RS2 consisted of two kinds of clearly separated lights; ones were higher-order anti-Stokes shifted (second, third and fourth) lights with ring-shapes, and the others were first Stokes shifted light, pump light and first anti-Stokes shifted light with round shapes. The second Stokes scattering (2.9  $\mu\text{m}$ ) was not observed in this experiment because presumably it was absorbed by the glass of the optics. No backward



scattering from RS2 was recognized.

Configuration (C) also improved the beam-profile of the forward 1.56- $\mu\text{m}$  pulse. Though its profile was not absolutely a Gaussian-shape, the intensity maximum was located near the center and intensity decreased as going away from the center. The output-beam profile in Configuration (C) was much better than that of 1.89- $\mu\text{m}$  or 1.56- $\mu\text{m}$  in Configuration (A). No temperature rise of RS2 surface around the focused point of pump and seed pulses was recognized in Configuration (C) even after prolonged pumping of  $\text{D}_2$ . This sharply contrasts with the observed temperature rise in configuration (A) with  $\text{H}_2$  or  $\text{D}_2$ .

#### 2.3.4 TRANSIENT TEMPERATURE CHANGE BY ILLUMINATION OF HEAT PULSE

**T-jump with 1.89- $\mu\text{m}$  NIR.** Time-resolved Raman ( $\text{TR}^2$ ) spectra of  $\text{MoO}_4^{2-}$  solution (1.5 M) after illumination of two 1.89- $\mu\text{m}$  heat pulses were obtained in backward scattering geometry with delay times from  $-1\ \mu\text{s}$  to 10 ms. Figure 2-5 shows  $\text{TR}^2$  spectra of  $\text{MoO}_4^{2-}$  solution just before and after the illumination of heat pulses; (A, A' and A'') at  $-20\ \text{ns}$  and (B, B' and B'') at  $20\ \text{ns}$ .<sup>§</sup> Anti-Stokes spectra (A' and B') and

---

<sup>§</sup> Relative intensity of the  $897\text{-cm}^{-1}$  band to the  $317\text{-cm}^{-1}$  band in Figure 2-5 is different from those in Figure 2-3 and Figure 2-7. This difference is caused by the difference in the angle between the polarization direction of Raman probe light and the collecting direction of scattered light; the angle with respect to the vertical axis was  $90^\circ$  for Figures 2-3 and Figure 2-7 but  $60^\circ$  for Figure 2-5. The  $897\text{-cm}^{-1}$  band is polarized but the  $317\text{-cm}^{-1}$  band is depolarized.<sup>19</sup> The polarized component in the geometry for Figure 2-5 is relatively unfavorable than the polarized component in the geometry for Figure 2-3 and Figure 2-7 because a component of polarized Raman scattering which is parallel to the collecting direction is not detected. However, this difference in polarization component is irrelevant to the temperature determination based on Eq. (2), because Eq. (2) is valid irrespective of polarization components

( $A''$  and  $B''$ ) are magnified in the ordinate scale by 4-times and 20-times, respectively, of those of Stokes spectra ( $A$  and  $B$ ). Before calculating transient intensities of  $\text{MoO}_4^{2-}$  bands, quartz spectrum, which was measured after this T-jump measurement without illumination of heat pulses, was subtracted from  $\text{TR}^2$ -raw spectra obtained. The transient band intensities of  $\text{MoO}_4^{2-}$  were calculated in the same way with the steady-state measurements of  $\text{MoO}_4^{2-}$ . Transient temperatures  $\Delta T(t)$  at delay time  $t$  from the reference temperature  $T_0$  (25.0°C) were obtained according to Eq. (2). In all the time region from  $-1 \mu\text{s}$  to 10 ms,  $\Delta T(t)$  were determined with the  $897\text{-cm}^{-1}$  band. Transient temperature  $\Delta T(t)$  from 500 ns to 50  $\mu\text{s}$  were not determined correctly from the  $317\text{-cm}^{-1}$  band because stray light of the probe pulse increased in this time region. The band at  $837 \text{ cm}^{-1}$  was not used in this procedure for the same reason in the steady-state measurements.

Figure 2-6 plots the transient temperature  $\Delta T(t)$  in nanosecond region ( $A$ ) and in longer time region ( $B$ , logarithmic scale in the abscissa) following the illumination of two  $1.89\text{-}\mu\text{m}$  heat pulses. The filled and open circles denote  $\Delta T(t)$  determined from  $317\text{-}$  and  $897\text{-cm}^{-1}$  bands, respectively. Good agreement between filled and open circles shows that Eq. (2) is applicable to transient temperature measurements. It is recognized that temperature rise as much as  $31^\circ\text{C}$  was obtained by  $1.89\text{-}\mu\text{m}$  heating and that the elevated temperature remained until 1 ms.

**T-jump with  $1.56\text{-}\mu\text{m}$  NIR.** Time-resolved Raman spectra of  $\text{MoO}_4^{2-}$  solution (1.5 M) after the illumination of two  $1.56\text{-}\mu\text{m}$  heat pulses were obtained in the  $90^\circ$ -scattering geometry with delay times from  $-200 \text{ ns}$  to 80 ms. Figure 2-7 shows  $\text{TR}^2$  spectra of  $\text{MoO}_4^{2-}$  solution just before and just after illumination heat pulses; ( $A$ ,  $A'$  and  $A''$ ) at  $-20 \text{ ns}$  and ( $B$ ,  $B'$  and  $B''$ ) at 20 ns. Anti-Stokes spectra ( $A'$  and  $B'$ ) and ( $A''$  and

$B''$ ) are magnified in the ordinate scale by 4-times and 20-times, respectively, of those of Stokes spectra ( $A$  and  $B$ ).  $TR^2$  spectra presented were used for calculating the band intensities of  $MoO_4^{2-}$  without any manipulation, because Raman scattering from quartz windows was well rejected spatially by the rectangular slit beside the sample cell as well as optically by the Notch filter. This slit also removed the stray light so effectively that the intensities of  $317\text{-cm}^{-1}$  bands were determined correctly in the time region from 500 ns to 50  $\mu\text{s}$  in spite of increased stray light. The procedures of determining transient temperatures  $\Delta T(t)$  from the reference temperature ( $25.0^\circ\text{C}$ ) were the same as those in the previous  $1.89\text{-}\mu\text{m}$  T-jump experiment. Raman bands at  $317\text{-}$  and  $897\text{-cm}^{-1}$  were used for this procedure but the band at  $837\text{-cm}^{-1}$  was not due to the same reason as explained for the steady-state measurements. Three sets of  $\Delta T(t)$  were obtained from three independent T-jump measurements.

Figure 2-8 and Figure 2-9 plot transient temperature rises  $\Delta T(t)$  after the illumination of two  $1.56\text{-}\mu\text{m}$  heat pulses, which were obtained from the  $317\text{-}$  and  $897\text{-cm}^{-1}$  bands, respectively, in nanosecond region ( $A$ ) and in longer time region ( $B$ , logarithmic scale in the abscissa). The filled and open circles denote the average values of three sets of  $\Delta T(t)$  and error bars show the magnitude of dispersion among them. The observed temperature rises from  $317\text{-}$  and  $897\text{-cm}^{-1}$  bands are  $8.2^\circ\text{C}$  and  $9.2^\circ\text{C}$ , respectively, whose discrepancy is within the accuracy of temperature determination based on Eq. (2). When the cylindrical volume of which diameter and thickness are 1.4 mm (heat pulse) and 2 mm (sample-thickness), respectively, absorbs 84% of the total energy of the  $1.56\text{-}\mu\text{m}$  heat pulse (135 mJ), the temperature rise expected for the solution with specific heat  $1\text{ cal}/^\circ\text{C}$  is  $8.8^\circ\text{C}$ , which is in good agreement with the experimental value ( $8.2^\circ\text{C}$  and  $9.2^\circ\text{C}$ ). Figure 2-8 and Figure 2-9 show that the elevated

temperature remained until 10 ms. It is noted, however, that temperatures in the negative delay time region are higher than reference temperature by 2.7°C in Figure 2-8 and by 2.4°C in Figure 2-9. However, the probe-only spectrum at the end of the series of 1.56- $\mu\text{m}$  T-jump measurements indicated the recovery of the laser-induced elevated temperature to the reference temperature. Therefore this raised temperature in the negative delay time region is attributed to insufficient heat conduction between the solution and the cell holder under successive heating at 10 Hz. Despite the insertion of a thermo-conductive sheet, the solution was slightly heated.

## 2.4 DISCUSSION

### 2.4.1 EFFECT OF SEEDING-AMPLIFICATION

In Configuration (A) in Figure 2-2, NIR pulses by  $\text{H}_2$  were generated with high energy and with high pulse-to-pulse stability, but those by  $\text{D}_2$  were not. Configuration (C) was indispensable for  $\text{D}_2$  to improve the conversion efficiency, pulse-to-pulse stability, and beam-profile. We discuss thereby about these operations in Configuration (C) from the next four points; (1) selective generation of light, (2) reduction of thermal gradient, (3) temporal and spatial overlap between seeding and pump pulses, and (4) contribution from generated anti-Stokes shifted light.

**(1) Selective Generation of Light.** For generation of intense light by SRS, two types of selectivity are important; one is nonlinear effect selectivity in forward SRS and the other is  $J$ -selectivity in the most intense  $Q(J)$ -band in generation of the first-shifted light. For the consideration into two kinds of selectivity, Raman gain coefficients are useful parameters<sup>20,21</sup> and its  $J$ -dependence is derived in Appendix for  $Q(J)$ -branches of  $\text{H}_2$  and  $\text{D}_2$ . From Eq. (A.2), the coefficients  $g_R[Q(J)]$  due to  $Q(J)$ -branches are

proportional as

$$g_R[Q(J)] \propto \frac{N_J(\tilde{\nu}_p - \tilde{\nu}[Q(J)])}{\Delta\tilde{\nu}_R[Q(J)]} \quad (3)$$

where  $N_J$  is the population of rotational level,  $J$ , in the electric and vibrational ground state,  $\tilde{\nu}_p$  is the wavenumber of pump light,  $\tilde{\nu}[Q(J)]$  is the wavenumber of  $Q(J)$ -branch and  $\Delta\tilde{\nu}_R[Q(J)]$  is Raman linewidth (FWHM). The refractive index is assumed to unity in Eq. (3). Table 2-I shows  $J$ -dependent Raman gain coefficients  $g_R[Q(J)]$  of  $H_2$  at 3.0 MPa and of  $D_2$  at 3.5 MPa calculated by Eq. (3)<sup>†</sup>. The wavenumbers of  $Q(J)$ -branches and rotational populations at room temperature in Table 2-I were calculated from Eq. (A.3) and Eq. (A.4), respectively, by using rotational-vibrational constants and nuclear degeneracy of  $H_2$  and  $D_2$  shown in Table 2-II. Raman linewidths in Table 2-I were calculated from Eq. (A.5) by using collisional-narrowing (A) and density-broadening (B) factors shown in Table 2-III.

At first we discuss about the selectivity of nonlinear effects. It is recognized from Table 2-I that the maximum value among  $g_R[Q(J)]$  of  $D_2$  (0.18 cmGW<sup>-1</sup> at  $J=2$ ) under 1.064- $\mu$ m pump is about 20% as large as that of  $H_2$  (0.94 cmGW<sup>-1</sup> at  $J=1$ ). Therefore energy of the pump light is less converted to the first Stokes-shifted light by  $D_2$  than by  $H_2$ . Accordingly, backward scattered lights would be more stimulated by backward SRS and backward SBS<sup>21</sup> in  $D_2$ . In fact a large amount of backward scattering was observed in Configuration (A) with  $D_2$ . This experimental result leads to the

---

<sup>†</sup> For this calculation we used  $g_R[H_2, Q(1)]$  of 2.64 cmGW<sup>-1</sup> and  $g_R[D_2, Q(2)]$  of 0.45 cmGW<sup>-1</sup> under 532-nm pump, reported by Ottusch *et al.*<sup>18</sup> They directly obtained these values by seeding-amplification technique. Raman gain coefficients of  $H_2$  and  $D_2$  were also given by Hanna *et al.*<sup>22</sup> The reported values of  $g_R[H_2, Q(1)]$  are essentially the same between these two papers. However, that of  $g_R[D_2, Q(2)]$  by Hanna *et al.* is about twice as that by Rockwell *et al.*

conclusion that backward generation of additional lights decreased energy conversion of the pump light to 1.56- $\mu\text{m}$  light in Configuration (A) with  $\text{D}_2$ . On the other hand, no backward scattering was observed in Configuration (C) with  $\text{D}_2$ . It indicates that the forward SRS overcame the backward SRS and backward SBS in Configuration (C) with  $\text{D}_2$  and, in other words, that selectivity in the forward SRS worked well. As a result, the conversion efficiency is much improved in Configuration (C) than that in Configuration (A).

Next we discuss about  $J$ -selectivity. Raman bands of  $\text{H}_2$  and  $\text{D}_2$  are separated among each  $Q(J)$ -branch even in high pressure at room temperature. The most intense branches at room temperature are originated from  $J=1$  for  $\text{H}_2$  and from  $J=2$  for  $\text{D}_2$ . However, intensity ratios among  $Q(J)$ -branches are very different between  $\text{H}_2$  and  $\text{D}_2$  because their rotational populations in electronic and vibrational ground state are remarkably different (Table 2-I). It results mainly in different  $J$ -dependence for  $g_R[Q(J)]$ . As for  $\text{H}_2$  it is recognized from Table 2-I that  $g_R[Q(J)]$  at  $J \neq 1$  are much smaller than that at  $J=1$ ; 14% at  $J=0$  and 12% at  $J=2$  relative to that at  $J=1$ . Therefore the energy depletion of the pump pulse due to  $Q(J)$ -transitions different from  $J=1$  can be neglected in Raman shifting with  $\text{H}_2$  and the first-Stokes shifted light due to  $Q(1)$ -transition is hence effectively generated. As for  $\text{D}_2$ , however,  $g_R[Q(J)]$  at  $J \neq 2$  are not so small relative to that at  $J=2$ ; 32% at  $J=0$ , 79% at  $J=1$ , 28% at  $J=3$ , and 25% at  $J=4$ . Therefore  $Q(J)$ -branches from  $J \neq 2$  would not be negligible for SRS in  $\text{D}_2$ . In fact the forward radiation pulses from RS1 contained many components with different wavelengths in Configuration (A) with  $\text{D}_2$ . From this result it is considered that additional lights were generated by SRS due to many components of  $Q(J)$ -branches in Configuration (A) with  $\text{D}_2$  and, in addition, their combinations would be also generated by four-wave-mixing

(FWM). By applying Configuration (C), however, the forward radiation pulses from RS2 consisted of clearly separated Stokes- and anti-Stokes-shifted lights. It indicates that SRS due to Q( $J$ )-branches of  $D_2$  at  $J=2$  suppressed those at  $J\neq 2$ . Therefore,  $J$ -selectivity in the most intense Q( $J$ )-branch of  $D_2$  worked well in Configuration (C) for the generation of 1.56- $\mu\text{m}$  NIR and, accordingly, improved the conversion efficiency.

**(2) Reduction of Thermal Gradient.** In the interaction region of gaseous molecules with pump light, molecules are vibrationally excited by Raman pumping and they would also photoreact by multiphoton absorption. Vibrational energy of excited molecules or recombination energy of dissociated atoms must be released as thermal energy to their surroundings. Therefore thermal gradient in the interaction region is established if the interval between successive pump pulses is not long enough for the released heat to be dissipated from the region. As a result, beam shapes of pump and generated pulses are distorted in passing through the interaction region and the conversion efficiency to the first Stokes-shifted light is reduced. In Configuration (A) with  $H_2$  and  $D_2$ , in fact, the beam shapes of the first-Stokes shifted outputs were far from Gaussian shapes and the surface temperature of RS1 around the focussed point of pump pulses was raised by prolonged pumping. It is considered that released thermal energy remained in the interaction region of  $H_2$  and  $D_2$  in Configuration (A) with successive pump pulses. Indeed, large intensity fluctuations were observed among generated first Stokes-shifted pulses in Configuration (A) with  $D_2$ . However it was not so large with  $H_2$ . These results show that the thermal gradient of gases is a much severer problem in  $D_2$  than in  $H_2$ . In Configuration (C) with  $D_2$ , however, the beam-shape of the 1.56- $\mu\text{m}$  pulse was refined and the striking improvement of pulse-to-pulse stability was obtained as well. Moreover, prolonged pumping did not raise the surface temperature of RS2 around

the focussed point of pump pulses. Consequently it is interpreted that Configuration (C) with D<sub>2</sub> reduced effectively the thermal gradient in the interaction region with the pump light and improved the beam quality in terms of shape and pulse-to-pulse stability.

### **(3) Temporal and Spatial Overlap between Seeding and Pump Pulses.**

The NIR generation in Configuration (C) with D<sub>2</sub> was much improved with regard to energy, beam shape, and pulse-to-pulse stability. Notable improvement was not obtained in Configuration (B) although it also used the seeding technique. Hence the reasons for the contrary results in two configurations are presumably associated with two kinds of overlaps between seed and pump pulses; one is temporal overlap and the other is spatial overlap. In fact the best overlaps were obtained temporally and spatially in Configuration (C) because the optical paths and beam sizes of two pulses could be adjusted independently. On the other hand, the temporal walk-off between pulses was 5 ns in Configuration (B). Moreover, two pulses would not be necessarily best overlapped spatially because the size of seed pulse could not be adjusted easily.

We would like to emphasize that the temporal overlap is an essential factor to generate the first Stokes-shifted light because the pump energy is depleted as the increase of its generation (saturation effect). If there is a slight temporal walk-off between the two pulses, the seed pulse would be amplified at an edge part of the pump pulse. Actually only slight improvement of conversion efficiency was obtained in Configuration (B) for generation of 1.56- $\mu$ m NIR with D<sub>2</sub> though the best overlap between the seed and pump pulses was estimated to be as much as 65% at their 5-ns difference in this experiment. This indicates that temporal overlap intensely affects the conversion efficiency in NIR generation with regard to saturation effect. Moreover the temporal difference of 5 ns resulted in reduction of output energy and of pulse-to-pulse



stability in prolonged pumping. Hence it is concluded that the best temporal overlap as well as the best spatial overlap between seeding and pump pulses improved the conversion efficiency in Configuration (C) with D<sub>2</sub>, and its improvement resulted in long-time stability of the generated NIR.

#### **(4) Contribution of Generated Anti-Stokes Shifted Light.**

In Configuration (C) with deuterium, observed beam profiles from RS2 were a round-shape for the first anti-Stokes shifted light and ring-shapes for the higher-order anti-Stokes shifted lights. The round-shape of the first anti-Stokes shifted light indicates that the first anti-Stokes light was mainly generated by SRS. Its generation, which actually reduces conversion efficiency to the first-Stokes shifted light, is believed to play an important role in depumping of vibrationally excited molecules (mainly,  $\nu=1 \rightarrow \nu=0$ ) and consequently to reduces thermal gradient in the interaction region of D<sub>2</sub> with pump light. The ring-shapes of higher-order anti-Stokes shifted lights indicate that they were generated mainly by FWM. Phase matching conditions for FWM would be satisfied with the focusing geometry of the seeding and pump pulses by the lens (L5) in Configuration (C). Therefore the higher-order anti-Stokes shifted lights would be decreased by replacing L5 by a longer conforcal lens.

### **2.4.2 OBSERVED TEMPERATURE CHANGES IN T-JUMP MEASUREMENTS**

#### **2.4.2.1 INCLINATION OF TEMPERATURE RISE**

The dotted line in Figure 2-6(4) represents temporal cross correlation between the 1.89- $\mu\text{m}$  heat (9 ns) and Raman probe (7 ns) pulses. The solid line shows the expected inclination of temperature rise from this cross correlation on the assumption that the energy dissipation of vibrationally excited water and thermal equilibration in the

illuminated volume are much faster than the temporal width of the heat pulses. It is recognized that the observed  $\Delta T(t)$  coincide very well with the expected inclination of temperature rise. The same depictions are used in Figure 2-8(A) and Figure 2-9(A) for 1.56- $\mu\text{m}$  T-jump experiments. The coincidences of observed  $\Delta T(t)$  with the expected behavior of temperature rise are also obtained in Figure 2-8(A) and Figure 2-9(A). From these results it is concluded that the energy of the 1.89- $\mu\text{m}$  or 1.56- $\mu\text{m}$  heat pulses was converted to equilibrated thermal energy within its pulse width (9 ns). This demonstrates that the nanosecond T-jump can be attained by the nanosecond 1.89- $\mu\text{m}$  or 1.56- $\mu\text{m}$  heat pulses.

#### 2.4.2.2 TEMPERATURE RECOVERY

We discuss about the origins of observed temperature recovery in a long time region of T-jump experiments for 1.89- $\mu\text{m}$  heating (Figure 2-6(B)) and 1.56- $\mu\text{m}$  heating (Figure 2-8(B) and Figure 2-9(B)). Possible origins of temperature recovery include (1) changes of thermal distribution in a sample and (2) replacement of heated volume by sample flowing. At first we discuss about contributions of temporal changes of thermal distribution without flowing and next those of sample-replacement by flowing.

**Temporal Changes of Thermal Distribution.** Thermal energy of heated volume is diffused in a sample as well as transferred to atmosphere through quartz windows. Therefore, even without flowing of sample, thermal distribution of heat energy changes by thermal diffusion and by thermal transfer. We distinguish these two contributions on the discussion about temporal changes of thermal distribution.

Temporal change of temperature is described by diffusion equation<sup>23</sup>,

$$\frac{\partial T}{\partial t} = \kappa \nabla^2 T \quad (4)$$

where  $T$  is temperature,  $\kappa$  is thermal diffusivity, and  $t$  is time. The thermal diffusivity  $\kappa$

is defined as

$$\kappa = \frac{K}{\rho c} \quad (5)$$

where  $K$  is thermal conductivity,  $\rho$  is density and  $c$  is heat capacity.

We assume that two heat pulses, which are equivalent and their beam-profiles are of Gaussian-shape, are illuminated to samples from both sides with counter-propagation geometry. This assumption is crude approximation for the 1.89- $\mu\text{m}$  T-jump experiment, but qualitative behavior of temporal temperature change can be investigated. Under this assumption, two-dimensional intensity distribution,  $I$ , of each heat pulse is represented in  $(r, \theta)$ -plane as

$$I(r, \theta) = \frac{E_0}{2} \frac{1}{2\pi\sigma^2} \exp\left(-\frac{r^2}{2\sigma^2}\right) \quad (6)$$

where the first term,  $E_0/2$ , is total energy of each heat pulse and the value  $2(2\sigma^2)^{1/2}$  is comparable length with a diameter of the heat pulse.

Let us set  $t = 0$  to be the time when a sample is illuminated by the two heat pulses from both sides. When sample thickness, which is equal to  $2l$ , is located in  $z$ -direction from  $-l$  to  $l$ , the temperature distribution at  $t=0$  is given in cylindrical coordinates  $(r, \theta, z)$  as

$$T(r, \theta, z, t = 0) - T_0 = 4\pi\sigma^2 l T_{avg} f(r, \theta, t = 0) g(z, t = 0) \quad (7)$$

The terms in the right side of Eq. (7) are represented as

$$T_{avg} = \frac{1}{2l} \int_{-l}^l dz T(r = 0, z, t = 0) = \frac{E_0(1 - \exp(-2al))}{4\pi\sigma^2 l \rho c} \quad (8)$$

$$f(r, \theta, t = 0) = \frac{1}{2\pi\sigma^2} \exp\left(-\frac{r^2}{2\sigma^2}\right) \quad (9)$$

$$\begin{aligned}
g(z, t=0) &= \frac{a \exp(az) + \exp(-az)}{2 \exp(al) - \exp(-al)} \\
&= \frac{a \exp(al) + \exp(-al)}{l \exp(al) - \exp(-al)} \sum_{n=0}^{\infty} \frac{(-1)^n k_{2n+1}}{a^2 + k_{2n+1}^2} \cos(k_{2n+1} z)
\end{aligned} \tag{10}$$

where  $k_{2n+1} = (2n+1)\pi/2l$ .  $T_0$  denotes temperature before illumination of heat pulses and  $T_{avg}$  is averaged temperature along  $z$ -direction at  $r=0$  immediately after the illumination. Functions  $f(r, \theta, t=0)$  and  $g(z, t=0)$  are the normalized distribution functions in  $(r, \theta)$ -plane and in  $z$ -axes, respectively. Parameter  $a$  is given by  $61 \times 2^{1/2} \times \ln 10 \text{ cm}^{-1}$  for the  $1.89\text{-}\mu\text{m}$  heating and  $4 \times \ln 10 \text{ cm}^{-1}$  for  $1.56\text{-}\mu\text{m}$  heating. The parameter  $a$  for  $1.89\text{-}\mu\text{m}$  heating is magnified by the factor  $2^{1/2}$ . The reason is that the  $1.89\text{-}\mu\text{m}$  pulses were illuminated at the angle of  $45^\circ$  against the sample thickness direction and hence the actual length along its propagating axes corresponds to that along  $z$ -axes multiplied by the factor  $2^{1/2}$ . Suppose that temperature at boundary is constant at  $T_0$ , the boundary conditions are represented as

$$T(r, \theta, z = \pm l, t) = T_0 \tag{11A}$$

$$T(r = \infty, \theta, z, t) = T_0 \tag{11B}$$

The diffusion equation (5) under the initial conditions (7)-(10) and the boundary conditions (11A), (11B) is solved<sup>23</sup> as

$$T(r, \theta, z, t) - T_0 = 4\pi\sigma^2 l T_{avg} f(r, \theta, t) g(z, t) \tag{12}$$

The temporal terms in the right side of Eq. (12) are represented as

$$f(r, \theta, t) = \frac{1}{2\pi(2\kappa t + \sigma^2)} \exp\left(-\frac{r^2}{2(2\kappa t + \sigma^2)}\right) \tag{13}$$

$$g(z, t) = \frac{a \exp(al) + \exp(-al)}{l \exp(al) - \exp(-al)} \sum_{n=0}^{\infty} \frac{(-1)^n k_{2n+1}}{a^2 + k_{2n+1}^2} \cos(k_{2n+1} z) \exp(-\kappa k_{2n+1}^2 t) \tag{14}$$

The time-dependent terms,  $f(r,\theta,t)$  and  $g(z,t)$ , represent the effects of thermal diffusion and thermal transfer, respectively.

We discuss thermal diffusion effect at first. Because the thermal diffusion term in  $(r,\theta)$ -plane,  $f(r,\theta,t)$ , is a time-dependent normal distribution function with expected value zero, the variance  $2(2\kappa t + \sigma^2)$  ( $= \langle r^2 \rangle_t$ ) determines the profile of  $f(r,\theta,t)$ . The value  $2(2\sigma^2)^{1/2}$  ( $= 2(\langle r^2 \rangle_{t=0})^{1/2}$ ) is crudely estimated to the observed beam diameter; 1.7 mm for the 1.89- $\mu\text{m}$  heat pulse, which is an averaged diameter of the two pulses utilized, and 1.4 mm for the 1.56- $\mu\text{m}$  heat pulse. Insertion of  $\kappa = 0.14 \text{ mm}^2\text{s}^{-1}$  at 25°C to Eq. (13) gives rise to  $2(\langle r^2 \rangle_t)^{1/2}$  at 100 ms to be 1.76 mm for 1.89- $\mu\text{m}$  T-jump and 1.48 mm for 1.56- $\mu\text{m}$  T-jump, respectively. These values suggest that the thermal diffusion within 100 ms is negligible in temperature recovery within the interval of successive T-jump at 10 Hz.

Next we discuss thermal transfer effect. The temporal behavior of thermal transfer term,  $g(z,t)$ , is extremely dependent on sample thickness. Figure 2-10 plots the temporal behaviors of the integral values of  $g(z,t)$  from  $-l$  to  $l$ ; (A)  $2l = 100 \text{ }\mu\text{m}$  and  $a = 61 \times 2^{1/2} \times \ln 10 \text{ cm}^{-1}$  for 1.89- $\mu\text{m}$  T-jump, (B)  $2l = 2 \text{ mm}$  and  $a = 4 \times \ln 10 \text{ cm}^{-1}$  for 1.56- $\mu\text{m}$  T-jump. Line (A) shows that the thermal transfer term  $g(z,t)$  is remarkably time-dependent within 100 ms in the 1.89- $\mu\text{m}$  T-jump. However, it cannot be concluded from this calculation only that the origin of temperature recovery within 100- $\mu\text{m}$  thickness is thermal transfer, because surface conductance from water to quartz windows is postulated to be infinite in the boundary conditions Eq. (11A).<sup>23</sup> Therefore we can say, at least, that thermal transfer is a possible origin of temperature recovery in a sample as thin as 100  $\mu\text{m}$ . On the other hand, it is recognized from Line (B) that time-dependence of  $g(z,t)$  within 100 ms is extremely small in a 2-mm thick sample in spite of high

conductance limit in boundary conditions Eq. (11A). Therefore it is concluded that thermal transfer within 100 ms is not a primary origin of temperature recovery in a sample as thick as 2 mm.

**Contribution of Sample Replacement by Flowing.** Second we discuss the effect of replacement of heated volume by flowing in 2.0-mm thick sample. From the above discussions, it can be assumed that the temperature distribution is practically constant within 100 ms in a 2.0-mm thick sample. Suppose that the sample flows at rate  $v$  along  $x$ -axes, which is perpendicular to the Raman collecting optics, the temperature distribution in  $(x,y)$ -plane is given by

$$T(x, y, t) - T_0 = T_{avg} \exp\left(-\frac{(x - vt)^2 + y^2}{2\sigma^2}\right) \quad (15)$$

Equation (15) is obtained from Eq. (12) by transformation from cylindrical coordinates  $(r, \theta, z)$  to rectangular coordinates  $(x, y, z)$  and then by integration along  $z$ -axes. The temperature difference,  $\Delta T_{obs}(t)$ , from  $T_0$  of the volume,  $V_{col}$ , from which Raman scattering is collected, is proportional to

$$\Delta T_{obs}(t) \propto \exp\left(-\frac{v^2}{2\sigma^2} t^2\right) \quad (16)$$

This equation is valid when the optical window along the  $x$  direction of  $V_{col}$  is much smaller than the length along the  $x$ -axis of heated volume. This condition was actually satisfied in the 1.56- $\mu\text{m}$  heating of this experiment because the entrance-slit width of spectrograph was much smaller than that of the image of scattered light on this slit.

Equation (16) predicts that the temperature recovery due to replacement of heated volume is represented by a Gaussian function against time. The solid lines in Figure 2-8(B) and Figure 2-9(B) represent the temporal behaviors of  $\Delta T_{obs}(t)$  according

to Eq. (16), where the identical coefficient against time is used. It is recognized that the expected temperature-recovery almost completely reproduces experimental points. This result means that the temperature recovery observed for longer delay times in the 1.56- $\mu\text{m}$  T-jump occurs by the replacement of the heated volume with fresh portion of the sample through flowing. It is hence concluded that the longer time limit of T-jump measurement in a sample as thick as 2 mm is determined by replacement of the sample by flowing, but not by thermal diffusion or by thermal transfer.

To examine the contribution of sample replacement to temperature recovery in the 100- $\mu\text{m}$  thick sample as in Figure 2-6(B), we made the experiment that the 1.89- $\mu\text{m}$  heat pulses illuminated the sample at 10-Hz repetition without sample flowing. It resulted in bubble-generation in the sample and in breaking cell windows. This means that the temperature of sample portion heated by 1.89- $\mu\text{m}$  pulses remained when the next 1.89- $\mu\text{m}$  pulses illuminated the sample. Thus the temperature recovery was not completed within 100 ms only by thermal transfer and temperature rise was additive. However, the temperature recovery was actually completed with sample flowing as depicted in Figure 2-6(B). Therefore it is concluded that in a sample as thin as 100  $\mu\text{m}$  the replacement of sample is one of factors determining the longer time limit of T-jump experiments as well as thermal transfer is.

### **2.4.3 INDUCED THERMAL EFFECTS UPON T-JUMP**

In the laser induced T-jump experiments, the stray light of the probe pulse increased in the time region from 500 ns to 50  $\mu\text{s}$  following the illumination of 1.89- $\mu\text{m}$  or 1.56- $\mu\text{m}$  heat pulses. The temporal behaviors of the  $\text{TR}^2$ -signals at 317- and 897- $\text{cm}^{-1}$  bands in the 1.56- $\mu\text{m}$  T-jump are depicted in Figure 2-11, where their transient band intensities are obtained from the fitted parameters in the determination of the transient

temperature. The two series of the experimental points in Figure 2-11 show that the increase of stray light was accompanied with the decrease in the amount of Raman signals that were collected. It has been known that a very rapid heating of a solution generates a shock wave due to rapid thermal expansion and that the cavitation effect induced by this shock wave occurs.<sup>3,24</sup> Therefore it is interpreted that the shock wave and the cavitation effect get crucial problems in the TR<sup>2</sup>-measurements, especially in terms of transient band intensities, though they are irrelevant to the transient temperature measurements according to Eq. (2). Figure 2-11, however, shows that the temporal changes in the band intensities at 317- and 897-cm<sup>-1</sup> cooperate well with each other. It means that TR<sup>2</sup>-spectra in the problematic region from 500 ns to 50  $\mu$ s can be calibrated with the temporal intensity behavior, which are obtained in Figure 2-11.

#### **2.4.4 APPLICABILITY TO RAMAN MEASUREMENTS OF PROTEIN**

Conformational changes of molecules in the initial steps of thermal excitation within millisecond can be pursued by the combination of laser induced T-jump and TR<sup>2</sup> spectroscopy. In fact we demonstrated that the two types of present T-jump apparatuses by 1.89- $\mu$ m or 1.56- $\mu$ m heat pulses are applicable to TR<sup>2</sup> measurements of MoO<sub>4</sub><sup>2-</sup> solution (1.5 M) in the time scales from nanoseconds to milliseconds. To examine their abilities to TR<sup>2</sup> measurements of proteins, we at first measured steady-state Raman spectra of bovine pancreatic ribonuclease A (RNase A) with the same geometry as that for TR<sup>2</sup> measurements of the MoO<sub>4</sub><sup>2-</sup> solution without illumination of heat pulses. The Raman spectra of RNase A obtained at 25.0°C are delineated in Figure 2-12; (A) 150-mg/ml solution with 100- $\mu$ m thickness and (B) 100 mg/ml solution with 2-mm thickness. The ordinate scales of spectra (A) and (B) are arbitrary. Accumulation time for each spectrum was 30 minutes. It is recognized at a glance that spectrum (B)



displays much better features than spectrum (A). Low frequency region of spectrum (A) could not be obtained due to the disturbance by Raman scattering of quartz windows and thus Raman bands of S-S and C-S stretching could not be measured with the 100- $\mu\text{m}$  thick sample. Tyrosine doublet in spectrum (B) was well resolved but that in spectrum (A) was buried in the disturbance of stray light. The clearer band of phenylalanine residues was given in spectrum (B) than in spectrum (A) although the band of sulfate ion could not be compared due to its different concentrations in (A) and (B). The S-S and C-S stretching bands as well as tyrosine doublet are important bands that are sensitive to conditions of side-chains and thus are expected to reflect protein structures as explained in Chapter 3. Accordingly, measurements of  $\text{TR}^2$  spectra in the frequency region from 400 to 900  $\text{cm}^{-1}$  are indispensable to discuss transient structure of RNase A involved in unfolding upon T-jump. For this purpose, the 2-mm thick sample can be utilized but 100- $\mu\text{m}$  thin sample can not be used as apparent from Figure 2-12. Therefore 1.56- $\mu\text{m}$  T-jump is applicable to  $\text{TR}^2$  experiments of protein unfolding but 1.89- $\mu\text{m}$  T-jump is not. For absorption, fluorescence, or ultraviolet resonance Raman measurements, the 100- $\mu\text{m}$  thick sample would be thick enough and, therefore, the 1.89- $\mu\text{m}$  T-jump is more suitable way for those experiments because larger T-jump is attained. The application of nanosecond T-Jump to  $\text{TR}^2$  study on thermal unfolding of RNase A is described in Chapter 3.

## 2.5 SUMMARY

We constructed two types of nanosecond temperature jump apparatuses applicable to time-resolved Raman measurements. At first we succeeded in successive generation (10 Hz) of high-energy heat pulses of two wavelengths (1.89  $\mu\text{m}$  and 1.56

$\mu\text{m}$ ) in prolonged operation by stimulated Raman scattering of  $\text{H}_2$  and  $\text{D}_2$ . The seeding-amplification technique was remarkably effective in progress of conversion efficiency, especially, for generation of  $1.56\text{-}\mu\text{m}$  heat pulses. This technique also supplied fluctuation-reduction among generated pulses and improvement of their beam quality. To the authors' knowledge, this is the first report of successive generation of nanosecond giant pulses at  $1.56\text{ }\mu\text{m}$ . Next we successfully applied  $1.89\text{-}\mu\text{m}$  and  $1.56\text{-}\mu\text{m}$  heat pulses to T-jump experiments. We obtained transient temperatures of heated volume directly from anti-Stokes/Stokes ratios of transient Raman spectra of  $\text{MoO}_4^{2-}$ . We made it sure that nanosecond temperature jump was attained by  $1.89\text{-}\mu\text{m}$  or  $1.56\text{-}\mu\text{m}$  heat pulses. The long-time limit of T-jump experiment for the sample as thick as  $2\text{ mm}$  was determined by sample replacements due to flowing, but not by thermal diffusion or thermal transfer. On the other hand, this limit for a sample as thin as  $100\text{ }\mu\text{m}$  might be determined by replacement of sample and by thermal transfer.

## APPENDIX

### *J*-Dependent Raman Gain Coefficients of *Q*(*J*)-Branches of $\text{H}_2$ and $\text{D}_2$

Raman differential cross sections of  $\text{H}_2$  and  $\text{D}_2$  is represented by the sum of the isotropic and anisotropic parts<sup>25-28</sup>. As for  $\text{H}_2$  and  $\text{D}_2$ , the anisotropic parts which are dependent on rotational levels, are negligible relative to isotropic parts<sup>29-31</sup> which are independent of rotational levels. Then the *J*-dependent Raman gain coefficients of *Q*(*J*)-branches<sup>21,32</sup> are proportional to

$$g_R[Q(J)] \propto \frac{N_J \tilde{\nu}_s [Q(J)]}{n_s^2 \Delta \tilde{\nu}_R [Q(J)]} \quad (\text{A.1})$$

where  $N_J$  is the population at the rotational level, *J*, in the electric and vibrational ground state,  $\tilde{\nu}_s$  is the wavenumber of Stokes light,  $\Delta \tilde{\nu}_R$  is Raman linewidth

(FWHM), and  $n_s$  is refractive index. Replacement of  $\tilde{\nu}_s$  in Eq. (A.1) with the wavenumber of pump light,  $\tilde{\nu}_p$ , and the wavenumber of Q(J)-branch,  $\tilde{\nu}[Q(J)]$ , yields Eq. (A.2).

$$g_R[Q(J)] \propto \frac{N_J (\tilde{\nu}_p - \tilde{\nu}[Q(J)])}{n_s^2 \Delta \tilde{\nu}_R[Q(J)]} \quad (\text{A.2})$$

The terms in the right side of Eq. (A.2) are given in the following.

$$N_J = \frac{g_J (2J+1) \exp\left(-\frac{hc}{k} \frac{F(J)}{T}\right)}{\sum_{J'} g_{J'} (2J'+1) \exp\left(-\frac{hc}{k} \frac{F(J')}{T}\right)} \quad (\text{A.3})$$

$$\tilde{\nu}[Q(J)] = \tilde{\nu}_{1-0} + (B_1 - B_0)J(J+1) - (D_1 - D_0)J^2(J+1)^2 \quad (\text{A.4})$$

$$\Delta \tilde{\nu}_R[Q(J)] = \frac{A[Q(J)]}{\rho} + B[Q(J)]\rho \quad (\text{A.5})$$

where  $g_J$  is the nuclear degeneracy<sup>33</sup> and  $F(J)$  is the energy of rotational level,  $J$ , which is represented<sup>34</sup> by

$$F(J) = B_0 J(J+1) - D_0 J^2(J+1)^2 \quad (\text{A.6})$$

Equation (A.4) of  $\tilde{\nu}[Q(J)]$  is given by Stoicheff<sup>34</sup>. Equation (A.5) of Raman linewidth,  $\Delta \tilde{\nu}_R[Q(J)]$ , is represented by the sum of a diffusion term (the first term) and a density-broadening term (the second term)<sup>35,36</sup>.

## REFERENCES

- 1 C. M. Phillips, Y. Mizutani, and R. M. Hochstrasser, *Proc. Natl. Acad. Sci. USA* **92**, 7292-7296 (1995).
- 2 J. V. Beitz, G. W. Flynn, D. H. Turner, and N. Sutin, *J. Am. Chem. Soc.* **92**, 4130-4132 (1970).
- 3 D. H. Turner, G. W. Flynn, N. Sutin, and J. V. Beitz, *J. Am. Chem. Soc.* **94**, 1554-1559 (1972).
- 4 S. Ameen, *Rev. Sci. Instrum.* **46**, 1209-1215 (1975).
- 5 A. P. Williams, C. E. Longfellow, S. M. Freier, R. Kierzek, and D. H. Turner, *Biochemistry* **28**, 4283-4291 (1989).
- 6 R. M. Ballew, J. Sabelko, C. Reiner and M. Gruebele, *Rev. Sci. Instrum.* **67**, 3694-3699 (1996).
- 7 M. Gruebele, J. Sabelko, R. Ballew, and J. Ervin, *Acc. Chem. Res.* **31**, 699-707 (1998).
- 8 P. A. Thompson, W. A. Eaton, and J. Hofrichter, *Biochemistry* **36**, 9200-9210 (1997).
- 9 I. K. Lednev, A. S. Karnoup, M. C. Sparrow, and S. A. Asher, *J. Am. Chem. Soc.* **121**, 4076-4077 (1999).
- 10 Y. Mizutani, K. Yamamoto, and T. Kitagawa, in *Old and New Views of Protein Folding*, edited by K. K. a. M. Arai (Elsevier, Amsterdam, 1999).
- 11 K. Yamamoto, Y. Mizutani, and T. Kitagawa, in *9th Intl. Conf. Time-Resolved Vibrational Spectroscopy* (Tucson, USA, 1999).
- 12 K. Yamamoto, Y. Mizutani, and T. Kitagawa, *Biophys. J.* (in press).
- 13 S. Williams, T. P. Causgrove, R. Gilmanishin, K. S. Fang, R. H. Callender, W. H. Woodruff, and R. B. Dyer, *Biochemistry* **35**, 691-697 (1996).
- 14 S. D. Rassat and E. J. Davis, *Appl. Spectrosc.* **48**, 1498-1505 (1994).
- 15 Z. Chu, U. N. Singh, and T. D. Wilkerson, *Opt. Commun.* **75**, 173-178 (1990).
- 16 S. E. Bisson, *Appl. Opt.* **34**, 3406-3412 (1995).
- 17 H. Konime and E. A. Stappaerts, *Opt. Lett.* **4**, 398-400 (1979).
- 18 J. J. Ottusch and D. A. Rockwell, *IEEE J. Quantum Electron.* **24**, 2076-2080 (1988).
- 19 K. Nakamoto, *Infrared and Raman Spectra of Inorganic and Coordination Compounds*, 5th ed. (John Wiley & Sons, Inc., Ney York, 1997).
- 20 N. Bloembergen, G. Bret, P. Lallemand, A. Pine, and P. Simova, *IEEE J. Quantum. Electron.* **QE-3**, 197-201 (1967).

- 21 W. Kaiser and M. Maier, in *Laser Handbook*, Vol. 2, edited by F. T. Arecchi and E. O. Schlz-DuBois (North-Holland Publ. Co., Amsterdam, 1972), pp. 1077-1150.
- 22 D. C. Hanna, D. J. Pointer, and D. J. Pratt, *IEEE J. Quantum Electoron.* **QE-22**, 332-336 (1986).
- 23 H. S. Carslaw and J. C. Jaeger, *Conduction of Heat in Solids*, 2nd ed. (Oxford University Press, Oxford, 1959).
- 24 M. Eigen and L. DeMaeyer, in *Technique of Organic Chemistry*, Vol. 8, edited by S. L. Friess, E. S. Lewis, and A. Weissberger (Interscience, New York, 1963), pp. 895-1054.
- 25 T. C. James and W. Klemperer, *J. Chem. Phys.* **31**, 130-134 (1959).
- 26 K. Altmann and G. Strey, *J. Mol. Spectrosc.* **44**, 571-577 (1972).
- 27 H. W. Schroetter and H. W. Kloeckner, in *Raman Spectroscopy of Gases and Liquids*, edited by A. Weber (Springer-Verlag, Berlin, 1979), pp. 123-166.
- 28 P. Baierl and W. Kiefer, *J. Raman Spectrosc.* **10**, 197-204 (1981).
- 29 D. M. Golden and B. Crawford, Jr., *J. Chem. Phys.* **36**, 1654-1661 (1962).
- 30 W. Kolos and L. Wolniewics, *J. Chem. Phys.* **46**, 1426-1432 (1967).
- 31 R. W. Carlson and W. R. Fenner, *Astrophys. J.* **178**, 551-556 (1972).
- 32 R. Loudon, *The Quantum Theory of Light*, 2nd ed. (Oxford University Press, Oxford, 1983).
- 33 H. Eyring, J. Walter, and G. Kimball, *Quantum Chemistry* (John Wiley & Sons, Inc, New York, 1944).
- 34 B. P. Stoicheff, *Can. J. Phys.* **35**, 730-741 (1957).
- 35 A. M. Toich, D. W. Melton, and W. B. Roh, *Opt. Comm.* **55**, 406-408 (1985).
- 36 D. A. Russell and W. B. Roh, *J. Mol. Spec.* **124**, 240-242 (1987).

**TABLE 2-I.** Raman gain coefficients of H<sub>2</sub> at 3.0 MPa and of D<sub>2</sub> at 3.5 MPa under 1.064- $\mu$ m excitation.

	H <sub>2</sub>				D <sub>2</sub>				
	Q(0)	Q(1)	Q(2)	Q(3)	Q(0)	Q(1)	Q(2)	Q(3)	Q(4)
$\tilde{\nu} / \text{cm}^{-1}$	4161.1	4155.2	4143.4	4125.8	2993.6	2991.4	2987.2	2980.9	2972.6
$N_j \%$	13.0	65.8	11.7	9.0	18.3	20.5	38.4	11.4	9.3
$\Delta\tilde{\nu}_R / \text{cm}^{-1}$	0.064	0.046	0.070	0.106	0.184	0.084	0.124	0.130	0.123
$g_R / \text{cmGW}^{-1}$	0.132	0.939 <sup>a</sup>	0.109	0.056	0.058	0.144	0.182 <sup>a</sup>	0.051	0.045

<sup>a</sup> See Reference 18

**Table 2-II.** Rotational and vibrational constants, and nuclear degeneracy of H<sub>2</sub> and D<sub>2</sub>.

		H <sub>2</sub>	D <sub>2</sub>
$B_0^a$	/cm <sup>-1</sup>	59.3392	29.9105
$D_0^a$	/cm <sup>-1</sup>	0.04599	0.01134
$\tilde{\nu}_{1-0}^a$	/cm <sup>-1</sup>	4161.137	2993.561
$B_1 - B_0^a$	/cm <sup>-1</sup>	-2.9752	-1.0623
$D_1 - D_0^a$	/cm <sup>-1</sup>	-0.00276	-0.00059
$g_J^b$	$J$ : even	1	6
	$J$ : odd	3	3

<sup>a</sup> See Reference 34

<sup>b</sup> See Reference 33

**Table 2-III.** Collisional-narrowing (A) and density-broadening (B) factors.

	$H_2^a$				$D_2^b$				
	Q(0)	Q(1)	Q(2)	Q(3)	Q(0)	Q(1)	Q(2)	Q(3)	Q(4)
$A / 10^{-1} \text{ cm}^{-1} \text{ m}^{-3} \text{ mol}$	8.17	6.91	7.36	7.41	8.44	6.68	6.90	8.31	7.03
$B / 10^{-5} \text{ cm}^{-1} \text{ m}^3 \text{ mol}^{-1}$	2.35	1.68	2.58	3.90	13.0	5.90	8.76	9.21	8.67

<sup>a</sup> See Reference 35

<sup>b</sup> See Reference 36



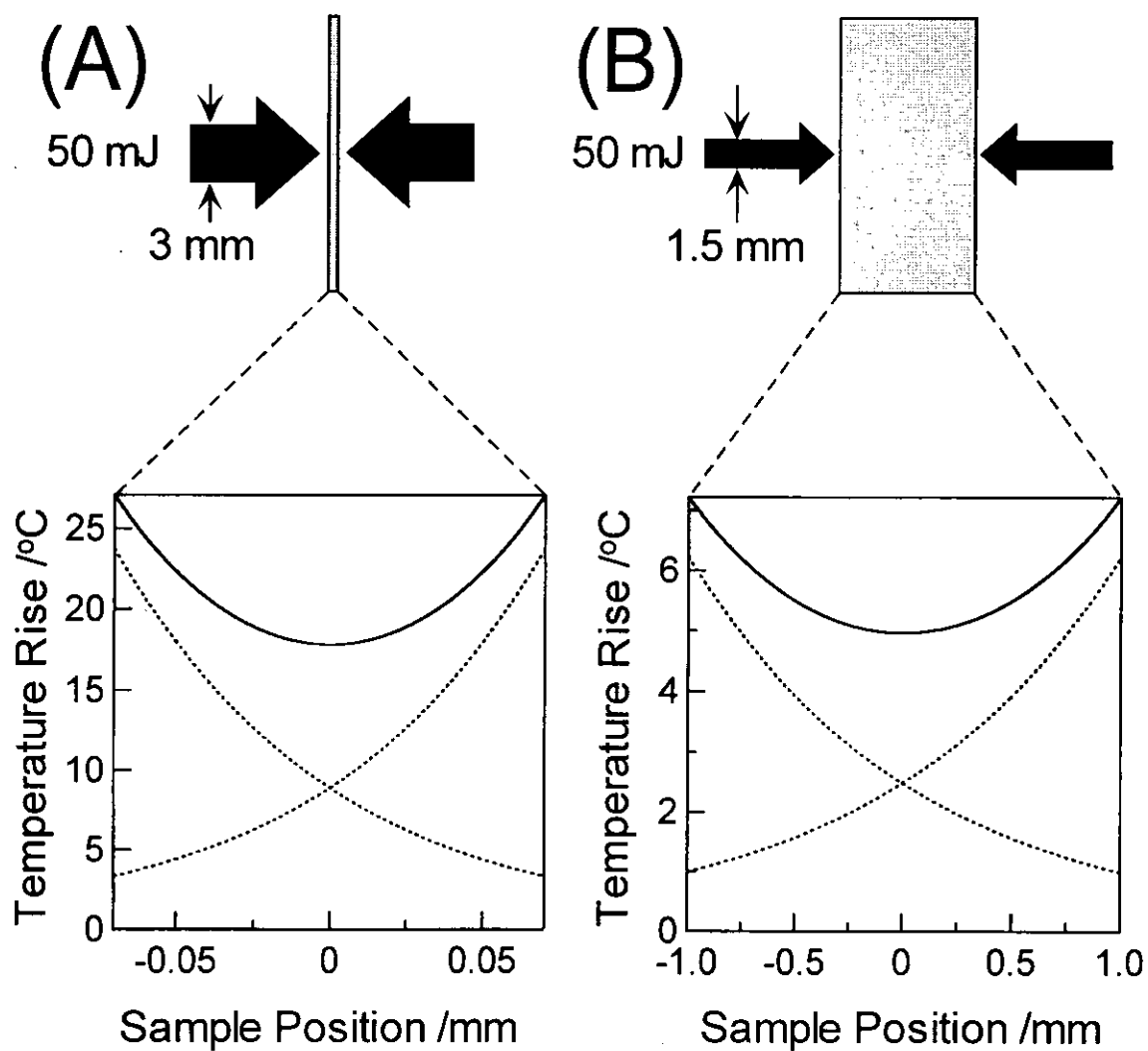


**Figure 2-1.** Estimated temperature rise of water by counter-propagating illuminations with two equivalent heat pulses of 50 mJ; (A) 1.89- $\mu\text{m}$  heat pulses with 3-mm diameter to 140- $\mu\text{m}$  thick water and (B) 1.56- $\mu\text{m}$  heat pulses with 1.5-mm diameter to 2-mm thick water. Dot lines show the profiles of temperature rise by illuminations of respective pulses and solid lines show the sum of those by counter-propagating illuminations of two heat pulses.

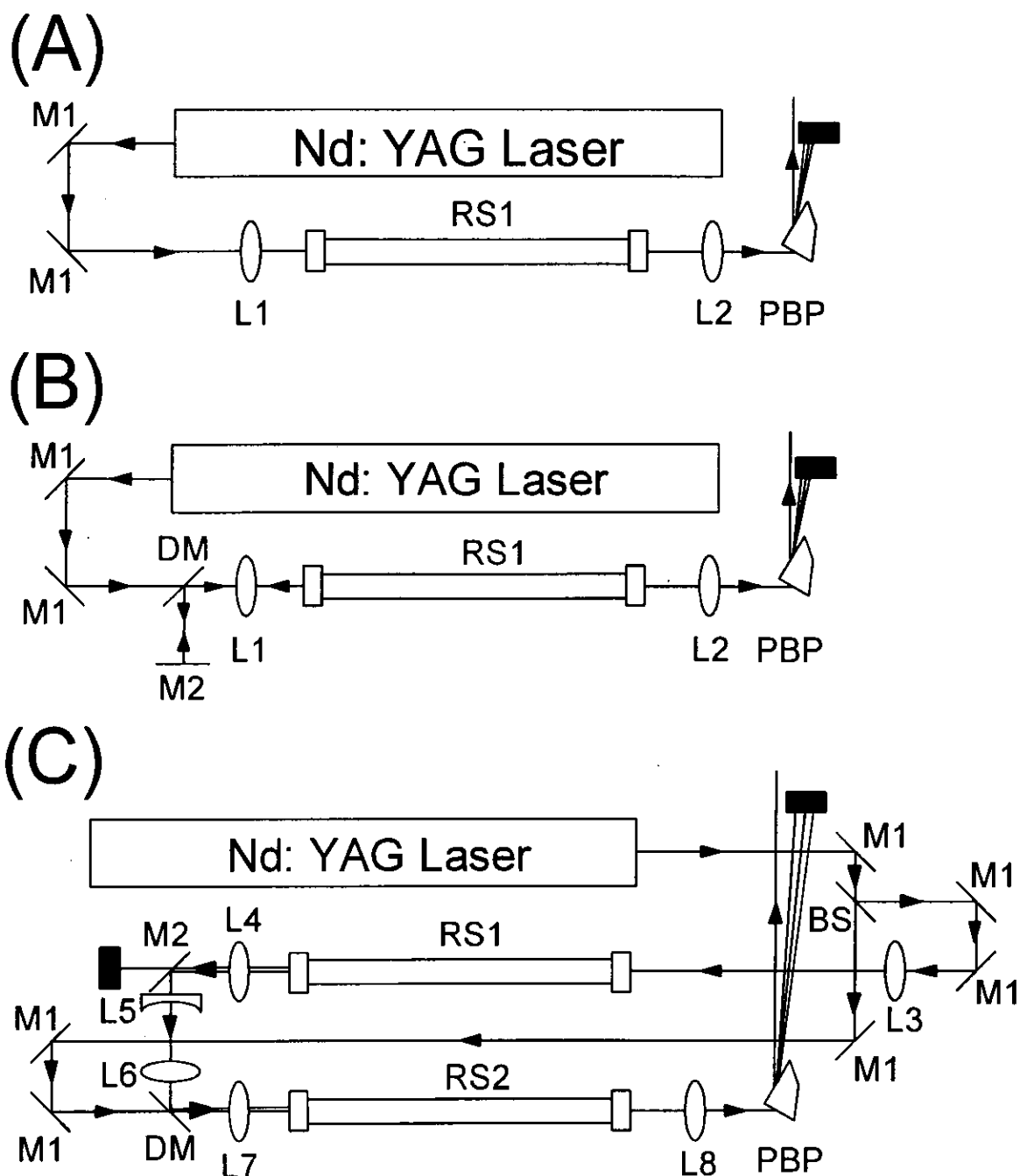


**Figure 2-2.** Schematic diagrams of the 1.89- $\mu\text{m}$  and 1.56- $\mu\text{m}$  pulse generation by the stimulated Raman effect; (A) a single pass configuration, (B) a half-resonator configuration, and (C) a seeding and amplification configuration. RS1, a compressed-gas cell with length of 1.0 m and effective diameter of 12 mm; windows, non-coated quartz with diameter of 25.9 mm and thickness of 20.0 mm. RS2, a compressed-gas cell with length of 1.1 m and effective diameter of 20 mm; windows, quartz which are AR-coated broadband filter from 1050 to 1600 nm, with diameter of 38.1 mm and thickness of 19.1 mm. M1, mirror for 1064 nm. M2, mirror for heat pulses. BS, beam-splitter for 1064 nm with variable reflection-ratio. DM, dichroic mirror with high reflectance for heat pulses and high transmittance for 1064 nm pulses. L1, L2, L3, L4, L6, L7, and L8, plano-convex lenses. L5, plano-concave lens. PBP, Pellin Broca prism.

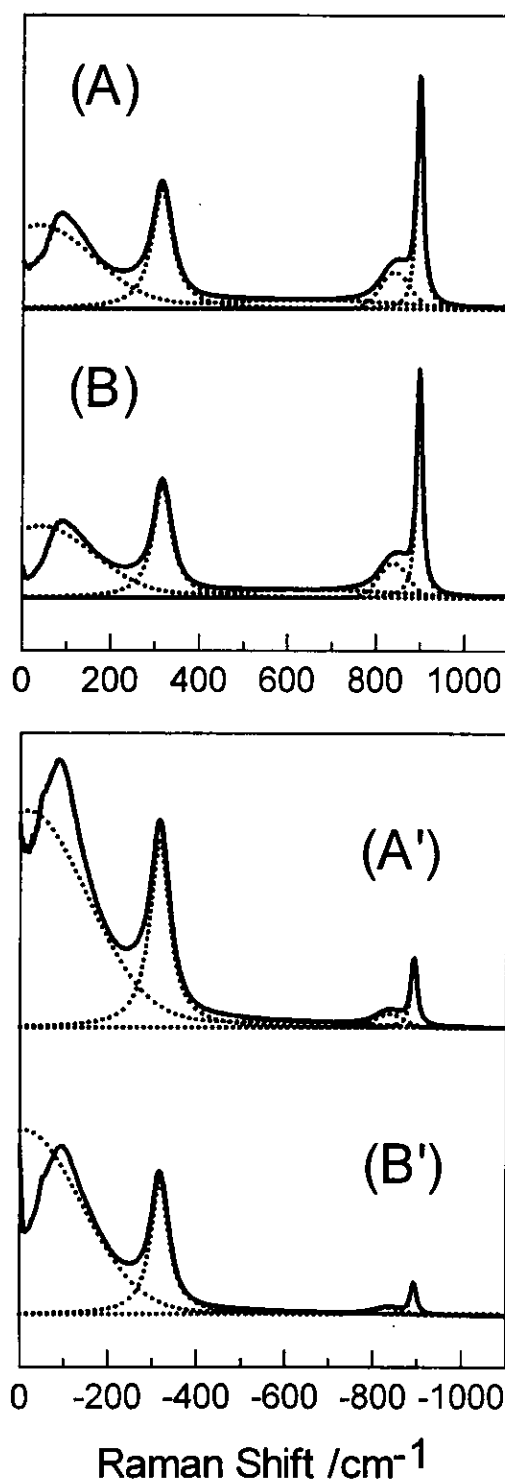


**Figure 2-3.** Stationary Stokes and anti-Stokes Raman spectra of  $\text{Na}_2\text{MoO}_4$  1.5 M aqueous solution excited at 532 nm. (A) and (A') at  $75.0 \pm 0.2^\circ\text{C}$ , (B) and (B') at  $20.0 \pm 0.1^\circ\text{C}$ . The solid lines show the observed spectra of right-angular scattering. The dashed lines show the fitted bands and base lines; Lorezian shapes at  $317\text{-cm}^{-1}$  and  $897\text{-cm}^{-1}$  bands and a Gaussian shape at  $837\text{-cm}^{-1}$  band. The intensities of these spectra are normalized to the Stokes  $897\text{-cm}^{-1}$  bands. The ordinate scale of (A') and (B') of the anti-Stokes Raman spectra is expanded with 4 times relative to that of (A) and (B) of Stokes Raman spectra. Stokes and anti-Stokes Raman spectra were obtained simultaneously.

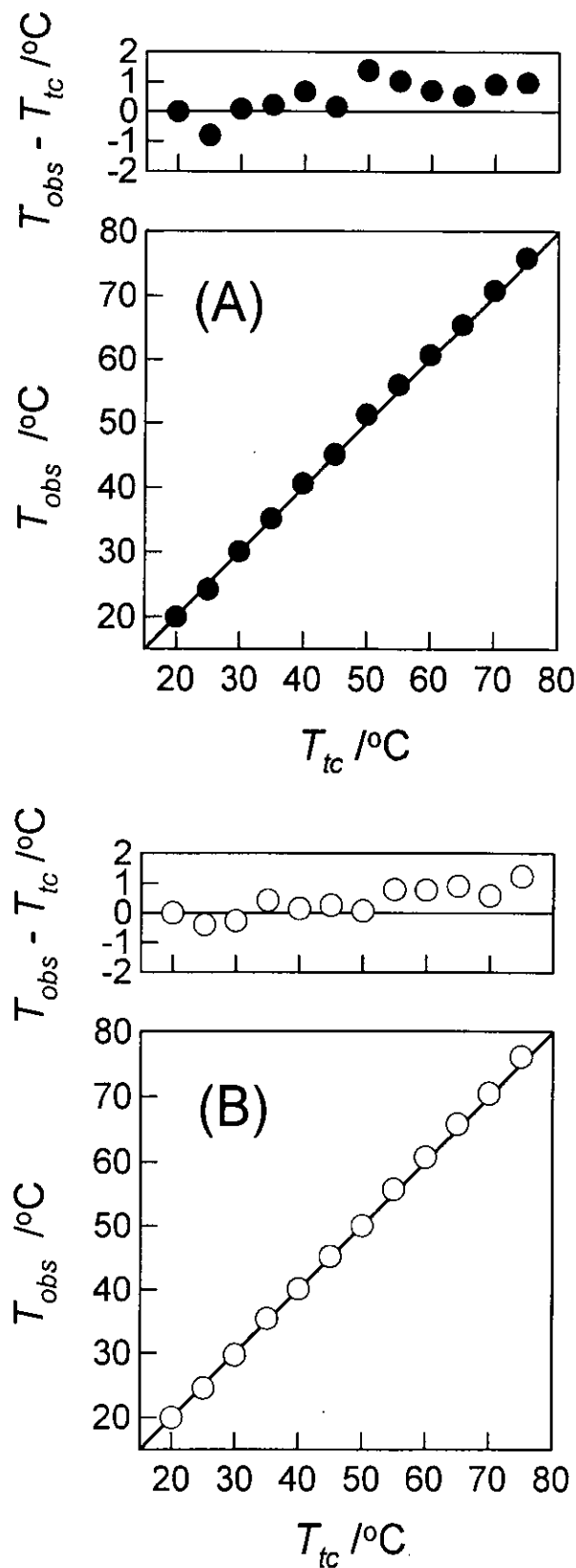


**Figure 2-4.** Steady temperature ( $T_{obs}$ ) of  $\text{Na}_2\text{MoO}_4$  solution determined from the anti-Stokes/Stokes intensity ratios of Raman bands of molybdate ions in water was compared with the temperature ( $T_{tc}$ ) measured with a calibrated alumel-chromel thermocouple; (A)  $T_{obs}$  determined from 317-cm<sup>-1</sup> bands and (B)  $T_{obs}$  determined from 897 cm<sup>-1</sup> bands. The solid lines show the straight lines ( $T_{obs} = T_{tc}$ ) for comparison. The upper panel in (A) and (B) show the plots of differences between the two obtained temperatures ( $T_{obs} - T_{tc}$ ).

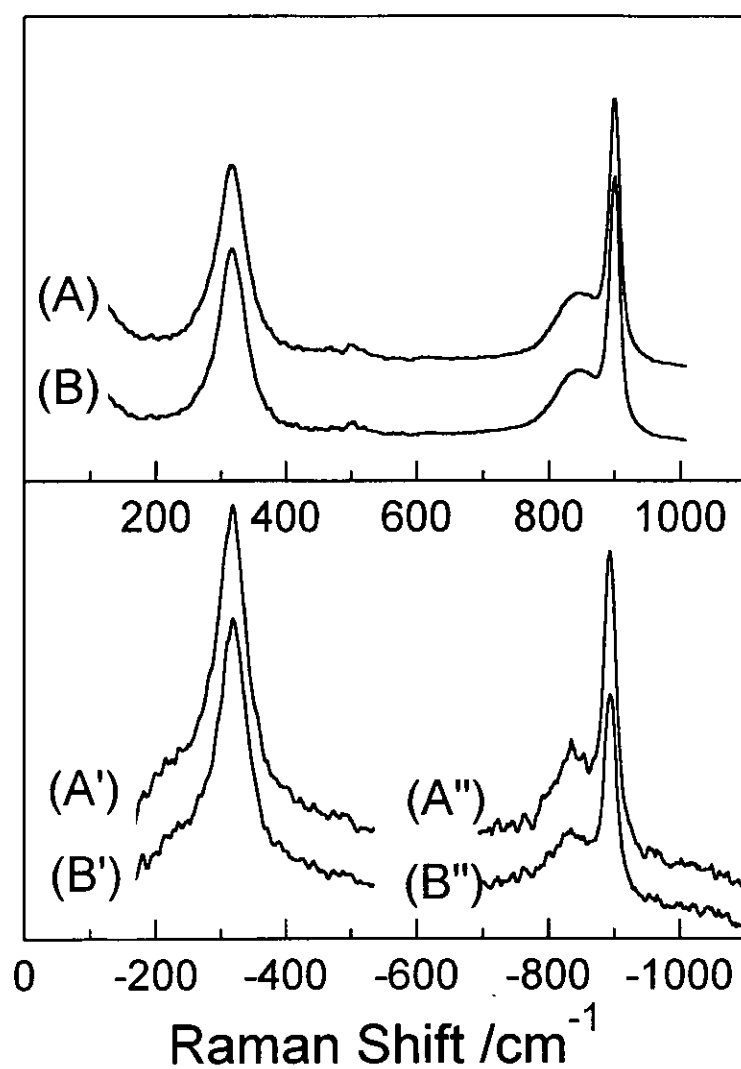


**Figure 2-5.** Time-resolved Raman spectra of  $\text{MoO}_4^{2-}$  solution (1.5 M) with 100- $\mu\text{m}$  thickness just before and just after illumination of 1.89- $\mu\text{m}$  heat pulses; (A, A' and A'') at - 20 ns and (B, B' and B'') at 20 ns. Anti-Stokes spectra (A' and B') and (A'' and B'') are vertically magnified by 4-times and 20-times, respectively, of Stokes spectra (A and B). All the spectra are obtained by subtracting Raman spectra of quartz windows from the raw TR<sup>2</sup> spectra obtained.

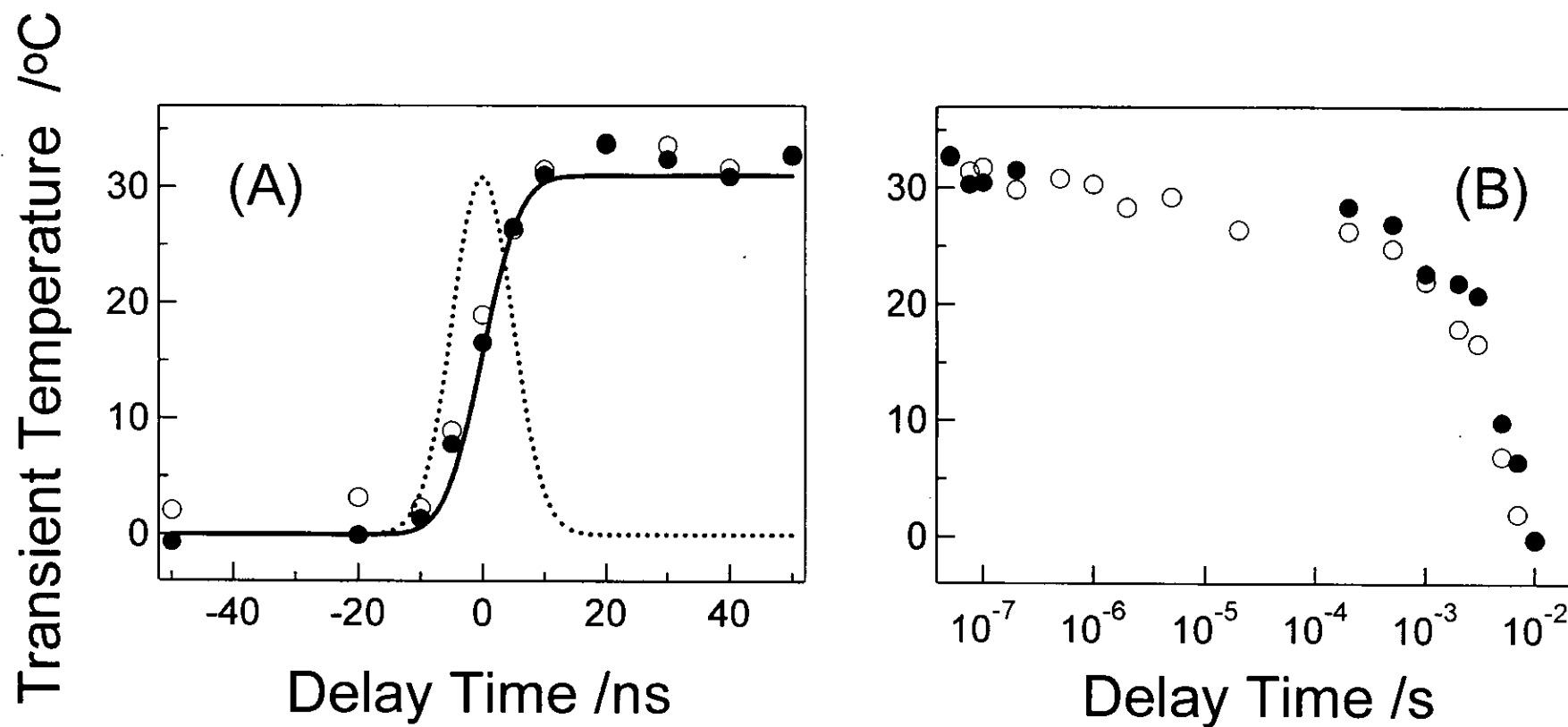


**Figure 2-6.** Observed temperature rise in nanosecond region (A) and its longer time behavior (B) of the  $\text{Na}_2\text{MoO}_4$  solution after illumination of a set of two 1.89- $\mu\text{m}$  heat pulses. Filled and open circles denote the observed transient temperatures determined with the anti-Stokes/Stokes ratios of 317- $\text{cm}^{-1}$  and 897- $\text{cm}^{-1}$  bands of molybdate ions in water, respectively. Dotted line in (A) shows the temporal cross correlation of the heat pulse and Raman probe pulse. Solid line in (A) plots the expected temperature rise which is calculated from this cross correlation.

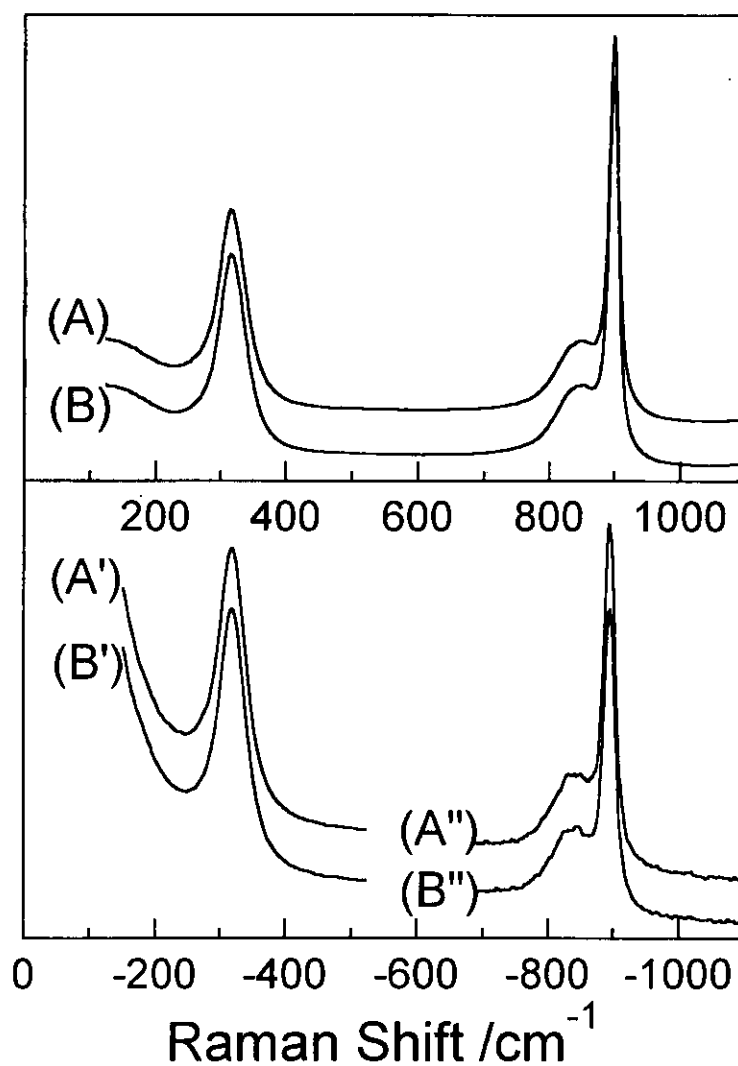


**Figure 2-7.** Time-resolved Raman spectra of  $\text{MoO}_4^{2-}$  solution (1.5 M) with 2-mm thickness just before and just after illumination of 1.56- $\mu\text{m}$  heat pulses; (A, A' and A'') at - 20 ns and (B, B' and B'') at 20 ns. Anti-Stokes spectra (A' and B') and (A'' and B'') are vertically magnified by 4-times and 20-times, respectively, of Stokes spectra (A and B). All the spectra are the raw  $\text{TR}^2$  spectra without any manipulation.

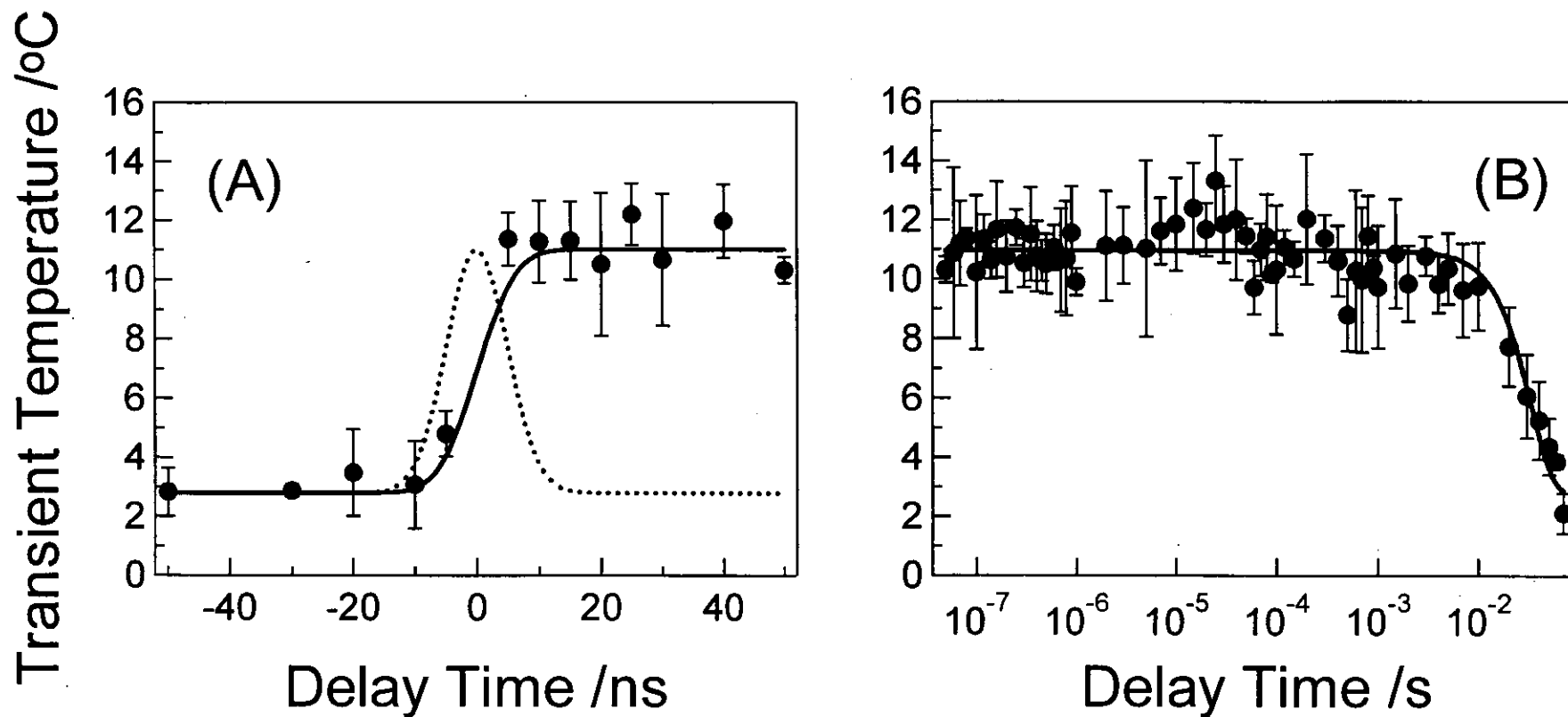


**Figure 2-8.** Observed temperature rise in nanosecond region (A) and its longer time behavior (B) of the  $\text{Na}_2\text{MoO}_4$  solution after illumination of a set of two  $1.56\text{-}\mu\text{m}$  heat pulses. Filled circles denote the averaged values over three sets of observed transient temperatures determined with the anti-Stokes/Stokes ratios of  $317\text{-cm}^{-1}$  bands of molybdate ions in water. Error bars show difference among them. Dotted line in (A) shows the temporal cross correlation of the heat pulse and Raman probe pulse. Solid line in (A) plots the expected temperature rise calculated from this cross correlation. The solid line in (B) shows the expected temperature recovery based on replacement of heated volume with fresh sample.



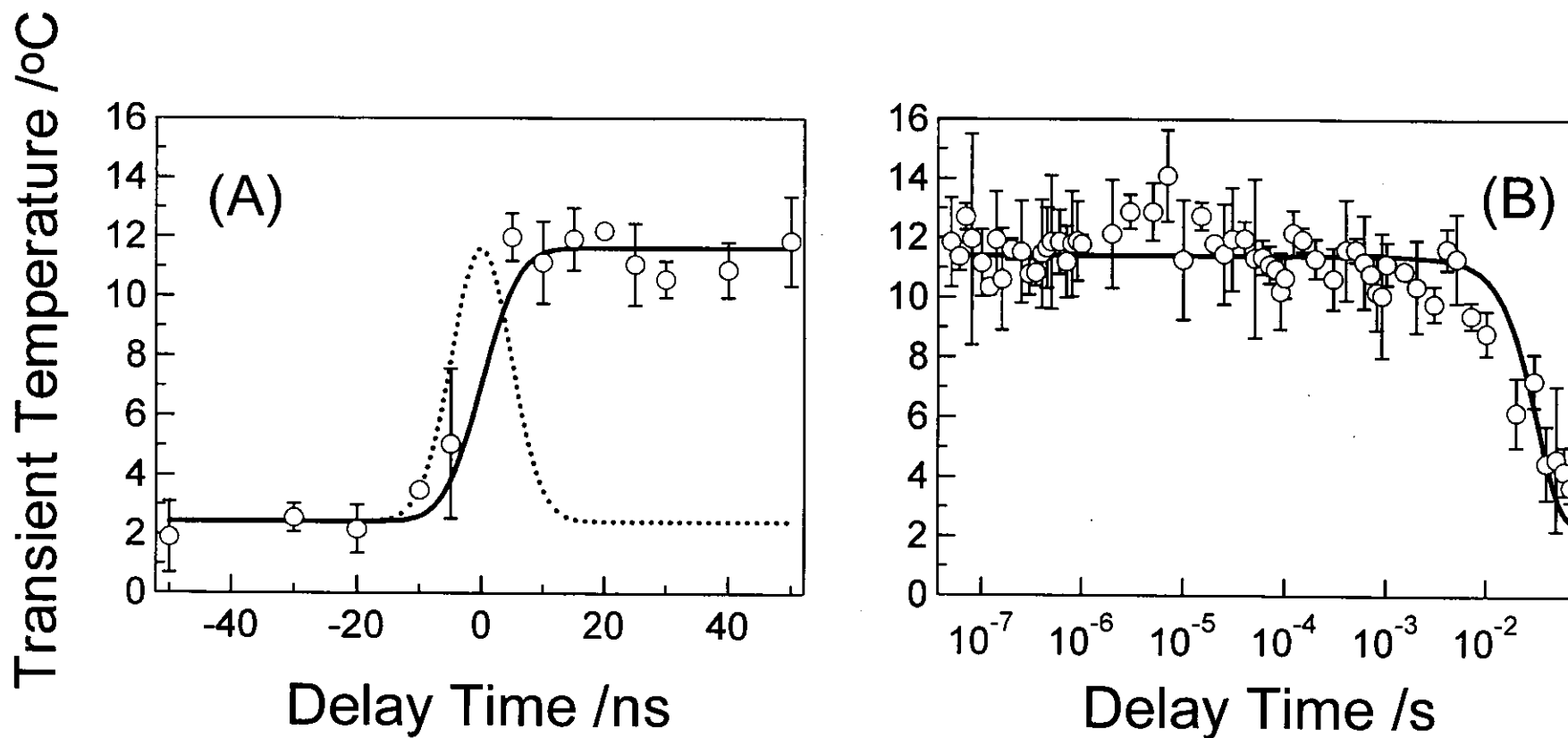


**Figure 2-9.** Observed temperature rise in nanosecond region (A) and its longer time behavior (B) of the  $\text{Na}_2\text{MoO}_4$  solution after illumination of a set of two  $1.56\text{-}\mu\text{m}$  heat pulses. Open circles denote the averaged values over three sets of observed transient temperatures determined with the anti-Stokes/Stokes ratios of  $897\text{-cm}^{-1}$  bands of molybdate ions in water. Error bars show differences among them. Dotted line in (A) shows the temporal cross correlation of the heat pulse and Raman probe pulse. Solid line in (A) plots the expected temperature rise calculated from this cross correlation. The solid line in (B) shows the expected temperature recovery based on replacement of heated volume with fresh sample.

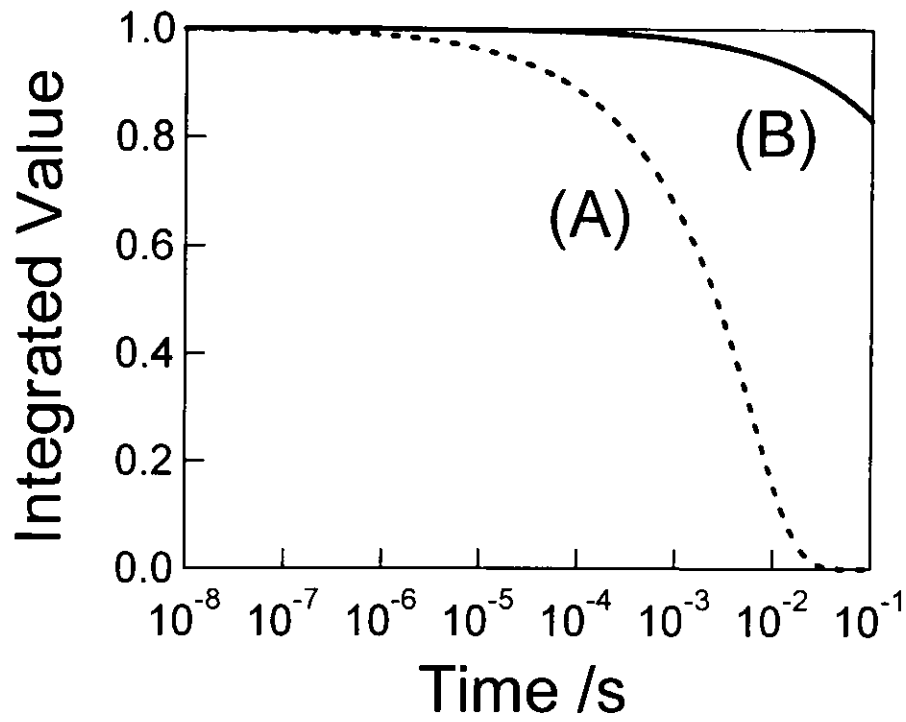


**Figure 2-10.** The temporal behavior of the integral value of thermal transfer term  $g(z,t)$  from  $-l$  to  $l$ ; (A)  $2l = 100 \mu\text{m}$  and  $a = 61 \times 2^{1/2} \times \ln 10 \text{ cm}^{-1}$  and (B)  $2l = 2 \text{ mm}$  and  $a = 4 \times \ln 10 \text{ cm}^{-1}$ .

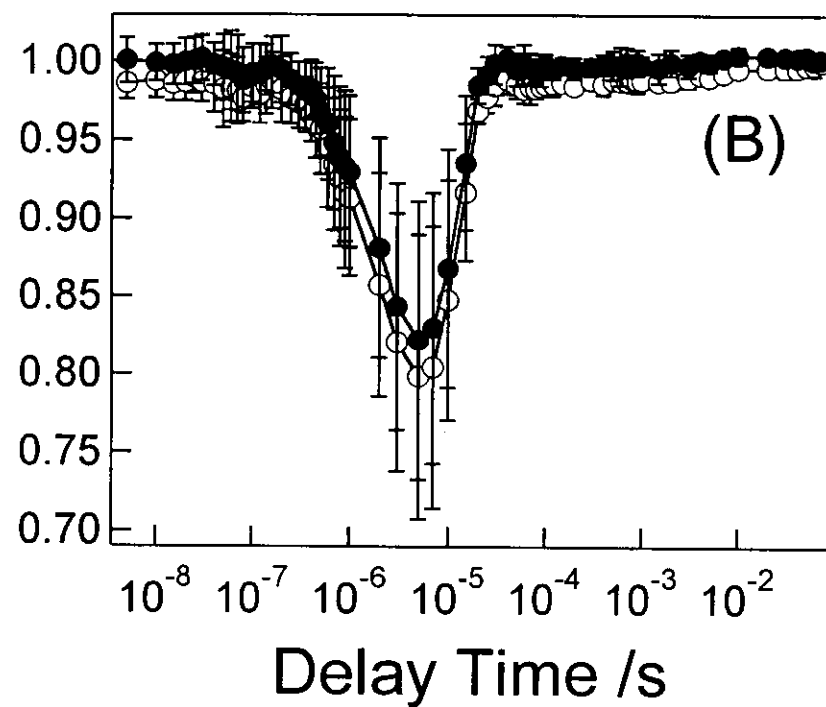
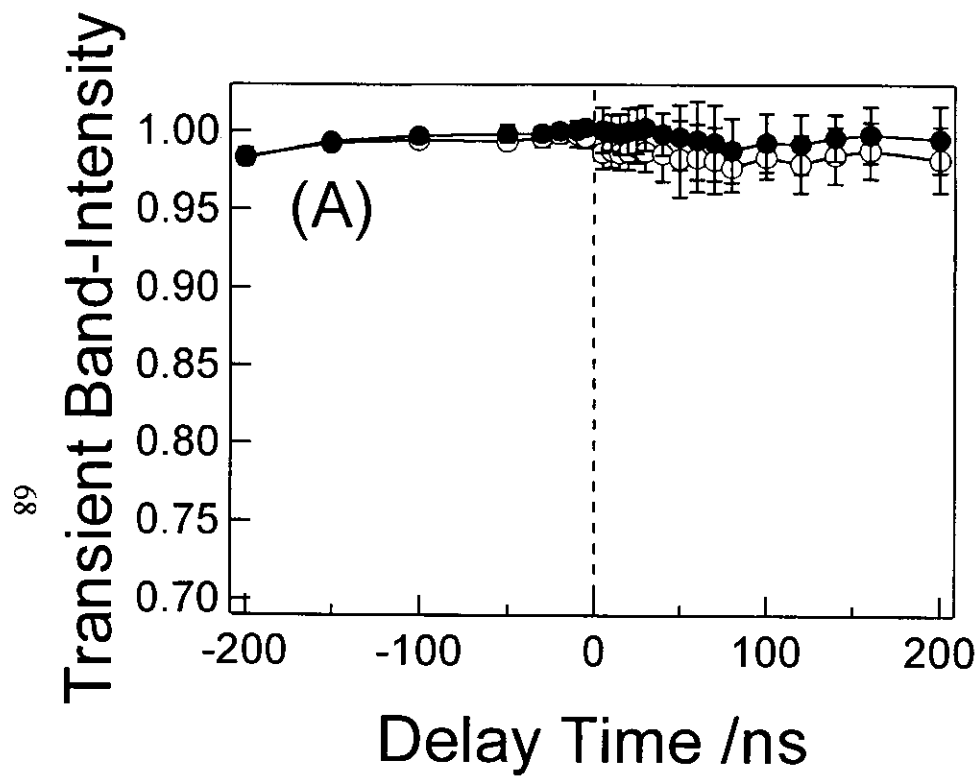


**Figure 2-11.** Observed temporal behaviors of band intensities of molybdate ions in an aqueous solution in nanosecond region (A) and their longer time behaviors (B) after the 1.56- $\mu\text{m}$  T-jump. Closed and open circles denote the averaged values over three sets of 317- $\text{cm}^{-1}$  and 897- $\text{cm}^{-1}$  band intensities, respectively. Error bars show differences among them.

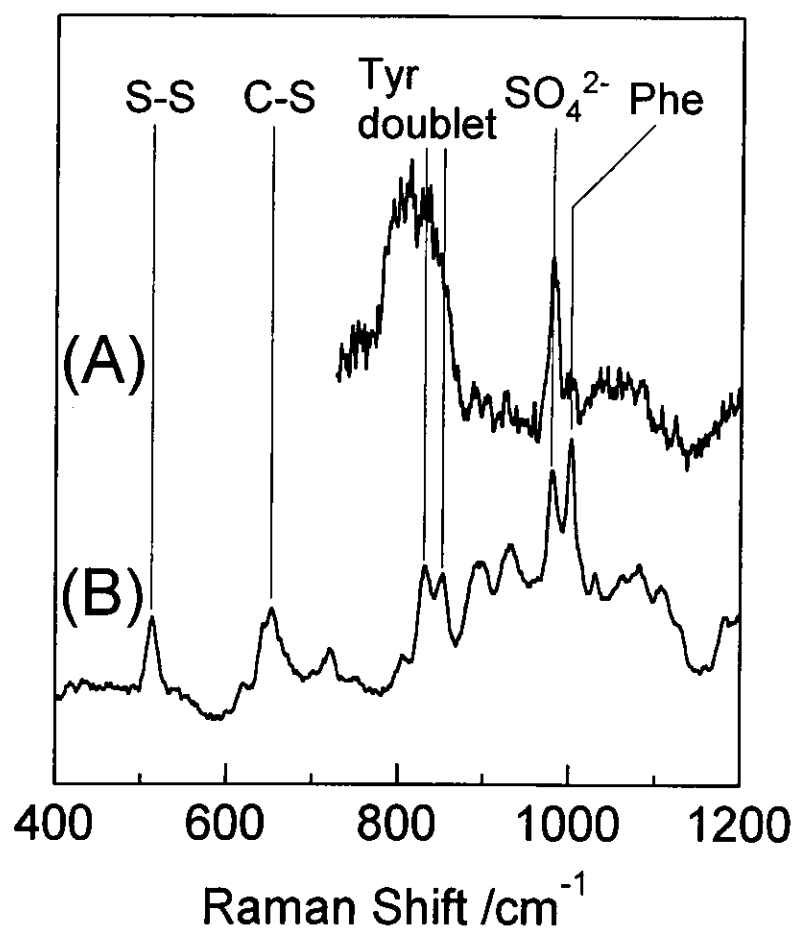


**Figure 2-12.** Stationary Raman spectra of RNase A at 25.0°C, excited by 532-nm light; (A) 150-mg/ml solution with 100- $\mu$ m thick cell and (B) 100 mg/ml solution with 2-mm thick cell. Ordinate scales of spectra (A) and (B) are arbitrary. Accumulation time for each spectrum was 30 minutes. Low frequency region of spectrum (A) is not displayed because it could not be obtained due to the disturbance of Raman scattering of quartz windows.



**Chapter 3.**  
**Time-Resolved Raman Study**  
**on Thermal Unfolding of Ribonuclease A**

*Biophys. J.* in press

Kohji Yamamoto, Yasuhisa Mizutani, and Teizo Kitagawa

## ABSTRACT

The nanosecond temperature jump (T-jump) apparatus using the 1.56- $\mu\text{m}$  heat pulse was combined with time-resolved Raman measurements to investigate thermal unfolding of a protein for the first time. This study pursued the transient structures of bovine pancreatic ribonuclease A (RNase A) in the thermal unfolding transition with time-resolved Raman spectra excited at 532 nm. It revealed that the temporal structural changes of RNase A differ among its regions in the initial 5 ms of unfolding; (1) the C-S stretching band of methionine residues exhibited 10% change of that expected from the stationary state temperature-difference spectra in the initial 200 ns following T-jump and another 10% in 5 ms, (2) the Raman intensity of  $\text{SO}_4^{2-}$  ions around 980  $\text{cm}^{-1}$  increased at 100  $\mu\text{s}$ , presumably due to some conformational changes of the protein around the active site, (3) the S-S stretching and tyrosine doublet displayed little changes within 5 ms. These results led to the conclusion that the conformational changes in the initial step of unfolding are not always concerted.

### 3.1 INTRODUCTION

Elucidation of protein folding mechanism is becoming a current topic of fast time-resolved spectroscopy since Anfinsen<sup>1</sup> found that the nature of interactions responsible for protein folding is determined solely by amino acid sequence of the protein. To investigate fast events of protein dynamics within milliseconds, the temperature jump (T-jump) is recently revisited as a rapid initiation method owing to developments in modern laser techniques<sup>2-10</sup> (Chapter 1). In these studies, fluorescence<sup>3-6</sup> (tryptophan or covalently-bound chromophore), infrared absorption<sup>2,7-9</sup> (amide I bands), and ultraviolet resonance Raman scattering<sup>10</sup> (amide I, II, and III) have been used as rapid probes. On the other hand, nonresonant Raman spectroscopy can provide detailed information on conformations or environments of various side chains in addition to the secondary and tertiary structures of protein backbone.<sup>11</sup> Hence we utilized this method as a rapid probe and succeeded in observing time-resolved nonresonant Raman spectra of a protein upon nanosecond T-jump for the first time.<sup>12</sup>

It is known that disulfide bonds play a critical role in the folding of many proteins as well as in the stabilization of native tertiary structures.<sup>13</sup> Bovine pancreatic ribonuclease A (RNase A) has been studied extensively to unravel its folding/unfolding pathways.<sup>14-17</sup> RNase A is a 124-residue protein containing four native disulfide bonds (Cys-26–Cys-84, Cys-40–Cys-95, Cys-58–Cys-110, and Cys-65–Cys-72) as illustrated in Figure 3-1.<sup>18</sup> Folding pathway of RNase A might not be unique and the rate-determining steps in the major and minor populated pathways involve the formation of the three-disulfide species which lacks the 40-95 or 65-72 bond.<sup>17</sup> While the oxidative regeneration and reductive cleavage of the disulfide bond were suggested to be kinetically same<sup>17</sup>, the three-disulfide species lacking the 65-72 bond is thought to be



the most highly populated intermediate in the unfolding pathways.<sup>19</sup> The role of the 65-72 bond was examined using des-[65-72]-RNase A, i.e. RNase A which lacks Cys-65–Cys-72 disulfide bond,<sup>20</sup> and it was found that the midpoint of the thermal transition of des-[65-72]-RNase A was 17.8°C lower than that of native RNase A but that these two proteins have a close structural similarity in all regions with only major differences in the loop region comprising residues 60-72. The recent <sup>1</sup>H, <sup>15</sup>N, and <sup>13</sup>C NMR studies revealed that the (C40A, C95A) mutant as well as wild-type proteins fold in a similar way.<sup>21</sup> Thus, it is thought that the rate-determining step corresponds to a partial unfolding even in one region of the protein and not to a global conformational unfolding process. On the other hand, relationships of the S-S stretching ( $\nu_{ss}$ )<sup>22-24</sup> and C-S stretching ( $\nu_{cs}$ ) frequencies<sup>25-27</sup> with the dihedral angles of the C-C-S-S-C-C moiety have been investigated. Accordingly, we focused our attention on the side-chain conformational changes of RNase A upon T-jump by a nanosecond laser pulse.

In this study we utilized the 1.56- $\mu$ m heating for the initiation of thermal unfolding of RNase A to get well-defined transient Raman signals of it with 2-mm thick sample cell (Chapter 2).

## **3.2 EXPERIMENTAL PROCEDURES**

### **3.2.1 SAMPLE PREPARATION**

RNase A (Sigma, type IIIA) was purified by passage through two columns; first, ion exchange chromatography with sulphopropyl sepharose (Amersham Pharmacia Biotech, SP Sepharose FF) equilibrated with 25 mM HEPES, 1 mM EDTA, pH 8.0 combined with linear gradient elution with 0 - 150 mM NaCl,<sup>28</sup> and second, adsorption on an active carbon column activated with 1 M HCl. The passage through the second

column removed the yellow color completely. Finally, the solvent was exchanged with 200 mM acetate buffer, pH 5.0 containing 40 mM Na<sub>2</sub>SO<sub>4</sub>, and the concentration of RNase A was adjusted to 7.0 mM on the basis of  $\epsilon_M = 9.8 \times 10^3 \text{ M}^{-1}\text{cm}^{-1}$  at 278 nm.<sup>29</sup> The sample solution was degassed before putting it into the Raman cell to avoid generation of bubbles upon T-jump. This treatment practically reduced not only the stray light and thus background of Raman spectra but also laser-induced damages of quartz window of the Raman cell.

### 3.2.2 MEASUREMENTS OF STEADY-STATE AND TIME-RESOLVED RAMAN SPECTRA OF RNASE A

The experimental arrangements in the time-resolved Raman (TR<sup>2</sup>) measurements of RNase A following illumination of 1.56- $\mu\text{m}$  heat pulses were the same as those of MoO<sub>4</sub><sup>2-</sup> solution (Chapter 2), except for the reference temperature  $T_0$ . The 1.56- $\mu\text{m}$  beam (135 mJ) with the 9-ns pulse width was split into two equal portions and the protein solution in the 2-mm thick cell with quartz windows was illuminated from both sides by the two counter-propagated heat pulses. Hence T-jump of 9°C was expected to be accompanied with 3°C rise in the negative delay time region (Figure 2-8(A) and 2-9(A)). Raman excitation by the second harmonic (532 nm) of another Q-switched Nd:YAG laser with 7-ns pulse width followed the illumination of heat pulses with delay times ( $\Delta t$ ) of -100 ns, 200 ns, 100  $\mu\text{s}$ , and 5 ms. The elevated temperature was maintained at  $\Delta t = 5 \text{ ms}$  (Figure 2-8(B) and 2-9(B)). Reference temperature  $T_0$  was kept at 59.0°C (fluctuation < 0.2°C) for the TR<sup>2</sup> measurements of RNase A solutions. Time-resolved Raman spectra presented are an average over 20 cycles. Steady-state Raman spectra at given temperatures were obtained by changing  $T_0$  without illumination of heating pulses in the same arrangements.

### 3.3 RESULT

Figure 3-2 displays the steady-state Raman spectra of RNase A and buffer solution observed at 20.0°C (*a*, *b*, and *e*) and 71.0°C (*c*, *d*, and *f*). The temperature-induced changes in the Raman spectra of RNase A [ $g = 2 \times ((f) - (e))$ , difference spectrum] are also shown at the bottom of Figure 3-2. Spectra (*a*) and (*c*) are the raw Raman spectra of RNase A containing the contribution from the buffer solution (200 mM acetate buffer with 40 mM Na<sub>2</sub>SO<sub>4</sub>) and spectra (*b*) and (*d*) show those of the buffer solution only. Spectra (*e*) and (*f*) were obtained by subtraction of buffer-only spectra [(*b*) and (*d*)] from the raw RNase A spectra [(*a*) and (*c*)] at each temperature. Hence the difference spectrum (*g*) of RNase A does not include the spectral changes of buffer solution. The vibrational assignments of well-established Raman bands<sup>11</sup> are designated in Figure 3-2. Upon the temperature change from 20.0 to 71.0°C, the  $\nu_{ss}$  band around 510 cm<sup>-1</sup> exhibits frequency shift toward lower frequencies and broadening (from 14 to 26 cm<sup>-1</sup> in terms of half-height width), while the  $\nu_{cs}$  band around 655 cm<sup>-1</sup> shows intensity reduction. The SO<sub>4</sub><sup>2-</sup> band around 980 cm<sup>-1</sup> shows intensity increase. The intensity ratio of tyrosine doublet at 831/851 cm<sup>-1</sup> changes from 1.4 to 0.8, indicating the change of hydrogen bonding of tyrosine residues.<sup>30</sup> These changes qualitatively agree with the reported results<sup>31</sup>.

Figure 3-3 shows the time-resolved Raman spectra of RNase A upon T-jump from 62 to 71°C. Spectra (*a*) to (*d*) were observed for  $\Delta t$  of -100 ns, 200 ns, 100  $\mu$ s, and 5 ms, respectively, while spectrum (*e*) represents the probe-only spectrum observed in the cycle of T-jump experiments. For comparison, the steady-state spectra at 59.0 and 71.0°C are also included as spectra (*f*) and (*g*), respectively. In all of them the buffer-only spectrum measured under the same condition had been subtracted. Apparently, all

the spectra appear similar except for spectrum (g), but their changes can be revealed by difference calculations.

Figure 3-4 displays the difference spectra, which were calculated from the raw spectra. Therefore the contributions from buffer solution were included in the spectra of Figure 3-4. The time-resolved Raman spectra are represented as the difference from the probe-only spectrum measured at  $T_0$  (59°C). Accordingly, spectra (a) to (d) correspond to  $\Delta t = -100$  ns, 200 ns, 100  $\mu$ s, and 5 ms, respectively. Spectra (e) and (f) delineate the stationary temperature-difference spectra of 62.0°C–59.0°C and 71.0°C–59.0°C, respectively. The stationary state temperature-difference between the buffer-only spectra at 71.0°C and 59.0°C is also represented by spectrum (g) for reference. This is the maximum contribution from the temperature dependence of the buffer spectrum. Spectral changes of buffer solution are small except for the bands of acetate ( $\sim 925$   $\text{cm}^{-1}$ ) and sulfate ( $\sim 980$   $\text{cm}^{-1}$ ) ions, which exhibited appreciable temperature dependence.

Spectrum (a) at -100 ns is almost the same as spectrum (e). This is compatible to the fact that the reference temperature in the repeated T-jump experiment is 3°C higher than  $T_0$ . Spectrum (b) exhibits differential peaks at 925  $\text{cm}^{-1}$  and 980  $\text{cm}^{-1}$  which are attributed to acetate ions and sulfate ions, respectively. These amounts of spectral differences are close to the sum of spectral changes of buffer solution (71.0°C–62.0°C) and those of RNase A raw spectrum for  $\Delta t = -100$  ns (a), indicating that the temperature is definitely raised at  $\Delta t = 200$  ns (b). In addition to the buffer peaks, spectrum (b) contains the contribution from the C-S stretching around 655  $\text{cm}^{-1}$ . Spectrum (c) is slightly noisier than spectra (b) and (d) owing to the appearance of effects of shock wave generated by the heat pulse, which practically increases Rayleigh scattering. Despite the efforts to remove the increased stray light through optical alignments and

filtering, it remained. Therefore, this contribution has been removed by subtraction of water spectrum measured under similar conditions. Anyway, this does not affect the difference intensity of any particular peak except for increased noises. Spectrum (c) exhibits an increase of differential patterns for the  $\text{SO}_4^{2-}$  band besides the intensity reduction for the  $\nu_{\text{CS}}$  band. Spectrum (d) is nearly the same as spectrum (c) but is distinct from spectrum (f), suggesting that the conformational change does not proceed largely between 100  $\mu\text{s}$  and 5 ms.

For detailed analysis of the transient spectra of RNase A, a part of the difference spectra are delineated in expanded scales in Figure 3-5, where panel (A) and (B) denote the C-S and  $\text{SO}_4^{2-}$  stretching regions, respectively. For comparison, transient and stationary difference spectra of the buffer solution only are shown in panel (C), where the ordinate and abscissa scales are the same as those of panel (B). The delay times or stationary-state temperature in panel (C) are identical with those designated in panel (B). In the spectra shown in panel (B), the contributions from the temperature dependence of buffer-only spectrum (panel (C)) had been subtracted. The base lines used for quantitative evaluation of spectral changes are drawn by broken lines. The temporal changes in difference spectra are clearer in Figure 3-5 than in Figure 3-4. The intensity increase of the  $\text{SO}_4^{2-}$  band in panel (B) is seen in the spectrum for  $\Delta t = 100 \mu\text{s}$  (c) and grows until  $\Delta t = 5 \text{ ms}$  (d), whereas that in panel (C) occurs in the spectrum for  $\Delta t = 200 \text{ ns}$  (b) and are practically unchanged until 5 ms (d). Therefore the transient intensity increase in panel (B) is distinct from that of buffer solution.

The temporal spectral changes were calculated as area intensities of the difference peaks. The results are illustrated in Figure 3-6, where the intensity reduction of the  $\nu_{\text{CS}}$  band in the stationary state spectra are also plotted against temperature in

panel (A). The intensity changes in the transient spectra are the quantities relative to the amount of the change between the stationary-state spectra at 59.0°C and 71.0°C, which were obtained from Figure 3-5(A), although the positions along the abscissa are arbitrary. Here the probe-only spectrum at  $T_0$  (59.0°C) was used as the reference spectrum. The spectrum of  $\Delta t = -100$  ns exhibits 20% reduction of intensity and it corresponds to that of the stationary-state spectrum at 62.0°C, in good agreement with the calibration using  $\text{MoO}_4^{2-}$  ions. For  $\Delta t = 200$  ns, the intensity decreased further by 10% but the amount of intensity decrease was 40% of the stationary-state difference even at 5 ms. On the other hand, the intensity increase of the  $\text{SO}_4^{2-}$  bands for  $\Delta t = -100$  ns is small and it is consistent with the difference in the stationary-state spectrum between 59.0°C and 62.0°C as shown in spectrum (e) of Figure 3-5(B). Its intensity increase starts from  $\Delta t = 100$   $\mu\text{s}$  as illustrated in Figure 3-6(B), where the intensity changes normalized to the positive part of spectrum (f) in Figure 3-5(B) are designated.

### 3.4 DISCUSSION

#### 3.4.1 TEMPERATURE JUMP IN RNASE A SOLUTION

The amount of temperature rise by laser induced T-jump can be determined from the energy of the heat pulse and the heated volume of the sample as demonstrated for the  $\text{MoO}_4^{2-}$  solution (Figure 2-8(A) and 2-9(A)). Nevertheless, it is a critical problem whether the laser induced T-jump with the 1.56- $\mu\text{m}$  pulse brings about as high and as rapid temperature rise in the protein solution as in the nonprotein solution. In nonresonant Raman scattering measurements, however, spectra of both RNase A and temperature reference material cannot be obtained simultaneously, because the former is much weaker in Raman intensity than the latter. Hence, the temporal temperature

behavior was examined for the mixed solution of 7 mM RNase A with 0.42 M  $\text{Na}_2\text{MoO}_4$  (pH 5.0) at 59.0°C by the initiation of laser-induced T-jump, where the beam size of the heat pulses was the same as that used in the T-jump experiments of the  $\text{MoO}_4^{2-}$  solutions and the RNase A solutions. From the 317 and 897  $\text{cm}^{-1}$  bands of  $\text{MoO}_4^{2-}$  in the transient spectra of this solution, which almost consisted of  $\text{MoO}_4^{2-}$  bands (not shown), the temperature rise was determined. The observed transient temperatures are plotted against the delay time in Figure 3-7, where the abscissa scale is linear in a short time region (*A*) but logarithmic in a longer time region (*B*). It was thus confirmed that the temperature rise of  $9 \pm 1^\circ\text{C}$ , at least, was accomplished within 20 ns and that the temperature in negative delay region was  $2.5 \pm 1^\circ\text{C}$  higher than the reference temperature (59.0°C). This result agrees with the transient temperature behavior of the  $\text{MoO}_4^{2-}$  solution (1.5 M) without protein, shown in Figure 2-8(*A*) and 2-9(*A*).

However, we cannot rule out a possibility that the protein stability increases due to  $\text{MoO}_4^{2-}$  ions added and that as a result the melting did not occur in this temperature range. This would mean that in the absence of the heat energies absorbed by thermal unfolding the temperature rises are identical between the  $\text{MoO}_4^{2-}$  solutions with and without the protein. From the enthalpy changes of 757  $\text{kJ mol}^{-1}$  involved in the thermal unfolding of RNase A at pH 5.0<sup>32,33</sup>, the absorbed heat owing to the thermal unfolding of 7 mM RNase A solution in the laser-heated volume can be estimated to be 16 mJ for the present T-jump experiments (Figure 3-3, 3-4 and, 3-5). The estimated energy is 12% of the total heat-pulse energy (135 mJ) and would be entirely absorbed when thermal unfolding of RNase A is completed. Even in this case, 88% of the heat pulse energy can be used to raise temperature similar to the case of a simple  $\text{MoO}_4^{2-}$  solution. In fact the conformational changes of RNase A were small within the initial 5

ms after the T-jump and hence the actual heat energy absorbed would be much less than that thus estimated. Therefore, the temperature rise in the RNase A solution by laser induced T-jump is considered to be close to that observed for the molybdate solution ( $\Delta T = 9^\circ\text{C}$ ).

### 3.4.2 DISULFIDE CONFORMATIONS

Sugeta et al.<sup>22-24</sup> studied the relationship between the S-S stretching frequency and conformation, and interpreted it in terms of dihedral angles around the three successive bonds of C-C-S-S-C-C; 508-512  $\text{cm}^{-1}$  for GGG, 523-528  $\text{cm}^{-1}$  for TGG, and 540-545  $\text{cm}^{-1}$  for TGT (T: *trans*, G: *gauche*). They also determined with diethyldisulfide that the GGG conformation is more stable by 2.5  $\text{kJ mol}^{-1}$  than TGG. The TGT form has not been identified. The  $\nu_{\text{ss}}$  modes of RNase A have been observed at 514  $\text{cm}^{-1}$  at room temperature and no peaks at 520-545  $\text{cm}^{-1}$ , indicating that the four disulfide bonds adopt the GGG conformation. This conformational assignment of disulfide bridges agrees with the X-ray crystallographic structure illustrated in Figure 3-1, where all the four disulfide bridges form the GGG conformation.

The  $\nu_{\text{ss}}$  bands in Figure 3-3 were fitted by a single Gaussian function under the assumption of inclined straight base line. Their peak frequencies and bandwidths, which were determined for both transient and steady-state spectra, are plotted against temperature in Figure 3-8. The peak frequencies differ between the probe-only spectrum and that for  $\Delta t = -100$  ns, but they are in reasonable agreement with the steady state spectra measured at 59.0 and 62.0°C, respectively. The  $\nu_{\text{ss}}$  frequency in the transient state spectra did not change in 5 ms. The half-width becomes larger at higher temperatures in the steady state spectra and its behavior is close to that of peak frequencies. However, in the transient spectra, the half-width also remained unchanged



until 5 ms. These results mean that a conformational change around the four disulfide bridges of cysteine residues does not take place in the initial 5 ms of thermal unfolding. This conclusion is compatible to the notes<sup>20,21</sup> that disulfide bridges play a critical role in the stabilization of RNase A.

Upon the temperature rise from 59 to 71°C, the  $\nu_{ss}$  frequency in the steady spectra decreased from 513 to 509  $\text{cm}^{-1}$ . This implies that the conformations of four disulfide bridges change within the category of the GGG conformation. It is plausible that the disulfide moiety in native RNase A has some strain at room temperature but that the strain disappears upon relaxation of the tertiary structure at higher temperatures. It would mean that the  $\text{C}_\alpha\text{-C}_\beta\text{H}_2\text{-S}_\gamma\text{-S}_\gamma'\text{-C}_\beta'\text{H}_2\text{-C}_\alpha'$  moiety approaches more to the true GGG conformation upon unfolding of RNase A. However, band broadening, which is observed in the panel (B) of Figure 3-8, indicates the presence of various conformations at higher temperatures.

Cysteine residues also give rise to the C-S stretching bands around 630-750  $\text{cm}^{-1}$ . The correlation between the C-S stretching frequency and the conformation of  $\text{X-C-CH}_2\text{-S-}$  has been studied with dialkyl-disulfide molecules as model compounds of the disulfide bridge.<sup>22-24</sup> The  $\nu_{cs}$  frequency is sensitive to an atom (X) at the *trans* position of S atom; 630-670  $\text{cm}^{-1}$  for  $\text{X=H}$  ( $\text{P}_\text{H}$ ) and 700-745  $\text{cm}^{-1}$  for  $\text{X=C}$  ( $\text{P}_\text{C}$ ), where  $\text{P}_\text{X}$  denotes that the atom X is present at the *trans* position of the S atom. From the X-ray crystallographic structure of RNase A,<sup>18</sup> all the eight cysteine residues adopt the  $\text{P}_\text{C}$  conformation regarding the  $\text{X-C}_\alpha\text{-C}_\beta\text{H}_2\text{-S-}$  group. Therefore it is considered that the C-S stretch of cysteine residues hardly contributes to the intensity reduction at 655  $\text{cm}^{-1}$  in the transient and stationary spectra of RNase A in Figure 3-6(A).

### 3.4.3 CONFORMATIONS OF METHIONINE

The fact that the  $\nu_{CS}$  modes of the eight cysteine residues do not give rise to the 655-cm<sup>-1</sup> band leads us to presume that the intensity reduction of  $\nu_{CS}$  bands around 655 cm<sup>-1</sup> is due to the C-S stretching of methionine residues. Actually RNase A has four methionine residues; (Met-13, -29, -30, and -79). It has been demonstrated from studies of model monosulfide compounds having the X-C-CH<sub>2</sub>-S-CH<sub>3</sub> structure that the  $\nu_{CS}$  frequency of CH<sub>2</sub>-S group is sensitive to an atom (X) at the *trans* position of the S atom; 640-680 cm<sup>-1</sup> for X = H (P<sub>H</sub>), and 740-760 cm<sup>-1</sup> for X = C (P<sub>C</sub>).<sup>25-27</sup> Methylpropylsulfide, which is the closest model compound in their studies to the side chain of a methionine residue, gives rise to Raman bands at 645 and 667 cm<sup>-1</sup> for the P<sub>H</sub>-G and P<sub>H</sub>-T conformations, respectively. On the other hand, the  $\nu_{CS}$  frequency of the S-CH<sub>3</sub> group is fairly independent of its conformation (700-725 cm<sup>-1</sup>). Consequently, it is presumed that the side chain conformations of some methionine residues change in the initial stage of unfolding. From the X-ray crystallographic structure,<sup>18</sup> the side chains (X-C <sub>$\beta$</sub> H<sub>2</sub>-C <sub>$\gamma$</sub> H<sub>2</sub>-S <sub>$\delta$</sub> -C <sub>$\epsilon$</sub> H<sub>3</sub>) of Met-13, -29, and -30 adopt the P<sub>H</sub>-G conformation and that of Met-79 adopts the P<sub>C</sub>-T conformation. Hence Met-13, -29, and -30 are considered as the candidates which underwent some conformational changes of side chains in the initial stage of unfolding. Since the -C <sub>$\gamma$</sub> H<sub>2</sub>-S <sub>$\delta$</sub> -C <sub>$\epsilon$</sub> H<sub>3</sub> side chain has no particular interactions with other residues, it is reasonable that some changes of packing around this group in the relaxation of the tertiary structure starts at 200 ns following T-jump.

### 3.4.4 CONFORMATIONAL CHANGE OF TYROSINE SIDE CHAIN

RNase A has six tyrosine residues (Tyr-25, -73, -76, -92, -97, and -115). The tyrosine doublet at 831 and 851 cm<sup>-1</sup> arises from the Fermi resonance between the ring-

breathing fundamental and the overtone of out-of-plane ring deformation vibration.<sup>30</sup> The relative intensity of two bands sensitively depends on the proximity of the two unperturbed frequencies and thus on the hydrogen bonding conditions of the phenol side-chain. In fact, the tyrosine doublet shows clear spectral changes between 20.0 and 71.0°C as demonstrated in Figure 3-2. For quantitative evaluation of the spectral changes, the spectra in the 780 to 870  $\text{cm}^{-1}$  region in Figure 3-3 were fitted with triple Gaussian functions with inclined straight base line as drawn in the spectra. Two Gaussian functions reflect the tyrosine doublet and the other corresponds to a weak band around 800  $\text{cm}^{-1}$ . The intensity ratios of the low- to high-frequency components are plotted against temperature in Figure 3-9. The intensity ratios of steady state spectra exhibit a large change with a midpoint at 62°C similar to the changes of the  $\nu_{\text{CS}}$  (Figure 3-6(A)) and  $\nu_{\text{SS}}$  Raman bands (Figure 3-8). In the time-resolved spectra, the ratio in the spectrum for  $\Delta t = -100$  ns compared with the probe-only spectrum is different in consequence of the 3°C difference between 59.0 and 62.0°C. However, the intensity ratios little change until 5 ms as illustrated in Figure 3-9, indicating that the conformational changes of the side chain of tyrosine residues do not take place within the initial 5 ms of unfolding. The present results give some information on structural changes which occur in the time region prior to that of the kinetic UV absorption study.<sup>34</sup>

### 3.4.5 SULFATE IONS

RNase A is considered to bind three phosphodiester groups of RNA when it catalyzes the hydrolysis reaction of RNA.<sup>35</sup> In the absence of phosphate ions in this experiment, three sulfate anions are thought to occupy the three phosphate sites. Transient intensity increase around 980  $\text{cm}^{-1}$  demonstrated in Figure 3-6(B) was caused

by the sulfate ions occupying the active site but not by free sulfate ions initially present in the buffer solution. This is evident from the comparison of the spectra shown in panel (B) and (C) in Figure 3-5. One may argue a possibility that it reflects the free sulfate ions which have been released from RNase A due to the base temperature difference (3°C). However, this possibility is unlikely on account of the following reasons; (1) the transient change of the band due to the released sulfate ions, if present, should appear in the spectrum for  $\Delta t = 200$  ns similar to that for the buffer spectrum (b) of Figure 3-5(C), and (2) the transient change of the band around  $980\text{ cm}^{-1}$  in Figure 3-5(B) is not recognized in spectrum (b) for  $\Delta t = 200$  ns but appreciably in spectra (c) for  $\Delta t = 100\text{ }\mu\text{s}$  and (d) for  $\Delta t = 5$  ms. Furthermore, careful examination of the band position in the transient spectra seemed to exhibit a small low-frequency shift ( $\sim 5\text{ cm}^{-1}$ ) with time. Therefore it is concluded that the transient intensity increase around  $980\text{ cm}^{-1}$  originates from the sulfate ions occupying the active site of RNase A and reflects the temporal changes of the structure around the binding site. This may mean that the protein conformation near the active site is more flexible than the other parts and accordingly its structural response to raised temperature is faster.

## REFERENCES

- 1 C. B. Anfinsen, *Science* **181**, 223-230 (1973).
- 2 C. M. Phillips, Y. Mizutani, and R. M. Hochstrasser, *Proc. Natl. Acad. Sci. USA* **92**, 7292-7296 (1995).
- 3 R. M. Ballew, J. Sabelko, and M. Gruebele, *Proc. Natl. Acad. Sci. USA* **93**, 5759-5764 (1996).
- 4 R. M. Ballew, J. Sabelko, and M. Gruebele, *Nature Struct. Biol.* **3**, 923-926 (1996).
- 5 P. A. Thompson, W. A. Eaton, and J. Hofrichter, *Biochemistry* **36**, 9200-9210 (1997).
- 6 V. Munoz, P. A. Thompson, J. Hofrichter, and W. A. Eaton, *Nature* **390**, 196-199 (1997).
- 7 S. Williams, T. P. Causgrove, R. Gilmanshin, K. S. Fang, R. H. Callender, W. H. Woodruff, and R. B. Dyer, *Biochemistry* **35**, 691-697 (1996).
- 8 R. Gilmanshin, S. Williams, R. H. Callender, W. H. Woodruff, and R. B. Dyer, *Proc. Natl. Acad. Sci. USA* **94**, 3709-3713 (1997).
- 9 R. Gilmanshin, S. Williams, R. H. Callender, W. H. Woodruff, and R. B. Dyer, *Biochemistry* **36**, 15006-15012 (1997).
- 10 I. K. Lednev, A. S. Karnoup, M. C. Sparrow, and S. A. Asher, *J. Am. Chem. Soc.* **121**, 4076-4077 (1999).
- 11 I. Harada and H. Takeuchi, in *Advances in Spectroscopy*, Vol. 13, edited by R. J. H. Clark and R. E. Hester (John Wiley & Sons, New York, 1986), pp. 113-175.
- 12 K. Yamamoto, Y. Mizutani, and T. Kitagawa, in *9th Intl. Conf. Time-Resolved Vibrational Spectroscopy* (Tucson, 1999), P12-A.
- 13 C. B. Anfinsen and H. A. Scheraga, *Adv. Protein Chem.* **29**, 205-300 (1975).
- 14 Y. Konishi, T. Ooi, and H. A. Scheraga, *Proc. Natl. Acad. Sci. USA* **79**, 5734-5738 (1982).
- 15 S. J. Wearne and T. E. Creighton, *Proteins* **4**, 251-261 (1988).
- 16 D. M. Rothwarf and H. A. Scheraga, *Biochemistry* **32**, 2698-2703 (1993).
- 17 Y. J. Li, D. M. Rothwarf, and H. A. Scheraga, *Nature Struct. Biol.* **2**, 489-494 (1995).
- 18 B. Howlin, D. S. Moss, and G. W. Harris, *Acta Crystallogra., Sect. A* **45**, 851-861 (1989).
- 19 D. M. Rothwarf and H. A. Scheraga, *J. Am. Chem. Soc.* **113**, 6293-6294 (1991).
- 20 S. Talluri, D. M. Rothwarf, and H. A. Scheraga, *Biochemistry* **33**, 10437-10449 (1994).

- 21 J. H. Laity, C. C. Lester, S. Shimotakahara, D. E. Zimmerman, G. T. Montelione, and H. A. Scheraga, *Biochemistry* **36**, 12683-12699 (1997).
- 22 H. Sugeta, A. Go, and T. Miyazaya, *Chem. Lett.*, 83-86 (1972).
- 23 H. Sugeta, A. Go, and T. Miyazaya, *Bull. Chem. Soc. JPN.* **46**, 3407-3411 (1973).
- 24 H. Sugeta, *Spectrochim. Acta* **31A**, 1729-1737 (1975).
- 25 N. Nogami, H. Sugeta, and T. Miyazawa, *Chem. Lett.*, 147-150 (1975).
- 26 N. Nogami, H. Sugeta, and T. Miyazawa, *Bull. Chem. Soc. JPN.* **48**, 2417-2420 (1975).
- 27 N. Nogami, H. Sugeta, and T. Miyazawa, *Bull. Chem. Soc. JPN.* **48**, 3573-3575 (1975).
- 28 D. M. Rothwarf and H. A. Scheraga, *Biochemistry* **32**, 2671-2679 (1993).
- 29 M. Sela and C. B. Anfinsen, *Biochim. Biophys. Acta* **24**, 229-235 (1957).
- 30 M. N. Siamwiza, R. C. Lord, M. C. Chen, T. Takamatsu, I. Harada, H. Matsuura, and T. Shimanouchi, *Biochemistry* **14**, 4870-4876 (1975).
- 31 M. C. Chen and R. C. Lord, *Biochemistry* **15**, 1889-1897 (1976).
- 32 T. Y. Tsong, R. P. Hearn, D. P. Wrathall, and J. M. Sturtevant, *Biochemistry* **9**, 2666-2677 (1970).
- 33 P. L. Privalov, *Crit. Rev. Biochem. Mol. Biol.* **25**, 281-305 (1990).
- 34 P. J. Hagerman and R. L. Baldwin, *Biochemistry* **15**, 1462-1473 (1976).
- 35 C. Arus, L. Paolillo, R. Llorens, R. Napolitano, and C. M. Cuchillo, *Biochemistry* **21**, 4290-4297 (1982).

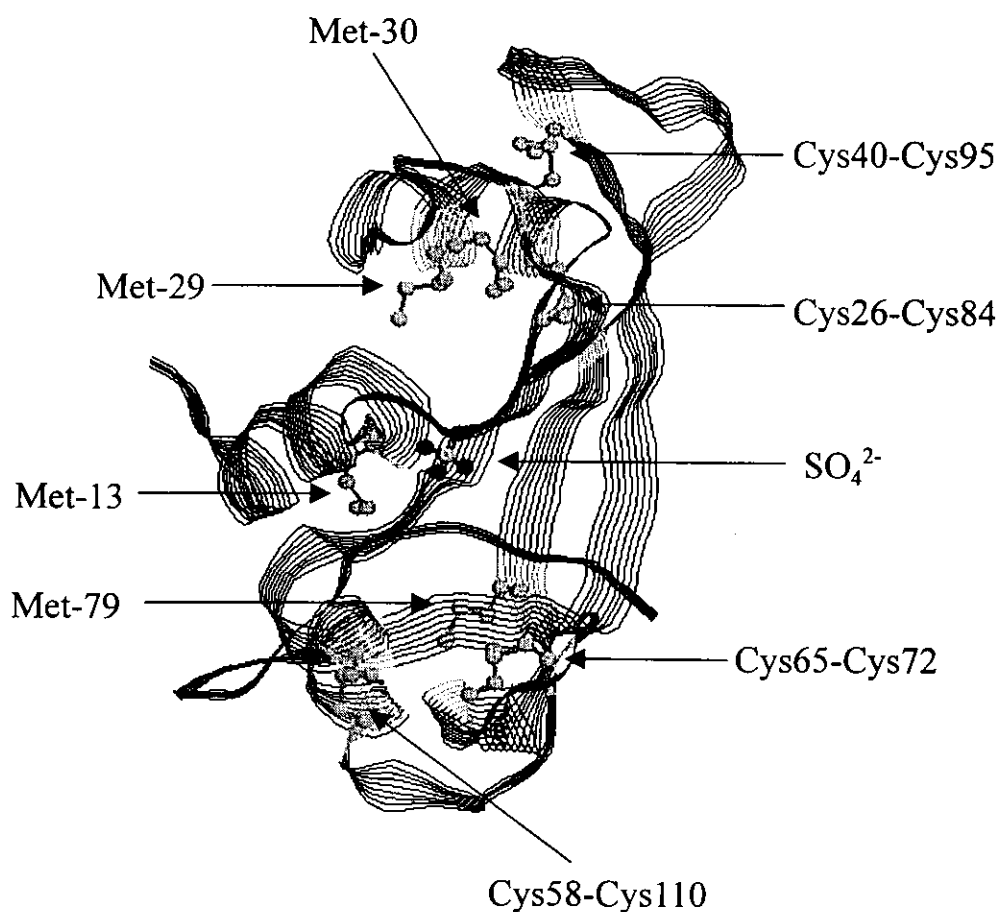


**Figure 3-1.** Structure of RNase A obtained by X-ray crystallography<sup>18</sup>. All the eight cysteine residues form four disulfide bridges; Cys-26–Cys-84, Cys-40–Cys-95, Cys-58–Cys-110, and Cys-65–Cys-72. All the disulfide bridges ( $C_\alpha-C_\beta H_2-S_\gamma-S'_\gamma-C'_\beta H_2-C'_\alpha$ ) adopt the GGG conformation. The *trans* position of the sulfur atom in  $X-C_\alpha-C_\beta H_2-S_\gamma$  group is occupied by a carbon atom of an amide group in all the cysteine residues ( $P_C$ -form). Four methionine residues (Met-13, -29, -30 and -79) have two conformations regarding the  $X-C_\beta-C_\gamma H_2-S_\delta-C_\epsilon H_3$  group; one is the  $P_H$ -G form as seen for Met-13, -29, and -30 where hydrogen atom occupies the *trans* position of the sulfur atom with *gauche* form of  $C_\beta-C_\gamma H_2-S_\delta-C_\epsilon H_3$  and the other is the  $P_C$ -T form as seen for Met-79 where  $\alpha$ -carbon occupies the *trans* position of the sulfur atom. A sulfate ion observed by X-ray crystallography is bound at the active site of RNase A.

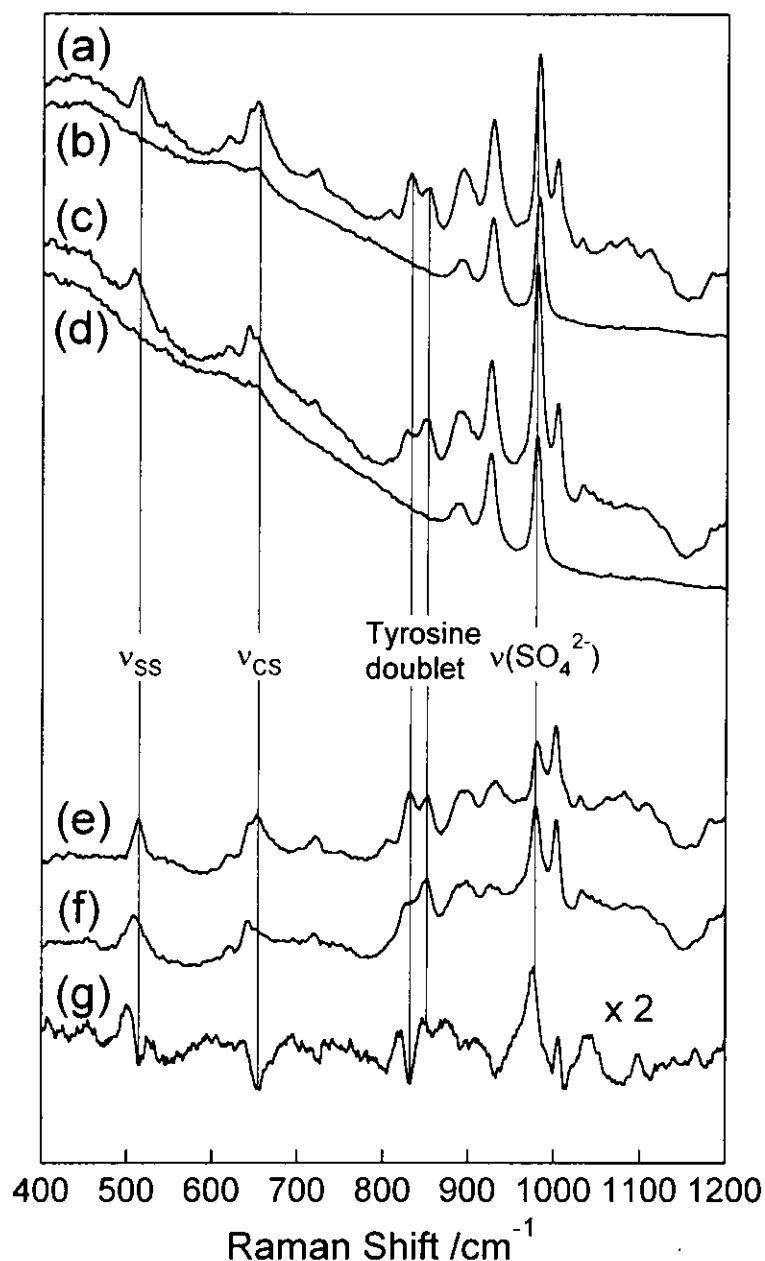


**Figure 3-2.** Steady Raman spectra of RNase A and buffer solution (200 mM acetate buffer, pH 5.0 containing 40 mM  $\text{Na}_2\text{SO}_4$ ); Spectra (a, b, and e) were obtained at 20.0°C and spectra (c, d, and f) at 71.0°C. Trace (g) shows the temperature-difference spectrum of RNase A,  $(g) = 2 \times [(f) - (e)]$ . Spectra (a) and (c) are the raw Raman spectra of RNase A containing the buffer solution and spectra (b) and (d) are those of the buffer solution only. Spectra (e) and (f) were obtained by subtraction of buffer-solution spectra [(b) and (d)] from the raw RNase A spectra [(a) and (c)] at each temperature;  $(e) = (a) - (b)$  and  $(f) = (c) - (d)$ . Hence the difference spectrum (g) of RNase A does not include the spectral changes of buffer solution. Experimental conditions: exposure time, 30 s; repetition, 60; laser, 532 nm, 5 mJ/pulse.



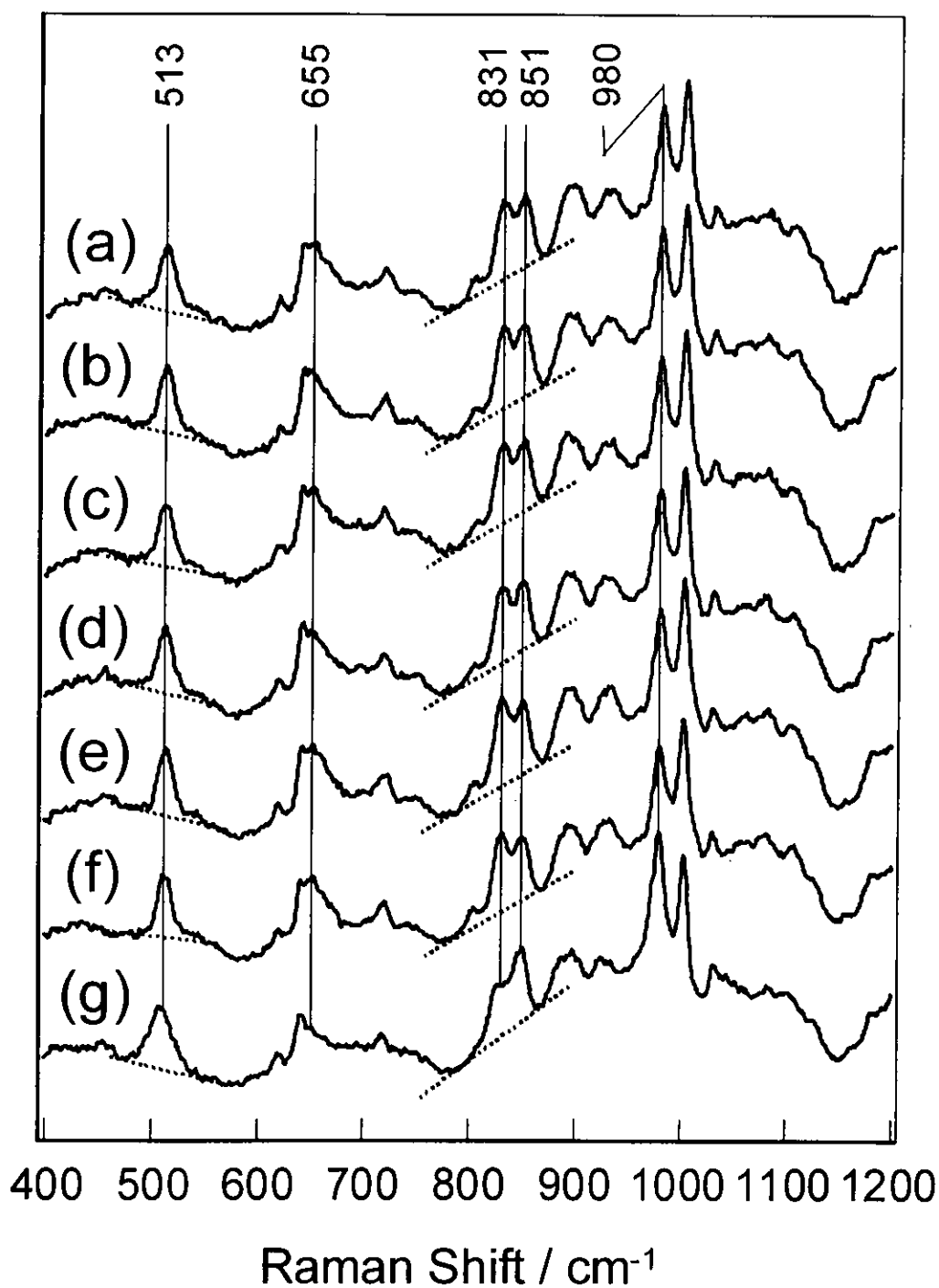


**Figure 3-3.** Time-resolved Raman spectra of RNase A upon T-jump. (a)  $\Delta t = -100$  ns, (b)  $\Delta t = 200$  ns, (c)  $\Delta t = 100$   $\mu$ s, (d)  $\Delta t = 5$  ms, (e) probe only at  $T_0$  (59.0°C), (f) stationary state spectrum at 59.0°C, (g) stationary state spectrum at 71.0°C. Buffer spectra, which were obtained under the same experimental conditions as respective raw spectra of RNase A solution, had been subtracted in all the spectra (a)-(g). Broken lines designate the base lines assumed for the calculations of intensity and bandwidth.

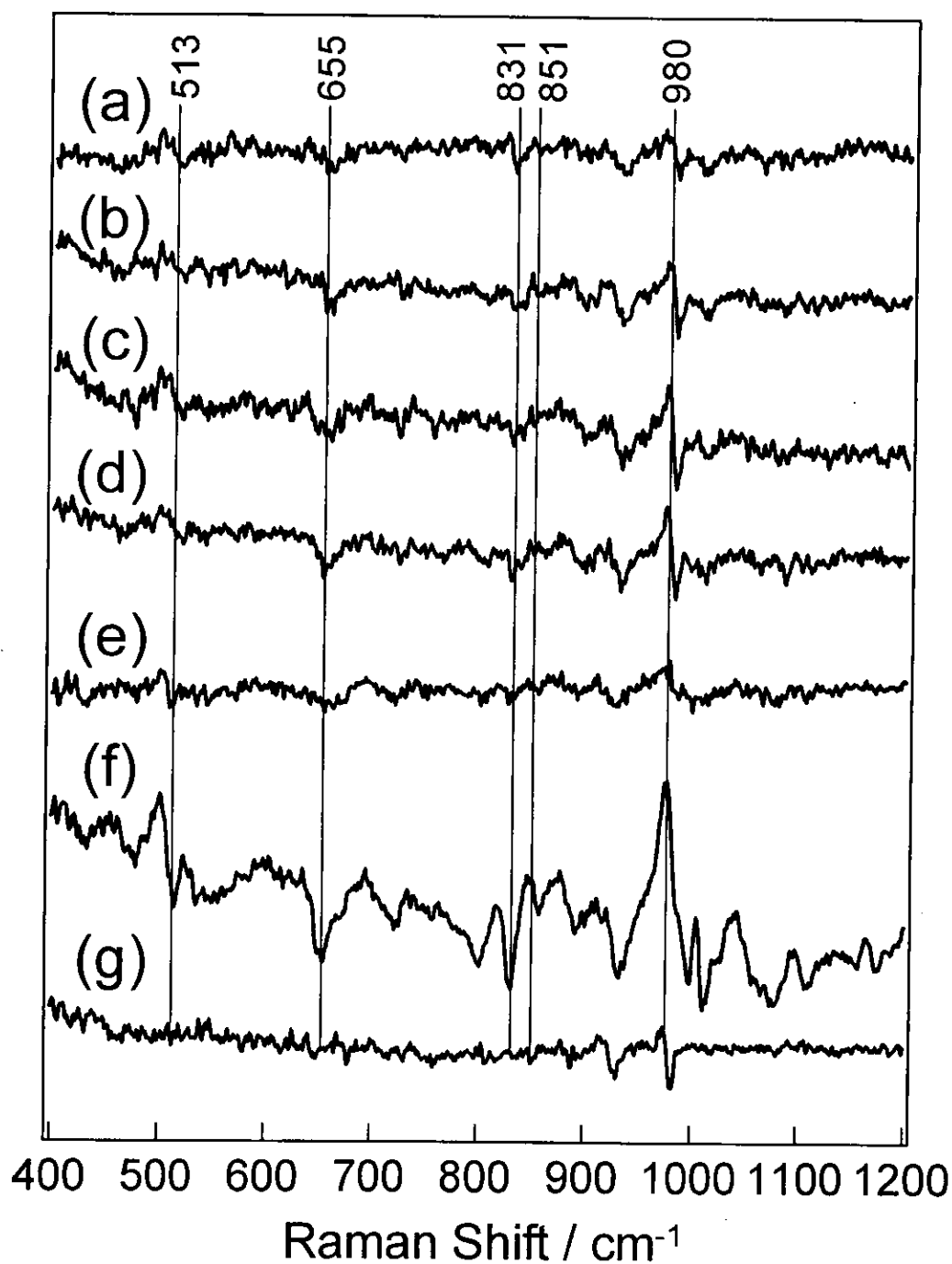


**Figure 3-4.** Difference spectra of RNase A upon T-jump; (a)-(d) pump/probe – probe-only; (e)-(g) steady state temperature-difference spectra. (a)  $\Delta t = -100$  ns, (b)  $\Delta t = 200$  ns, (c)  $\Delta t = 100$   $\mu$ s, (d)  $\Delta t = 5$  ms, (e)  $62.0^{\circ}\text{C} - 59.0^{\circ}\text{C}$ , (f)  $71.0^{\circ}\text{C} - 59.0^{\circ}\text{C}$ , (g) buffer-only  $71.0^{\circ}\text{C} - 59.0^{\circ}\text{C}$ . Since raw spectra were used for this calculations, spectra (a)-(f) contain spectral changes of buffer solution.

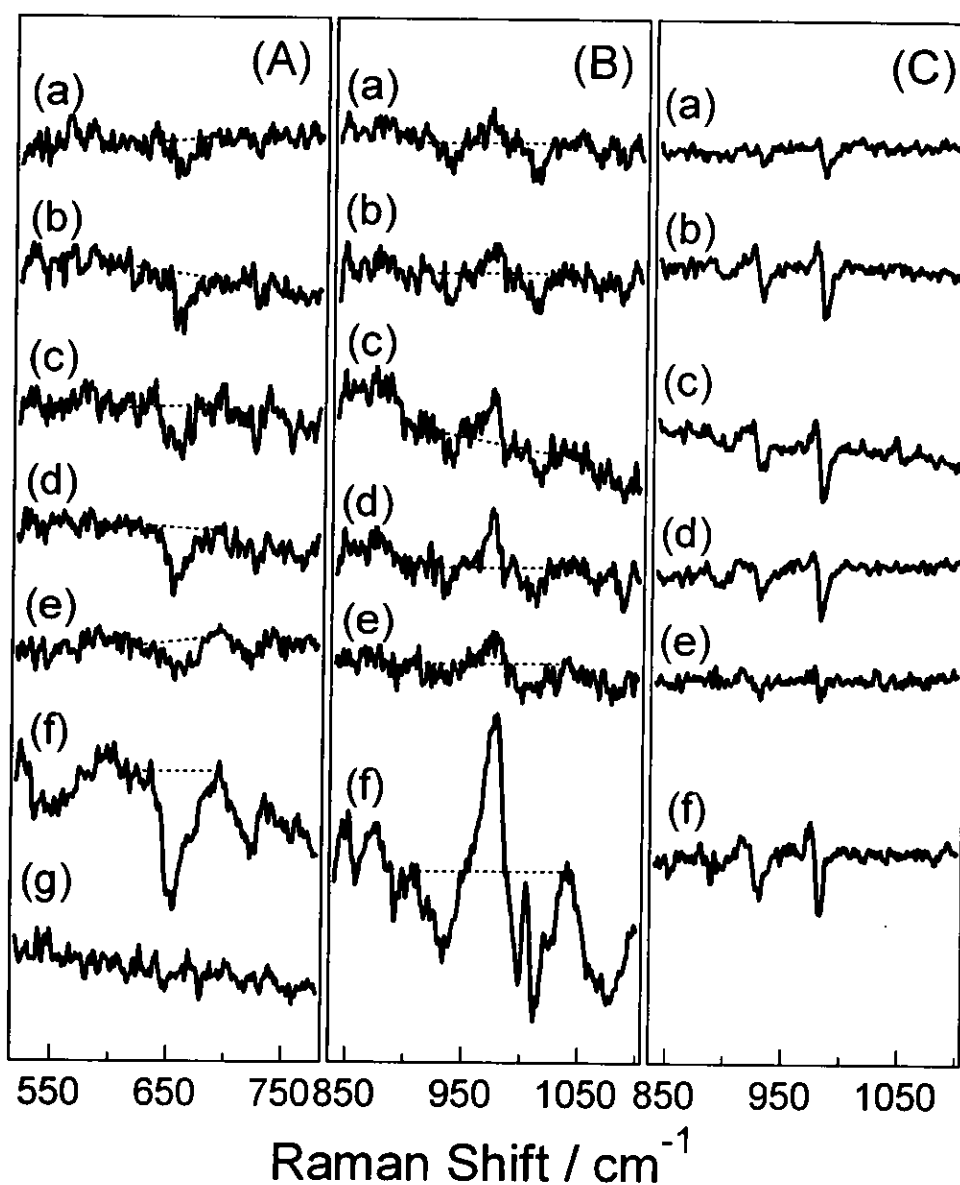


**Figure 3-5.** The expanded difference Raman spectra of RNase A upon T-jump for the C-S stretching (A) and  $\text{SO}_4^{2-}$  stretching regions (B) and those of buffer solution only (C) upon T-jump; Spectra (a)-(d) show the differences, pump/probe - probe-only, and spectra (e)-(g) show the stationary-state temperature-difference spectra; (a)  $\Delta t = -100$  ns, (b)  $\Delta t = 200$  ns, (c)  $\Delta t = 100$   $\mu\text{s}$ , (d)  $\Delta t = 5$  ms, (e)  $62.0^\circ\text{C} - 59.0^\circ\text{C}$ , (f)  $71.0^\circ\text{C} - 59.0^\circ\text{C}$ , and (g) buffer-only  $71.0^\circ\text{C} - 59.0^\circ\text{C}$ . Buffer difference spectra (a)-(f) in panel (C), were observed under the same conditions as those for (B). In practice, spectra in panel (B) were obtained by subtracting spectra (a)-(f) in panel (C) from spectra (a)-(f) in Figure 3-7, respectively, although such subtraction had not been done for spectra in panel (A). The ordinate and abscissa scales in panel (B) and (C) are the same. The broken lines denote the base lines used for the difference intensity calculations.

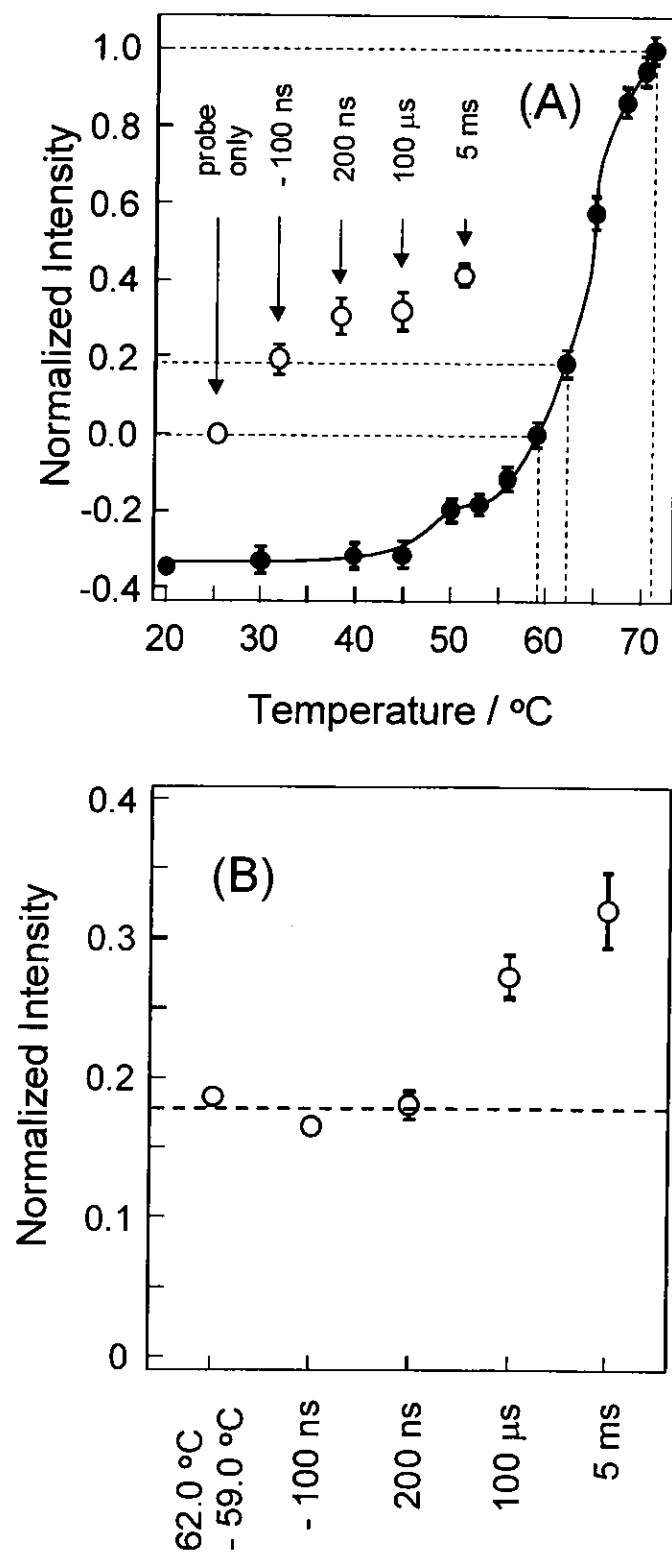


**Figure 3-6.** Intensity decrease of the  $\nu_{CS}$  bands (A) and intensity increase of  $SO_4^{2-}$  bands (B) of RNase A upon T-jump (open circles) and upon steady state temperature change (closed circles).

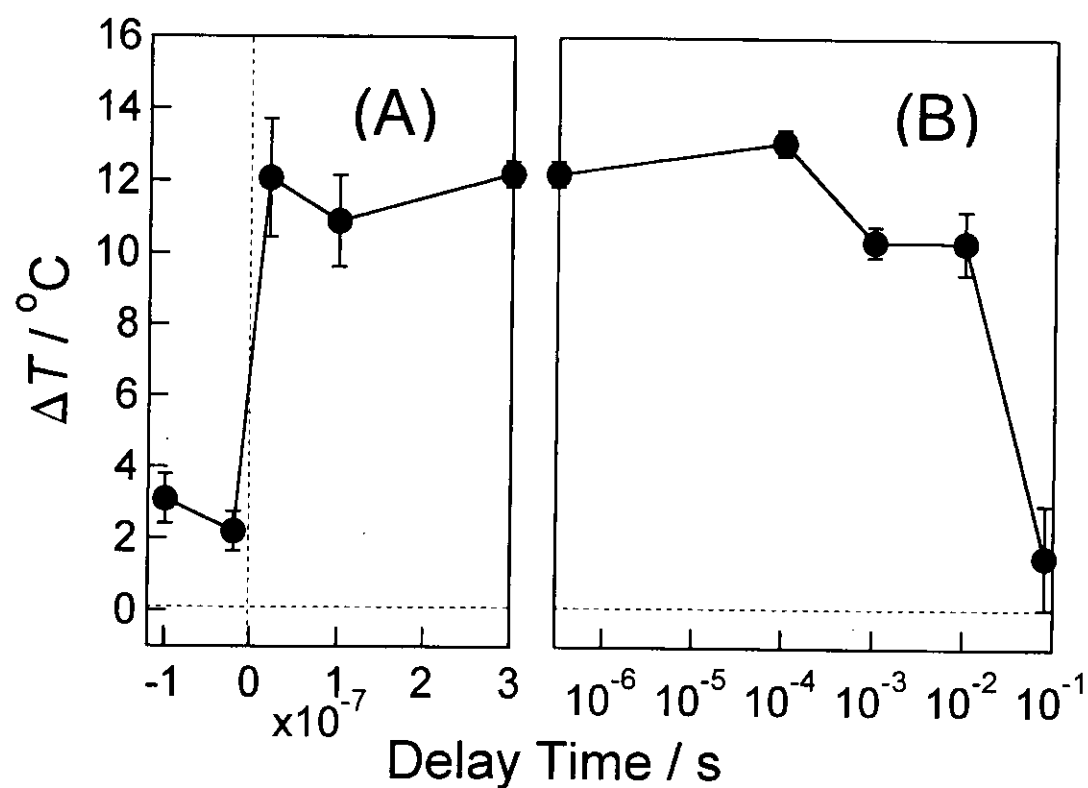


**Figure 3-7.** Temperature rise observed for the mixture solution of  $\text{MoO}_4^{2-}$  ions (0.42 M) with RNase (7 mM) under the same experimental conditions as those for Figure 2-8(A) and 2-9(A). The scale of abscissas is linear in a shorter time region (A) but logarithmic in a longer time region (B).

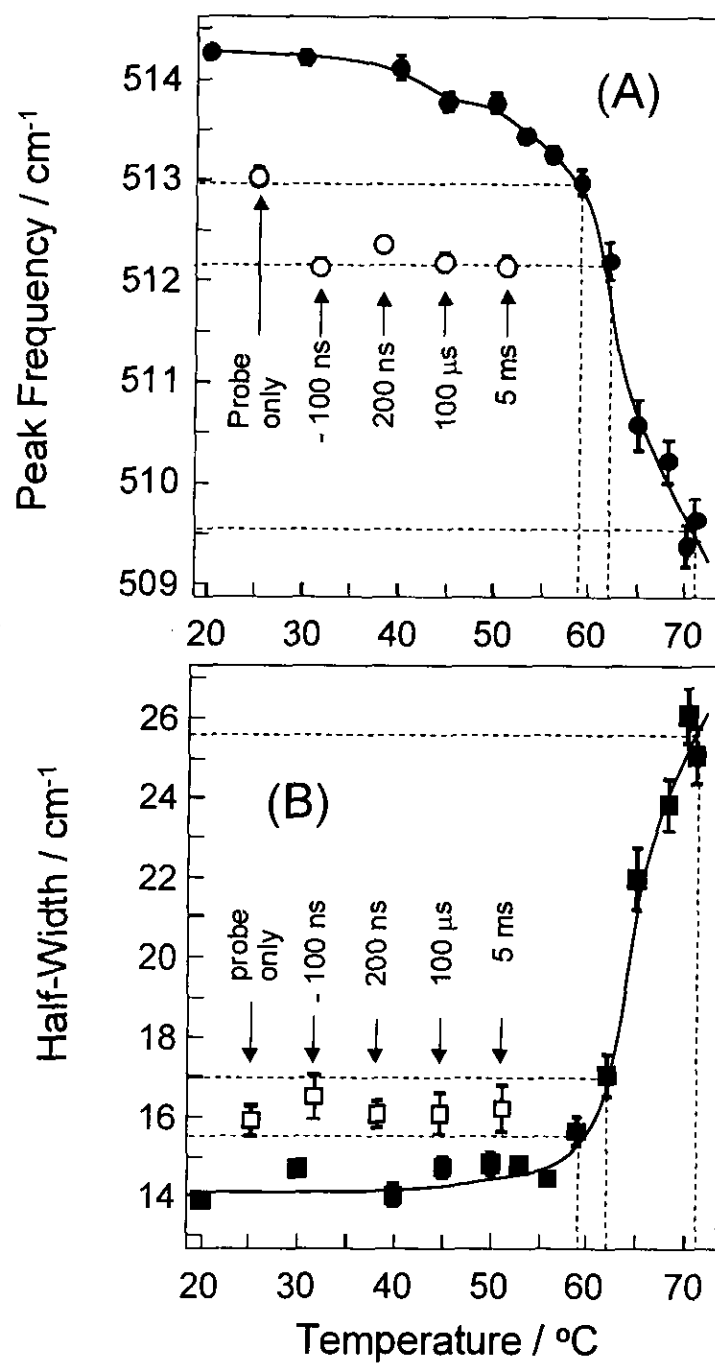


**Figure 3-8.** Peak-shift and band-broadening of the  $\nu_{ss}$  bands of RNase A upon T-jump (open markers) and upon steady state temperature change (closed markers). (A) peak frequency and (B) half-width.

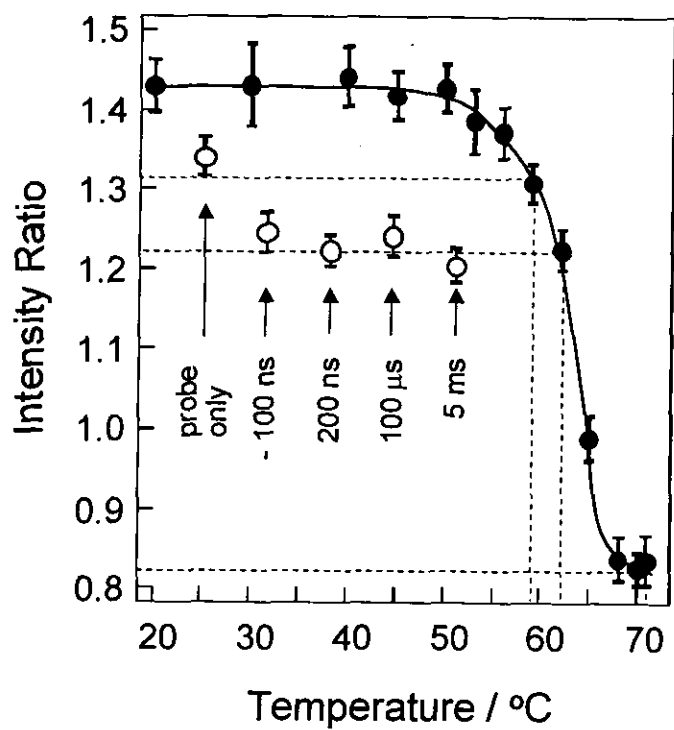


**Figure 3-9.** Intensity ratio of tyrosine doublet ( $I_{831}/I_{851}$ ) of RNase A upon T-jump (open circle) and upon steady state temperature change (closed circle).







## List of Publications

### 1. Fast Protein Dynamics Probed by Vibrational Spectroscopy

Y. Mizutani, K. Yamamoto and T. Kitagawa

*Old and New Views of Protein Folding* ; K. Kuwajima and M. Arai, Eds.; Elsevier Science; The Netherlands; 1999; p85-94

### 2. Nanosecond Temperature Jump and Time-Resolved Raman Study of Thermal Unfolding of Ribonuclease A

K. Yamamoto, Y. Mizutani and T. Kitagawa

*Biophysical Journal* (in press)

### 3. Construction of Novel Nanosecond Temperature Jump Apparatuses Applicable to Raman Measurements and Direct Observation of Transient Temperature

K. Yamamoto, Y. Mizutani and T. Kitagawa

*Applied Spectroscopy* (in submission)

## Acknowledgement

The present thesis is a summary of the author's studies from 1996 to 2000 at Department of Functional Molecular Science, the Graduate University for Advanced Studies. This work is generously supported by Institute for Molecular Science and carried out under the supervision of Professor Teizo Kitagawa. The author wishes to express his cordial gratitude to Professor Teizo Kitagawa for his continual direction, stimulating discussion, and hearty encouragement. The author also wishes to acknowledge profound indebtedness to Dr. Yasuhisa Mizutani for his guidance and fruitful discussions throughout the course of this study.

The author is indebted to Professor Shingo Tsuyama of Osaka Prefecture University for his help in the purification of RNase A and to Associate Professor Atsuo Tamura of Kobe University for his advice on the treatments of RNase A.

This work would not have been possible without help of the members and coworkers in the Professor Kitagawa's laboratory, to whom the author is deeply indebted.

Finally, the author expresses his sincere gratitude to his family for their supports, generous understanding, and affectionate encouragement.

January, 2000

Okazaki

Kohji Yamamoto